ABSTRACT

Title of dissertation: NONLINEAR OPTICS AND CARRIER DYNAMICS IN NANOSTRUCTURED AND TWO-DIMENSIONAL MATERIALS

Ryan J. Suess, Doctor of Philosophy, 2016

Dissertation directed by: Professor Thomas E. Murphy
Institute for Research in Electronics & Applied Physics
Department of Electrical & Computer Engineering

Understanding and measuring the interaction of light with sub-wavelength structures and atomically thin materials is of critical importance for the development of next generation photonic devices. One approach to achieve the desired optical properties in a material is to manipulate its mesoscopic structure or its composition in order to affect the properties of the light-matter interaction. There has been tremendous recent interest in so called two-dimensional materials, consisting of only a single to a few layers of atoms arranged in a planar sheet. These materials have demonstrated great promise as a platform for studying unique phenomena arising from the low-dimensionality of the material and for developing new types of devices based on these effects. A thorough investigation of the optical and electronic properties of these new materials is essential to realizing their potential. In this work we present studies that explore the nonlinear optical properties and carrier dynamics in nanoporous silicon waveguides, two-dimensional graphite (graphene), and atomically thin black phosphorus.

We first present an investigation of the nonlinear response of nanoporous silicon optical waveguides using a novel pump-probe method. A two-frequency heterodyne technique is developed in order to measure the pump-induced transient change in phase and intensity in a single measurement. The experimental data reveal a characteristic material response time and temporally resolved intensity and phase behavior matching a physical model dominated by free-carrier effects that are significantly stronger and faster than those observed in traditional silicon-based waveguides. These results shed light on the large optical nonlinearity observed in nanoporous silicon and demonstrate a new measurement technique for heterodyne pump-probe spectroscopy.

Next we explore the optical properties of low-doped graphene in the terahertz spectral regime, where both intraband and interband effects play a significant role. Probing the graphene at intermediate photon energies enables the investigation of the nonlinear optical properties in the graphene as its electron system is heated by the intense pump pulse. By simultaneously measuring the reflected and transmitted terahertz light, a precise determination of the pump-induced change in absorption can be made. We observe that as the intensity of the terahertz radiation is increased, the optical properties of the graphene change from interband, semiconductor-like absorption, to a more metallic behavior with increased intraband processes. This transition reveals itself in our measurements as an increase in the terahertz transmission through the graphene at low fluence, followed by a decrease in transmission and the onset of a large, photo-induced reflection as fluence is increased. A hybrid optical-thermodynamic model successfully describes our observations and predicts

this transition will persist across mid- and far-infrared frequencies. This study further demonstrates the important role that reflection plays since the absorption saturation intensity (an important figure of merit for graphene-based saturable absorbers) can be underestimated if only the transmitted light is considered. These findings are expected to contribute to the development of new optoelectronic devices designed to operate in the mid- and far-infrared frequency range.

Lastly we discuss recent work with black phosphorus, a two-dimensional material that has recently attracted interest due to its high mobility and direct, configurable band gap (300 meV to 2 eV) depending on the number of atomic layers comprising the sample. In this work we examine the pump-induced change in optical transmission of mechanically exfoliated black phosphorus flakes using a two-color optical pump-probe measurement. The time-resolved data reveal a fast pump-induced transparency accompanied by a slower absorption that we attribute to Pauli blocking and free-carrier absorption, respectively. Polarization studies show that these effects are also highly anisotropic - underscoring the importance of crystal orientation in the design of optical devices based on this material. We conclude our discussion of black phosphorus with a study that employs this material as the active element in a photoconductive detector capable of gigahertz class detection at room temperature for mid-infrared frequencies.

NONLINEAR OPTICS AND CARRIER DYNAMICS IN NANOSTRUCTURED AND TWO-DIMENSIONAL MATERIALS

by

Ryan J. Suess

Dissertation submitted to the Faculty of the Graduate School of the
University of Maryland, College Park in partial fulfillment
of the requirements for the degree of
Doctor of Philosophy
2016

Advisory Committee:
Professor Thomas E. Murphy, Chair/Advisor
Professor H. Dennis Drew
Professor Julius Goldhar
Professor Romel Gomez
Professor Jeremy Munday

For my family

Acknowledgments

I would like to acknowledge and thank those who have helped me with the work presented in this thesis as well as those who have supported me throughout the years while I pursued my education.

There are a number of mentors who have helped me throughout my career and it is their guidance and direction that has helped me grow intellectually and achieve my professional and educational goals. First I would like to acknowledge Professor Leon McCaughan of the University of Wisconsin. Without your guidance early on in my career I would not have pursued the type work that I have; thank you for helping me get my start in optics and photonics research. I would also like to recognize Dr. Eric Hines and Dr. Lyle Shirley at the Massachusetts Institute of Technology-Lincoln Laboratory. Thank you for sharing your considerable technical expertise with me and making my time at the Laboratory both interesting and fulfilling. I would like to thank Professor Dennis Drew at the University of Maryland for the many thought provoking conversations from which I learned a lot about physics. Finally I would like to thank my thesis advisor Professor Thomas Murphy. Thank you for giving me the opportunity to work within your group and for demonstrating excellence and thoughtfulness in your approach to research. Your example has made me a better scientist and I am grateful for the direction that you've offered me during my doctoral studies.

With respect to the work presented in this thesis, I would like to acknowledge the following individuals for their assistance and contributions to this work: I thank

Dr. Kyowon Kim and Dr. Ke-Yao Wang for providing the waveguides that were characterized in section 2.2.2 and in section 2.3.1, respectively. I am further grateful to Dr. Martin Mittendorff for collecting the experimental data presented in Chapter 3 that enabled the analysis and modeling efforts that are developed in the same chapter. Finally I would like to credit Dr. Xinghan Cai for providing the graphene devices that were characterized in section 3.1.3. To the other numerous co-authors that I've worked with: thank you for the discussions and the occasional extra hand you've pitched in to help me carry out this work. Specifically I would like to thank the many exceptional post-docs, scientists, and fellow graduate students who I've met while at Maryland: Xinghan Cai, Aaron Haagerstrom, Mehdi Jadidi, Kyowon Kim, Myoung-Hwan Kim, Gagan Kumar, Edward Leong, Shanshan Li, Vincent Págan, Andrei Sushkov, J.J. Wathen, and Jun Yan. Dr. Martin Mittendorff deserves special acknowledgment for the many enjoyable and productive conversations we've had during our time as colleagues and also for teaching me the German term for "shrink-wrap tubing". I would also like to thank Dr. Andrew Lee for the many lively conversations regarding research, science, and philosophy and for occasionally letting me win at squash. Several friends and former colleagues who've provided me with perspective and advice throughout my studies also deserve mention: Andrew Berkovich, Manish Bhardwaj, Daniel Burke, Alexander Hayes, Matthew Grein, Ronny Huang, Micah Kalscheur, Chad Staus, and Jon Watson. Thanks again to everyone here for helping me along the way.

Most of all I would like to thank my family. Without the support and encouragement of my mother and father none of this would be possible. Thank you for inspiring me and making it possible for me to fully pursue my education. To my brother and sister in-law, thank you for the good humor and laughs. To my extended family, thank you for the encouragement and for always expressing interest in my studies. I would also like acknowledge Maxwell for his friendship and company during the long, late hours required to carry out much of this work. Lastly, I thank my wife Kerri for her love and support during my doctoral studies.

Table of Contents

Contributed Work

Journal Publications

R.J. Suess, E. Leong, T. Zhou, R. Salem, T.E. Murphy, M. Mittendorff, "Gigahertz Room Temperature Mid-Infrared Detection with Black Phosphorus", *manuscript in preparation*

M.M. Jadidi, R.J. Suess, X. Cai, A.B. Sushkov, M. Mittendorff, H.D. Drew, M.S. Fuhrer, T.E. Murphy, "Infrared Two-wave Mixing in Graphene Photodetectors", *manuscript in preparation*

R.J. Suess, S. Winnerl, T.E. Murphy, M. Mittendorff, "Role of Photoinduced Reflection in Graphene Nonlinear Infrared Optics", *manuscript under review, ACS Photonics*

M. Mittendorff, J. Kamann, J. Eroms, D. Weiss, C. Drexler, S.D. Ganichev, J. Kerbusch, A. Erbe, R.J. Suess, T.E. Murphy, S. Chatterjee, K. Kolata, J. Ohser, J.C. Knig-Otto, H. Schneider, M. Helm and S. Winnerl, "Universal ultrafast detector for short optical pulses based on graphene", Opt. Express 23(22) 28728-28735 (2015).

X. Cai, R.J. Suess, H. D. Drew, T. E. Murphy, J. Yan and M.S. Fuhrer, "Pulsed Near-IR Photoresponse in a Bi-metal Contacted Graphene Photodetector", Sci. Rep. 514803 (2015).

R.J. Suess, M. M. Jadidi, T. E. Murphy and M. Mittendorff, "Carrier dynamics and transient photobleaching in thin layers of black phosphorus", Appl. Phys. Lett. 107(8) 081103 (2015).

J.J. Wathen, V.R. Pagán, R.J. Suess, K-Y. Wang, A.C. Foster, T.E. Murphy, "Non-instantaneous optical nonlinearity of an a-Si:H nanowire waveguide", Optics Express (2014).

X. Cai, A.B. Sushkov, R.J. Suess, M.M. Jadidi, G.S. Jenkins, J. Yan, L.O. Nyakiti, R.L. Myers-Ward, D. Kurt Gaskill, Thomas E. Murphy, H. Dennis Drew, Michael S. Fuhrer, "Sensitive Room Temperature Terahertz Detection via Photothermoelectric Effect in Graphene", Nature Nanotechnology (2014).

R.J. Suess, M.M. Jadidi, K. Kim and T.E. Murphy,"Characterization of optical nonlinearities in nanoporous silicon waveguides via pump-probe heterodyning technique", Opt. Express 22(14) 17466-17477 (2014)

M.-H. Kim, J. Yan, R.J. Suess, T.E. Murphy, H.D. Drew, M.S. Fuhrer, "Photo-thermal response in dual-gated bilayer graphene", Physical Review Letters (2013).

Conference Publications

R.J. Suess, E. Leong, T. E. Murphy and M. Mittendorff, "Intrinsic Speed of a Black Phosphorus Photoconductive Detector", *Conference on Lasers and Electrooptics (CLEO), San Jose, CA (USA)* (2016).

R.J. Suess, S. Winnerl, H. Schneider, M. Helm, C. Berger, W.A. de Heer, T.E. Murphy and M. Mittendorff, "Far-Infrared Nonlinear Optics in Multilayer Epitaxial Graphene", *Conference on Lasers and Electrooptics (CLEO), San Jose, CA (USA)* (2016).

E. Leong, R.J. Suess, A. Sushkov, H.D. Drew, T. E. Murphy and M. Mittendorff, "THz Photoresponse of Thin Layers of Black Phosphorus", *Conference on Lasers and Electrooptics (CLEO), San Jose, CA (USA)* (2016).

M. Mittendorff, E. Leong, R.J. Suess, A. Sushkov, H.D. Drew and T. E. Murphy, "Room Temperature THz Detection with Thin Layers of Black Phosphorus", *Graphene, Genoa (Italy)* (2016).

R.J. Suess, M. M. Jadidi, T. E. Murphy and M. Mittendorff, "Time Resolved Spectroscopy on Thin Layers of Black Phosphorus", *Frontiers in Optics - Laser Science (FiO-LS), San Jose, CA (USA)* (2015).

Mohammad M. Jadidi, Ryan J. Suess, Xinghan Cai, Andrei B. Sushkov, Martin Mittendorff, Michael S. Fuhrer, H. Dennis Drew, and Thomas E. Murphy, "Characterization of Graphene Photothermoelectric Detector via Two-wave Mixing Technique", *Conference on Lasers and Electrooptics (CLEO), San Jose, CA (USA)* (2015).

R.J. Suess, X.Cai, M.M. Jadidi, A.B. Sushkov, G.S. Jenkins, J. Yan, L.O. Nyakiti, R.L. Myers-Ward, D.K. Gaskill, T.E. Murphy, H.D. Drew, M.S. Fuhrer, "Characterization of Fast Temporal Photoreponse in a Broadband Graphene Photodetector", *Conference on Lasers and Electrooptics (CLEO), San Jose, CA (USA)* (2014).

X.Cai, R.J. Suess, A. Sushkov, T.E. Murphy, H.D. Drew, M.S. Fuhrer "Broadband Response of a Graphene Photodetector", *Conference on Lasers and Electrooptics (CLEO), San Jose, CA (USA)* 2013.

R.J. Suess and T.E. Murphy, "Third-Order Optical Nonlinearity in Bulk Nanoporous Silicon at Telecom Wavelengths", *Conference on Lasers and Electrooptics (CLEO), San Jose, CA (USA)* (2012).

Conference Procedings

R.J. Suess, M.M. Jadidi, T.E. Murphy and M. Mittendorff, "Transmission pump-probe spectroscopy on multilayer black phosphorus", APS March Meeting, Baltimore, MD (USA) BAPS.2016.MAR.L16.8 (2016)

M. Mittendorff , R.J. Suess, T.E. Murphy , H. Schneider, M. Helm and S. Winnerl, "Pump-induced far-infrared reflection in quasi-intrinsic graphene ", APS March Meeting, Baltimore, MD (USA) BAPS.2016.MAR.A17.11 (2016)

H.D. Drew , M.M. Jadidi , A. Sushkov , X. Cai , R. Suess , M. Mittendorff , T. Murphy , M. Fuhrer , K. Daniels , K. Gaskill, "Infrared two-wave mixing technique for characterization of graphene THz plasmonic devices", APS March Meeting, Baltimore, MD (USA) BAPS.2016.MAR.B16.3

A. Boyd, A. Nath, M. Jadidi, R. Suess, A. Sushkov, G. Jenkins, H. D. Drew, T. E. Murphy, R. Myers-Ward, K. Daniels and D. K. Gaskill, "Top Gated Graphene PN junctions for THz detection", APS March Meeting, San Antonio, TX (USA) BAPS.2015.MAR.M17.9 (2015)

R. J. Suess, X. Cai, A. Sushkov, G. Jenkins, M.-H. Kim, J. Yan, H. D. Drew, T. E. Murphy and M. S. Fuhrer, "Temporal characterization of hot-electron thermoelectric effect in monolayer graphene devices", APS March Meeting, Baltimore, MD (USA) BAPS.2013.MAR.J7.7 (2013)

M.-H. Kim, J. Yan, R. J. Suess, T. E. Murphy, M. S. Fuhrer and H. D. Drew, "Photovoltaic response time in dual-gated bilayer graphene", APS March Meeting, Baltimore, MD (USA) BAPS.2013.MAR.J7.5 (2013)

X. Cai, R. J. Suess, A. Sushkov, G. Jenkins, M.-H. Kim, J. Yan, H. D. Drew, T. E. Murphy and M. S. Fuhrer, "Sensitive bolometry using hot-electron thermoelectric effect in graphene devices", APS March Meeting, Baltimore, MD (USA) BAPS.2013.MAR.J7.8 (2013)

Chapter 1: Introduction

1.1 Overview

The work presented in this this thesis covers nonlinear optical properties in bulk nanostructured materials patterned into confining waveguide structures and atomically thin, "two-dimensional" materials consisting of sheets of atoms. In each of these systems unusual phenomena and sometimes surprisingly regular behavior appears. For many of the cases considered here, the time scales of this behavior are exceedingly short - typically being in the range of 10^{-9} to 10^{-15} seconds. This is both interesting and challenging for an experimentalist who has to come up with a way to observe the anticipated (or unknown) behavior. The overarching theme of the work presented herein is that of exploring scientifically and technologically interesting material systems using time-domain experimental methods enabled by pulsed laser systems. Investigations pursuing an understanding of fast time-domain phenomenology often requires some experimental ingenuity, and thus a minor theme in this work also addresses methods for capturing the physics of interest in measurement.

Ultrafast laser spectroscopy or ultrafast time domain spectroscopy make use of short pulses (of order 10^1 to 10^2 fs) and high pulse energies to observe the tem-

poral dynamics of materials while providing insight into the physical mechanisms governing a substance's behavior [1, 2]. Time-domain spectroscopic techniques have been employed in a wide range of fields including physical chemistry, biology, and physics [3–6]. The high intensity possible with pulsed laser systems is another critical aspect for the studies carried out in this work. In confining structures or nanostructured materials of the type considered in this work, fields can reach exceptionally high values and produce highly nonlinear behavior. In combination with the time-resolution provided by the short laser pulse, the high pulse energy allows the probing of the nonlinear dynamics of the material optical response.

Throughout this work we will concern ourselves with the study using time-domain spectroscopic methods of nanostructured and low-dimensional materials. These materials possess interesting material physics, worth study in their own right, with potentially useful properties that could be used in future optical and electronic devices. One area explored in this work relates to the research field of integrated photonics. Integrated photonics aims to create optical and optoelectronic devices using a monolithic fabrication approach - in that functions are contained in a single chip opposed to being distributed amongst multiple discrete macroscopic components. To achieve this, material systems with the appropriate optical nonlinearity must be employed. For example, electrooptic modulators employ lithium niobate ($LiNbO_3$) due to its exceptional electrooptic coefficient which, with proper engineering, allows for fast and efficient optical modulation [7]. Identifying and characterizing new types of materials is therefore an essential enterprise for developing integrated photonic components. Chapter 2 explores the nonlinear optical properties of nanoporous sili-

con, a promising material being considered for sensors that exploit the porous nature of the material [8].

The remaining chapters in this thesis relate to the burgeoning field of two-dimensional materials and devices. Research on two-dimensional materials has exploded in the years following the first successful isolation and measurement of two-dimensional graphite (work for which the Nobel Prize in Physics was awarded in 2007 [9]). Since the initial studies on graphene, a variety of other materials have been found to have equally intriguing properties when thinned down to a few atomic layers. Most of these materials are van der Waals materials which can be isolated through a mechanical microcleavage technique that uses adhesive tapes or other processes to delaminate the crystal into atomically thin layers. The unique optical and electronic properties of these two-dimensional materials has created an opportunity to explore new types of physics and devices. Presently the materials range from gapless semi-metallic materials like graphene, to wide band-gap insulators such as the transition metal dicalcogenides. Chapters 3 and 4 present studies investigating the properties of graphene and atomically thin black phosphorus as well as devices created from these materials.

1.2 Organization of Thesis

The thesis is organized in to two main parts. The first part discusses nonlinear optics in an integrated photonics context (Chapter 2), while the latter part presents the dynamical optical properties of two-dimensional materials (Chapters 3 and 4).

Chapter 5 discusses general research trends and future directions of research.

Chapter 2.2 introduces nanoporous silicon and provides some related background material to integrated optics. A study presenting the full details of the time-resolved optial nonlinearity in this material is discussed in section 2.2.2. At the end of chapter 2 a brief summary of a related study on amorphous hydrogenated silicon is presented.

In chapter 3 a study of graphene nonlinear optics in the far-infrared region is presented (cf., section 3.1.2). A short primer on graphene's general properties with numerous references is provided in section 3.1.1. Various methods for characterizing the temporal dynamics of a graphene detector are given in section 3.1.3.

The optical properties of atomically thin layers of black phosphorus is the subject of chapter 4. This chapter has the same structure as chapter 3 in that it begins with a background on the properties of the material (cf., section 4.2) and follows up with a study of its intrinsic properties, and ends with a characterization of a device based on the two-dimensional material in question (sections 4.3 and 4.4 respectively).

An effort has been made to present the work with concision, and thus many formula are provided in-line with the main text without full derivation. Greater detail of useful results (and those not available elsewhere) are provided at the back of the thesis in the form of appendices. In addition, a thorough bibliography has been included that contains numerous reviews of the main subject areas covered in this work.

Chapter 2: Nonlinear Effects in Silicon-Based Waveguides

2.1 Overview

The term "integrated optics" refers to the idea of combining multiple types of optical components on an integrated platform (here the platform is typically taken to be a chip-based paradigm; meaning a lithographically compatible, planar substrate on which useful components can be engineered). There is also tremendous interest in combining optical and electrical functions in the same device [10–12], allowing each modality to excel in its respective functional area (e.g., high bandwidth optical guided wave structures [13] alongside high-density electronics with memory). The eventual range of device functionality is rooted in the electrical and optical properties of the material system used. A thorough understanding of the electrical and optical qualities of a material is therefore the first step towards building new types of integrated optical devices.

In this chapter we investigate two promising materials that are based upon the silicon material platform. Modifications to the base material through physical, electrical, or chemical manipulation can produce optical properties that are more favorable for silicon-based photonic devices. Silicon-based materials can take advantage of mature semiconductor manufacturing methods and potentially be com-

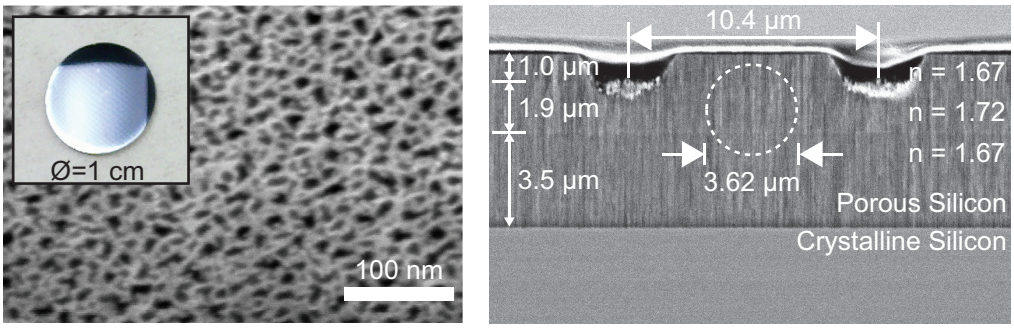

(a) (b)

Figure 2.1: Scanning electron micrographs showing nanoporous silicon structure (a) and the waveguide end facet of the type characterized in section 2.2.2. The inset in (a) shows a macroscopic image of a nanoporous silicon disc. The dashed circle in (b) shows the approximate mode dimension as estimated by a diffraction technique described in the text. The polymer cover layer (appearing as the topmost material in (b)) was not present during device characterization.

patible with the CMOS fabrication process - a requirement for seamless integration of photonic and microelectronic components.

2.2 Nanoporous Silicon

Nanoporous silicon (also called porous silicon and denoted as pSi) is a special form of silicon that has nanostructured, columnar holes (or pores) throughout the material volume. The pores form naturally via an electrochemical etching process that can be controlled by experimental parameters such as etch chemistry, wafer

doping, crystal orientation, and applied current [14, 15]. The amount of silicon removed is in direct proportion to the applied current and only removes silicon from the pore bottom; leaving previously etched layers unaffected. This surprising feature of the etch process enables the formation of 1-dimension profiles of varying silicon volume fraction by controlling the current during the etching process and thus makes porous silicon a material naturally suited for layered optical devices [16]. The resulting nanostructured silicon material possesses optical, thermal, and electrical properties that differ [15,17,18] from its crystalline form, which has generated interest in the optics community for applications such as nonlinear optical devices [19] and integrated biosensors [8,20]. Macro- and microscopic views of porous silicon are shown in the main panel and inset of Fig. 2.1(a) respectively.

The first part of this chapter (sections 2.2.1 and 2.2.2) explores the properties of the optical nonlinearity in nanoporous silicon. In section 2.2.1 the nonlinear optical properties of bulk nanoporous silicon are investigated and compared against the same figures in bulk crystalline silicon. Section 2.2.2 explores the dynamical behavior of the optical nonlinearity using a heterodyne pump-probe technique and formulates a macroscopic carrier-based model that accurately describes experimental observations.

2.2.1 Measurement of Optical Nonlinearity

Porous silicon has become a material of interest to the optics community due a number of unique optical properties and attractive features such as the ability to eas-

ily control the refractive index profile during the porous silicon fabrication process. While there have been a few [19,21,22] measurements characterizing the third-order nonlinearities of nanoporous silicon, there remains a lack of data at the important telecommunications wavelength of 1550 nm. A direct measurement of the real and imaginary components of the effective third-order nonlinearity $\chi^{(3)}(-\omega;\omega,\omega,-\omega)$ at a wavelength of 1550 nm for bulk, nanoporous silicon using the Z-scan technique [23] is presented in this section.

The nonlinear absorption and refraction coefficients, β and n_2 respectively, were characterized using the well-established Z-scan method [23]. In this measurement, the sample is longitudinally translated through the focus of a lens and the transmission is recorded as a function of the sample position. If an occluding aperture is placed after the sample, the recorded transmission will be sensitive to both nonlinear absorption and refraction [23]. A diagram of the experiment is given in Fig. 2.2. In our experiment samples are illuminated with pulses from a tunable optical parametric oscillator that is pumped by a mode-locked Ti:sapphire laser. The pulses incident on the sample have a pulse repetition frequency of 82 MHz, pulsewidth of 250 fs, 100 mW average power, and a wavelength of 1550 nm. The beam is chopped and sent through polarization control optics before reaching a focusing lens with a focal length of 100 mm. A balanced photodetection unit and lock-in amplifier are used to measure the transmission through the aperture. The sample tested in our experiment is $\langle 100 \rangle$ p-type crystalline silicon electrochemically etched to produce a 200 μm thick free-standing nanoporous silicon sample with an average pore size of 5-100 nm [22]. The reference sample used in our experiment

is a 380 μm thick, 5-10 kΩ-cm, double side polished, ⟨100⟩ bulk crystalline silicon wafer treated on both sides with an antireflective coating optimized for near infrared wavelengths.

With the exception of the sample thickness and reflection coefficient differing between the porous and crystalline silicon, the measurements were performed under nearly identical conditions. Figure 2.2(a) shows the measured transmission through the sample without an aperture present, a configuration that is sensitive only to nonlinear absorption, for both crystalline and nanoporous silicon. Near the focus (zero on the abscissa in Fig. 2.2(a)) there is a dip in the transmission that corresponds to increased nonlinear absorption. The nonlinear absorption and refraction coefficients are estimated from the measurement data with the partially occluding aperture present (shown in Fig. 2.2(b)). The nonlinear parameters are fit using models developed in references [23, 24].

The nonlinear parameters fit from the data presented in Fig.2.2 indicate that the nonlinear coefficients for nanoporous silicon are enhanced over those of crystalline silicon with the ratios $\beta_p/\beta_c = 6.9$ and $n_{2,p}/n_{2,c} = 17.4$ being larger than unity. The nonlinear figure of merit $F = n_2/\lambda\beta$ was also calculated, giving $F_c = 0.27$ and $F_p = 0.69$ (subscripts "c" and "p" denote crystalline and porous materials). A percent error of around 20% is estimated for all figures. The primary source of error in the measurement is believed to originate from surface inhomogeneities in the porous silicon and uncertainty in estimating the optical intensity inside the samples. The above measurements used linear polarization to investigate the nonlinear coefficients. While we observed the expected anisotropy present in crystalline silicon

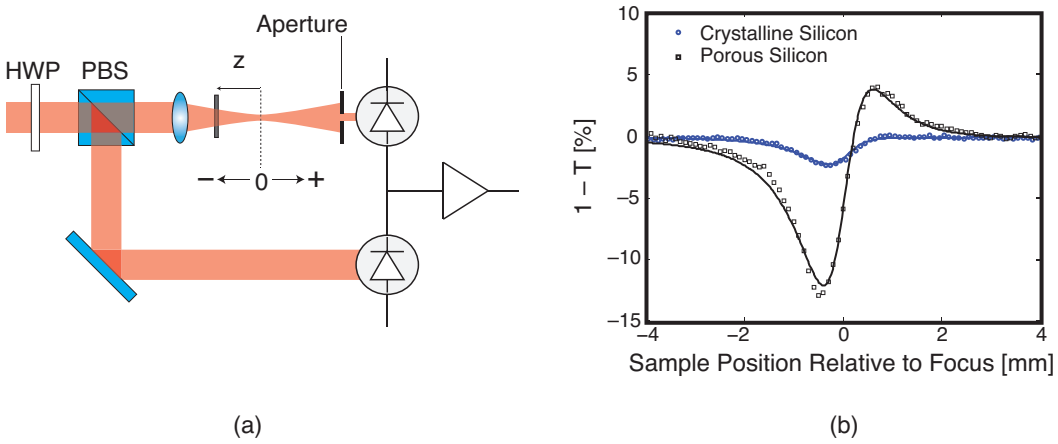

Figure 2.2: (a) Schematic of "Z-Scan" measurement. HWP: Half-wave plate, PBS: Polarizing beam splitter. (b) "Z-Scan" measurements of nanoporous silicon (black squares) and crystalline silicon (blue circles). The figure plots relative transmission versus sample position. The solid lines are theoretical curves used to fit the data.

for light linearly polarized at particular angles with respect to the crystallographic axis [25], no such anisotropy was observed in the porous silicon sample.

2.2.2 Heterodyne Pump-Probe

In the section 2.2.1 a single beam measurement was used to characterize the optical nonlinearity of nanoporous silicon. This approach produces a single, complex valued number to characterize the nonlinearity of the material which, while useful, reveals little about the physical mechanisms producing the nonlinear behavior. The following sections describe measurements that resolve the time domain behavior of

the nonlinearity; illuminating the various physical processes underlying the optical nonlinearity.

2.2.2.1 Nanoporous Silicon Waveguides

The time-domain measurements described in section 2.2.2.2 are carried out in guided wave structures. Besides being one of the most technologically ubiquitous structure in photonics [26], optical waveguides have several attractive features that make them ideal structures for studying nonlinear behavior. The first useful property is the high confinement of the optical mode, which allows large intensities (GW/cm^2) to be readily achieved over a large interaction length (the length of the waveguide for sufficiently low linear loss). A second important feature for phase sensitive measurements involving multiple beams is that each beam will be projected onto the same spatial mode in single-mode structure. This ensures that sensitive phase information related to the nonlinearity being studied is not aberrated by spatial structure introduced by the preceding optical system or by slight misalignment of optical beams.[1]

The waveguides tested in this study utilized a current-controlled electrochemical etch that produced a buried optical slab waveguide with a 1.9 μm core with an effective refractive index of $n = 1.72$ surrounded on each side by $n = 1.67$ cladding

[1]The waveguide measurement is also sensitive to beam misalignment in that the coupling of light into the waveguide depends critically on the relative position of the input beam and the waveguide end-facet. This type of misalignment only affects the size of the measured signal and does not introduce spurious features into the data as is the case for the free-space experiment.

layers. To confine the optical mode in the second transverse direction, a computer controlled laser ablation [8] writing system was used to fabricate two parallel trenches on the surface of the porous silicon wafer having a length and spacing that define respectively the length and width of the optical waveguide. The waveguide refractive index profile and width are designed to support single mode operation at 1560 nm. An optical micrograph showing the device fabricated as described above is shown in Fig. 2.1(b). Full details of the pSi optical waveguide fabrication and characterization process are given in [8, 27]. A nanoporous silicon structure representative of the type considered in this study is shown in the top-down scanning electron micrograph shown in Fig. 2.1(a).

The linear propagation loss of the waveguide was estimated by performing cutback measurements [28] for devices of different lengths. This approach produced a loss estimate of 13.5 dB/cm; indicating 7.7 dB of total loss attributed to linear absorption for the 0.57 cm long waveguide. There are several factors that contribute to this linear loss, including Rayleigh scattering from the nanoporous structure, edge roughness from the laser-patterned waveguide boundaries, residual free-carrier absorption, and transverse evanescent leakage. Inverse transmission measurements [29] were used to estimate the free-space input coupling loss and the two-photon absorption coefficient, β_{2PA}, and found to be 5.25 dB and 1.15 cm/GW respectively. The optical mode size was estimated by a observing the far-field diffraction of the the light exiting from the back facet of the waveguide. The measured beam divergence is nearly symmetric and Gaussian, from which a mode size of 10.27 $\mu\mathrm{m}^2$ is inferred. The inferred mode profile is overlaid on the micrograph in Fig. 2.1(b).

2.2.2.2 Time-Domain Measurements and Discussion

To characterize the nonlinear optical properties of the waveguides, a two-frequency pump-probe heterodyne technique was used. The experimental setup used in this study differs slightly from more conventional pump-probe heterodyne techniques [30, 31] and is diagrammed in Fig. 2.3. As with traditional pump-probe heterodyning, the two-frequency approach uses a reference pulse, chopped pump pulse, and probe pulse that are sequentially launched into the waveguide, with a variable delay τ between the pump and probe pulse. After traversing the waveguide, the reference and probe pulses are temporally overlapped at the detector using a Michelson interferometer to produce a heterodyne signal (see Fig. 2.3). The amplitude and phase of the probe pulse is modified due to the presence of the pump in the sample, thus altering the magnitude and phase of the heterodyne signal measured by the lock-in amplifier. Measuring the amplitude and phase change as a function of pump delay time (τ) gives the transient absorption and phase response, respectively.

The chopping of the pump beam introduces additional tones above and below the heterodyne frequency. By using a lock-in amplifier that is capable of measurement at two different reference frequencies (the heterodyne frequency and the first upper sideband due to the chopping), it is possible to simultaneously determine both the magnitude and phase of the probe pulse. The dual-frequency measurement described here determines the only the relative changes in intensity and phase that are caused by the chopping of the pump signal, and is hence insensitive to slow phase fluctuations and drift that otherwise plague heterodyne measurements.

The pump pulse is produced by a 100 MHz mode-locked fiber-laser (Menlo Systems), and the probe and reference pulses are obtained from a second, similar mode-locked laser. The two lasers have intra-cavity piezoelectric actuators that allow for fine adjustment of their repetition rates. Using external synchronization circuitry, the two lasers are locked together with a small difference frequency $\delta f =$ 0.1 mHz, thereby producing a slow, linear sweep of the time delay τ between the pump and probe. This allows for large delays (nanoseconds for the system used in this study) without the use of mechanical delay lines [32]. Both lasers are co-polarized and have a center wavelength of 1.56 μm and a pulsewidth of 100 fs (FWHM). The time delay T between the probe and reference is set to 830 ps using a fixed external delay line. This delay limits the maximum pump-probe delay that can be unambiguously measured in the experiment. The reference and probe pulses are derived from the same laser and are frequency blue-shifted by frequencies of $f_D = 35$ MHz and $f_D + f_H = 35.0625$ MHz respectively using a pair of acousto-optic frequency shifters (AOFS). The difference frequency between the two AOFSs defines the heterodyne frequency, which was set to $f_H = 62.5$ kHz for this study. The AOFS causes the probe and references pulses to broaden to approximately 700 fs, as determined by autocorrelation measurements at the output. The pump beam, which is chopped at frequency $f_c = 1$ kHz, is combined with the probe and reference beams and passed through a polarizing beam cube, resulting in an horizontally polarized beam impinging on the waveguide end facet. The ratio of the pump power to the combined probe and reference beam power (the probe and reference beams are equipotent) can be controlled with half-wave plates (HWP)

prior to beam combination and ranged between 35 and 70 for the measurements reported here.

The light is next free-space coupled into the TE eigenmode of the waveguide using an 0.65 NA 60× aspheric lens. The electric field of the TE mode is perpendicular to the principal direction of the columnar pores, resulting in a lower linear propagation loss in comparison to the TM eigenmode. At the back facet of the waveguide, the emerging light is re-collimated and directed into a Michelson interferometer with a temporal path difference of T, chosen to temporally overlap the reference and probe pulses. Both outputs of the interferometer are differentially detected in a balanced photoreceiver to reduce the large common mode pump signal. A dual-phase digital lock-in amplifier (Signal Recovery 7270) is used to simultaneously detect both quadratures at both the heterodyne frequency, f_H, and at the first upper sideband of the heterodyne, $f_H + f_C$, which is generated by a nonlinear interaction with the pump pulse in the waveguide. The AOFSs, optical chopper, and lock-in reference signal are all derived from a common 4-channel synthesizer (Novatech 409B), thereby ensuring a common phase relation between the heterodyne and chopping frequency. The Appendix explains how these two-frequency measurements can be used to calculate the transient change in relative intensity and phase in a manner that is robust to noise, including a complete derivation of the relevant equations.

The experimental method described above was used to measure the time domain characteristics of the nonlinear optical properties of the pSi waveguides. Figure 2.4(a) shows the measured transient intensity change of the probe, $(\Delta I/I)$, as a

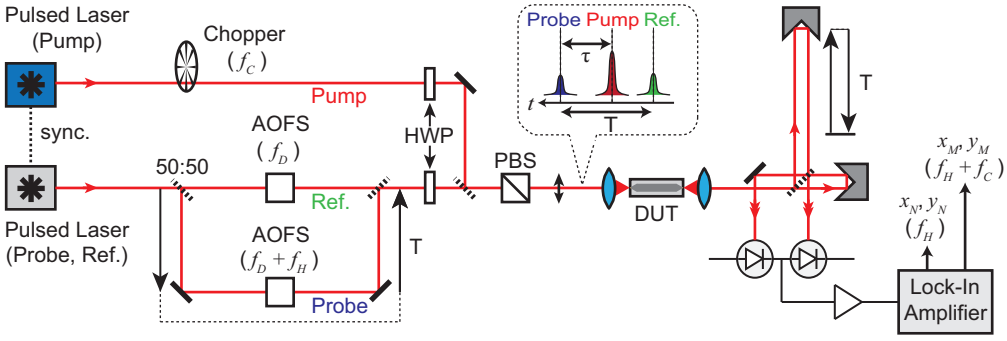

Figure 2.3: Diagram of pump-probe experiment used in this study. The inset shows the relative timing of pulses incident on the device under test (DUT). A dual-phase lock-in amplifier measures the in-phase and quadrature components (x and y respectively) at two different frequencies f_H and $f_H + f_C$. AOFS: acousto-optic frequency shifter; HWP: half waveplate; PBS: polarizing beam splitter.

function of the pump-probe delay, τ. The inset shows an enlarged view near zero delay for three different coupled pump intensities. The absorption of the probe pulse is caused by a combination of instantaneous two-photon absorption of the pump and probe signal and subsequent free-carrier absorption caused by the associated electrons and holes.

The transient data reveals that multiple recombination time scales exist for the pSi waveguides measured in this study, as has been previously observed in photoluminescence studies in bulk pSi [33]. The intensity exhibits an initial exponential recovery with a $1/e$ recovery time of $\tau_c = 10$ ps, as depicted in the inset to

Fig. 2.4(a), followed by a slower recovery. The 90% recovery time for free-carrier absorption in the pSi waveguides was found to be 100 ps. This result is several times faster than absorption-based measurements in conventional SOI waveguides of comparable geometry [27, 34] which have lifetimes on the scale of τ_c =1 ns, and is orders of magnitude faster than the carrier lifetime in bulk silicon. The rapid recombination time is believed to originate in reduced mean free path lengths in the carrier diffusion process due to the presence of local surface recombination sites in the nanoporous material [33].

Figure 2.5(a) plots the corresponding phase as a function of delay, which shows both an ultrafast decrease caused by instantaneous cross-phase modulation, followed by a slower positive phase shift caused by free-carrier dispersion. As with the intensity measurements, the free-carrier response exhibits a 90% recovery time of approximately 100 ps.

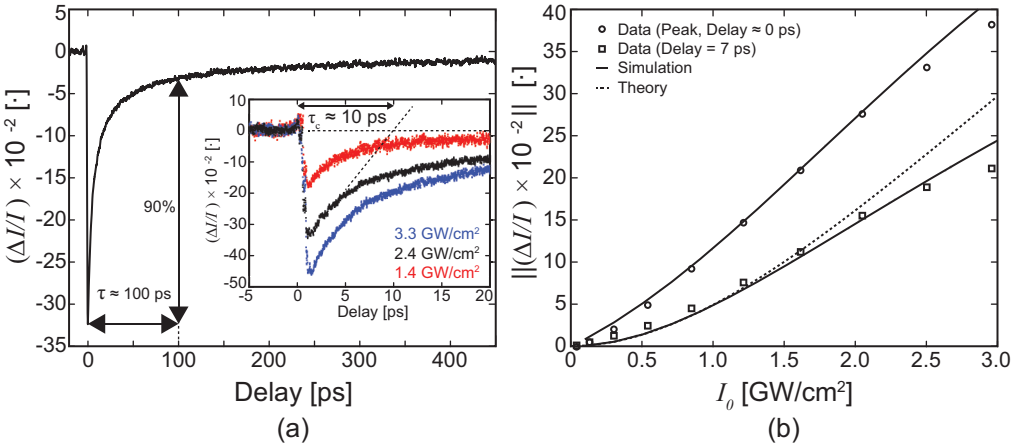

Figure 2.4: (a) Transient normalized change in probe intensity for coupled pump intensity of 2.4 GW/cm^2. The inset shows a zoomed view of transient near zero delay for different coupled pump intensities (1.4, 2.4, 3.3 GW/cm2 top to bottom). An effective time constant for the initial recovery is also indicated on the inset. (b) Relative change in probe intensity for delays $\tau = 0$ ps (top curve) and $\tau = 7$ ps (bottom curve) for varying coupled pump intensity. The theoretical curve (dotted line) is an approximate solution valid at low intensities.

In order to quantify the strength of the instantaneous and carrier-based nonlinearities, we measured the dependence of the transient magnitude and phase on the pump intensity. Figures 2.4(b), 2.5(b) show the relative change in intensity and the change in phase as a function of the coupled pump peak intensity, for fixed values of pump-probe delay. In these plots we examine the intensity and phase dependence near zero delay, where we expect ultrafast effects such as two-photon absorption

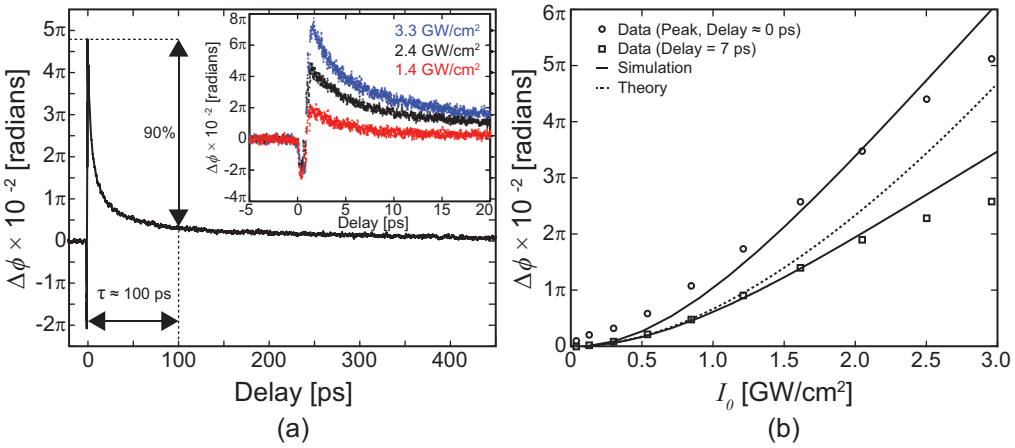

Figure 2.5: (a) Change in phase for coupled pump intensity of 2.4 GW/cm^2. The inset shows a zoomed view of transient change in phase near zero delay for different intensities (1.4, 2.4, 3.3 GW/cm^2 bottom to top). (b) Change in phase for delays $\tau = 0$ ps (top curve) and $\tau = 7$ ps (bottom curve) for varying coupled pump intensity. The theoretical curve (dotted line) is an approximate solution valid at low intensities.

and the optical Kerr effect to dominate the response, and also the at 7 ps, where we anticipate effects predominantly from free-carriers generated by the strong pump.

The data was modeled by numerically solving the coupled equations of evolution for the reference, pump, and probe pulses in the presence of ultrafast optical nonlinearities and carrier-based effects. The equation governing pulse propagation is given by:

$$\begin{aligned}\frac{\partial}{\partial z}u(z,t) = &\left[-\frac{\alpha}{2} + \left(i\frac{\omega}{c}n_2 - \frac{\beta_{\text{2PA}}}{2}\right)\frac{|u(z,t)|^2}{A_{\text{eff}}}\right. \\ &\left. - \left(i\frac{\omega}{c}\Delta n_{\text{FCD}}(z,t) + \frac{1}{2}\Delta\alpha_{\text{FCA}}(z,t)\right)\right]u(z,t)\end{aligned} \tag{2.1}$$

where $u(z,t)$ represents the field envelopes including the pump, reference, and probe pulses, α is the linear absorption coefficient, n_2 is the Kerr coefficient, β_{2PA} corresponds to the two-photon absorption coefficient, and A_{eff} is the effective area of the optical mode.

The coefficients $\Delta\alpha_{\mathrm{FCA}}$ and Δn_{FCD} are related to the free-carrier population through the following relations:

$$\Delta\alpha_{\mathrm{FCA}}(z,t) = \sigma_{\mathrm{FCA}}\Delta N(z,t) \tag{2.2}$$

$$\Delta n_{\mathrm{FCD}}(z,t) = k_{\mathrm{FCD}}\Delta N(z,t) \tag{2.3}$$

where σ_{FCA} is the free-carrier absorption cross section and k_{FCD} is the free-carrier dispersion coefficient. The term $\Delta N(z,t)$ is the excess carrier density present in the waveguide caused by the strong pump pulse. The carrier density is related to the pump field in the waveguide by:

$$\frac{\partial}{\partial t}\Delta N(z,t) = \frac{\beta_{\mathrm{2PA}}}{2\hbar\omega}\left[\frac{|u(z,t)|^2}{A_{\mathrm{eff}}}\right]^2 - \frac{\Delta N(z,t)}{\tau_c} \tag{2.4}$$

with τ_c being the carrier recombination time, which was inferred from the transient measurements of Figs. 2.4, 2.5. Second-order dispersion is excluded in Eq. (1) because the waveguides considered are not long enough to cause significant broadening of the 100 fs pulses used in the measurement. The Raman contribution to the nonlinear susceptibility was omitted in Eq. (1) because the pulses used in this experiment do not have sufficient bandwidth or spectral separation to efficiently couple through the vibrational modes of the crystal. Earlier measurements have shown that the Raman spectrum in porous silicon is only moderately broadened

and shifted and otherwise retains many of the characteristics of the original silicon substrate [35].

The split-step Fourier method was implemented to solve the coupled equations for all pulses in the experiment and produce numerical $(\Delta I/I)$ and $\Delta\phi$ curves. The fitting was done simultaneously for all the data given in Figs. 2.4(b), 2.5(b) and are shown as solid black lines. Fit parameters produced from the numerical solution give $\sigma_{\mathrm{FCA}} = 137 \times 10^{-17}$ cm^2 and $k_{\mathrm{FCD}} = 13.5 \times 10^{-21}$ cm^3. The fit value for the free-carrier absorption in pSi waveguides is two orders in magnitude larger than those for SOI waveguides while the free-carrier plasma dispersion is approximately 3 times larger. For bulk silicon, the free-carrier parameters have been reported in the literature as [36] $\sigma_{\mathrm{FCA,Si}} = 1.45{\times}10^{-17}$ cm^2 and $k_{\mathrm{FCD,Si}} = 3.5{-}7.5{\times}10^{-21}$ cm^3 [27,37]. We note that these measurements are consistent with earlier reports that also show a significant enhancement in the free-carrier parameters compared to crystalline silicon [27]. Unlike earlier measurements, which relied upon indirect estimates of the free-carrier dispersion and nonlinear refraction coefficients based only on spectral measurements, the present approach provides a direct measurement of the temporal phase response, which enables a less ambiguous determination of these parameters. Also notable in the data is the optical Kerr effect which is apparent immediately after zero delay in the inset of Fig. 2.5(a) and appears as a negative change in phase. Estimates for the Kerr coefficient produced by the full numerical solution gives $\mathrm{n_2} = 6.7 \times 10^{-14}$ cm^2/W; comparable to that of crystalline silicon [27].

Approximate solutions for the probe field, and hence approximate $(\Delta I/I)$ and $\Delta\phi$ curves, can be found for delay values larger than zero delay ($\tau \gg T_0$), once the

strong pump pulse arriving at time zero is no longer present. Assuming weak probe and reference pulses, the probe pulse evolution dynamics are dominated primarily by the pump generated free-carrier population. Thus for times after the initial transient, the change in phase and relative intensity should be related to the carrier population. For carrier lifetimes $\tau_c \gg T_0$, the initial carrier population can be determined by integrating the pump intensity squared over the total duration of the pump pulse and will be a function of the initial coupled pump power and position. Furthermore, the net change in phase or relative intensity is given by the integral of the carrier population over the length of the waveguide. An approximate solution for the pump is assumed, which incorporates linear loss and two-photon absorption effects and assumes a $\mathrm{sech}^2\left(t/T_0\right)$ temporal dependence. The probe evolution is then given by the solution of Eq. (2.1) with only linear absorption and carrier-based effects included. The approximate probe field is given by:

$$u_{\mathrm{probe}}(t) = u_{0,\mathrm{probe}}(t-\tau)\exp\left(-\frac{\alpha}{2}L\right)\exp\Bigg\{-\left(\frac{1}{2}\sigma_{\mathrm{FCA}} + i\frac{\omega}{c}k_{\mathrm{FCD}}\right) \times\left[\frac{\beta_{\mathrm{2PA}}}{2\hbar\omega}\int_0^L\int_{-\infty}^{\tau} I^2_{\mathrm{pump}}(z,t';I_{0,\mathrm{pump}})dt'dz\right]e^{-t/\tau_c}\Bigg\} \tag{2.5}$$

In the above expression $u_{0,\mathrm{probe}}$ is the temporal field envelope, $I_{\mathrm{Pump}}(z,t';I_{0,\mathrm{Pump}})$ is the pump intensity ansatz which has linear and two-photon absorption effects included, and $I_{0,\mathrm{Pump}}$ is the initial coupled pump input intensity. From the probe field solution, $(\Delta I/I)$ and $\Delta\phi$ can be calculated and are plotted as a dashed line in Figs. 2.4(b), 2.5(b). The theoretical curves are in excellent match to the numerical solution and data taken at 7 ps delay for low intensities; supporting the claim that the observed effect is predominantly the result of free-carriers generated by

the pump. For small coupled input intensities, the 7 ps delay data and theoretical curves are quadratic with power as expected. For larger values of intensity, the pump is depleted by two photon absorption and a sub-quadratic power dependence is observed. At higher intensities ($\geq$ 1.5 GW/cm^2) the theoretical and numerical solution diverge, with the theoretical curves over-predicting the nonlinear effects. This is expected as the theory does not incorporate the nonlinear absorption of the pump from self generated carriers, which further limits the amount of carriers generated at high intensities. A more detailed explanation of Eqn. 2.5 is given in Appendix B.

2.3 Amorphous Hydrogenated Silicon

Amorphous hydrogenated silicon (often denoted as a-Si:H) is a depositable silicon-based material that has attracted enormous interest in the optics community for use in nonlinear optical devices. The material is fabricated using low temperature (300 ^{o}C) plasma-enhanced chemical vapor deposition which allows for the a-Si:H to be deposited on top of other pre-existing structures (such as microelectronic circuits defined using a CMOS process). Recent studies have indicated a large optical nonlinearity exists in this material [38, 39] suggesting that a-Si:H would serve as an ideal material for integrated photonics circuits. Previous work aiming to characterize the optical properties of this material, however, has not yet produced a definitive picture.

The following section (section 2.3.1) discusses heterodyne pump-probe mea-

surements on both crystalline silicon waveguides and amorphous hydrogenated silicon waveguides. These measurements were part of a larger study [40] that employed a number of experimental techniques [22, 41, 42] to understand the nonlinear optical response of a-Si:H.

2.3.1 Heterodyne Pump-Probe

Heterodyne pump-probe measurements were carried out on a-Si:H and crystalline Si waveguides. Due to the small transverse dimensions of these structures (of order 10^2 nm), the term nanowire is typically used. Nanowires are an attractive structure as the small transverse width makes possible large optical intensities within the guiding structure assuming sufficiently high index contrast and diminished free-carrier lifetimes due to the short path length to surface recombination sites [34]. Cross-sectional waveguide dimensions and optical mode profiles (as calculated by a full-vector mode solver [43]) for the structures presented in this section are shown in Fig.2.6(a) and (b).

Using the experimental technique described in sections 2.2.2 and 2.2.2.2, crystalline silicon and a-Si:H nanowires were measured. Full details of the characterization of each waveguide (linear loss, coupling efficiency, etc.) are given in [40] and are similar to those described in section 2.2.2.2.

Figure 2.7 shows time-resolved $\Delta\phi$ transients for the a-Si:H and c-Si waveguides, together. We note that the zero-delay in these pictures is artificially registered to the extremum of the phase transient ($\tau = 0$ does not necessarily correspond to

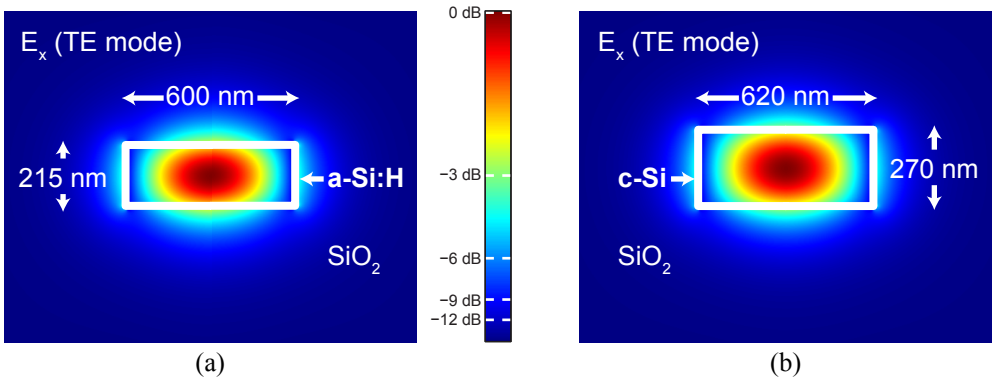

(a) (b)

Figure 2.6: Crystalline silicon (a) and amorphous hydrogenated silicon (b) nanowire cross-section and mode profile. Each guiding structure is buried in silicon dioxide.

perfect temporal overlap of the pump and probe). Rough estimates for the optical power coupled into the waveguides were obtained by performing separate in-situ nonlinear transmission experiments ("inverse transmission" experiments) using the same free-space coupling setup. For the a-Si:H experiment, we estimate the average probe power launched into the waveguide was 0.3 μW while the average launched pump power was 264 μW. For the c-Si experiment, we estimate the average probe power launched into the waveguide was 0.46 μW, while the average launched pump power was 431 μW. As is clear in Fig. 2.7, the non-instantaneous phase transients in the a-Si:H and c-Si waveguides have opposite signs. or the crystalline silicon, we expect a negative phase contribution from the instantaneous portion of the optical nonlinearity (occurring around time zero) and a positive nonlinear hase occurring at later times due to the free-carrier plasma generated by the strong pump pulse.

Similar to the crystalline silicon nanowire, the a-Si:H waveguide has a negative instantaneous nonlinearity corresponding to the optical Kerr effect. In contrast to crystalline silicon, however, the a-Si:H structure displays a long-lived negative nonlinear phase that cannot be attributed to the dispersive effects of free carriers.

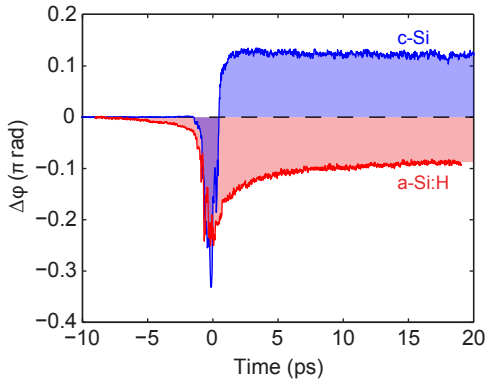

Figure 2.7: Time resolved phase transients for the a-Si:H (red) and c-Si (blue) nanowires. The instantaneous (long-lived) nonlinear phase is same (oppositely) signed for each material.

Next the power scaling of the nonlinear absorption and refraction was studied for each material. Similar to the plots shown in Fig. 2.4(b) and Fig. 2.5(b), the changed in relative intensity and phase was considered after the arrival of the pump probe at a probe delay of 5 ps. Figure 2.8 shows the nonlinear intensity and phase change as a function of probe delay on a log-log plot to better contrast the power dependence of the nonlinearity in each material. The amount of power coupled into each type of nanowire is different and the power axis is thus normalized to the other data points within each data set (i.e., the relative size of the nonlinearity for

each material cannot be directly compared on this plot). In Fig. 2.8(a) the relative intensity is shown for the two materials. A saturation behavior is observed since we are plotting the relative intensity which is proportional to $1 - \exp(-\alpha(I, L))$. Thus for small values of the argument we are plotting $\alpha(I, L)$ whereas at larger values of the argument higher order terms from the expansion of the exponent are included and produce a saturation effect. The data for the c-Si and a-Si:H are shown to follow respectively quadratic and linear trends. This is anticipated for the carrier based nonlinearity in the crystalline silicon nanowire which should follow an effective $\chi^{(5)}$ nonlinearity. The linear in power dependence of the amorphous silicon follows the trend of a $\chi^{(3)}$ type nonlinearity and cannot be associated with free-carrier absorption. Figure 2.8(b) shows the same trend is also true of the nonlinear phase. It is noted that no saturation effect is expected for the phase as the quantity being plotted is the absolute value of the *argument* in the exponential $\exp(\Delta\phi(I, L))$.

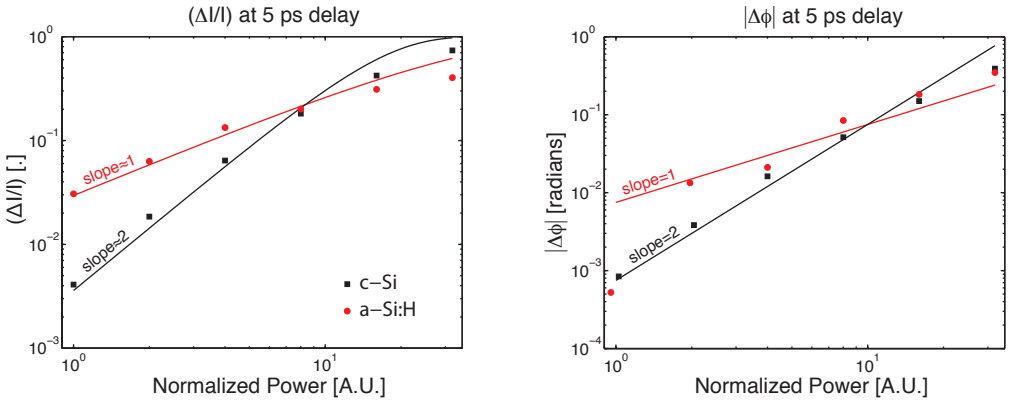

Figure 2.8: (a) Plot of $(\Delta I/I)$ versus normalized power for crystalline and amorphous hydrogenated silicon (black squares and red circles respectively). Solid lines show linear and quadratic power dependence with saturation behavior. (b) Absolute value of $\Delta\phi$ for crystalline and amorphous hydrogenated silicon. Solid lines show linear and quadratic power dependence.

Chapter 3: Dynamics in Graphene and Graphene-Based Devices

3.1 Overview

Graphene refers to a single atomic layer of carbon atoms that form a planar honeycomb lattice. The linear, gapless band structure of the single-layer graphene results in a material with a nearly wavelength independent absorption of electromagnetic radiation; making graphene an ideal candidate for broadband photodetection. Other properties such as high carrier mobility and the ability to electro-statically control the carrier concentration in the atomic monolayer, have made graphene an intensely studied material for a host of optical and electronic applications [44]. Graphene has also been considered an ideal material for plasmonics as the field-effect in graphene would allow for tunability and control of the plasmon resonance [45].

In this chapter we present time-domain studies of the optical nonlinearity in graphene (section 3.1.2). This investigation discusses the graphene nonlinear optical properties that have been studied using terahertz pump-probe spectroscopy. A complete understanding of the light-matter interaction at terahertz frequencies is of significant fundamental interest and technological importance. The chapter concludes by highlighting an application of graphene as a broadband photodetector with an emphasis on time-domain techniques that can be used to characterize

the temporal reponse of electrically connected graphene. The photodetector characterization was part of a larger study carried out by X. Cai, et al. [46]. Before proceeding, section 3.1.1 offers a brief primer that presents the essential characteristics of graphene relevant to the work discussed in this chapter. For a more complete discussion of graphene properties and physics, please see references [47, 48].

3.1.1 Overview of Electrical and Optical Properties of Graphene

The unique electrical and optical properties of graphene originate from its two-dimensional structure. Graphene is an atomically thin layer of carbon atoms arranged in a hexagonal honey-comb lattice as shown schematically in Fig. 3.1(a). The hybridization of the out of plane p_z orbitals form π-bonds and are predominantly responsible for the unique electronic band structure as shown in Fig. 3.1(b). The inset of the figure shows the gapless, linear dispersion relationship that are centered around the **K**-points in the Brillouin zone.

The band structure plotted in Fig. 3.1(b) are determined from a tight-binding model with parameters from [49]. Following the original work of Wallace [50] and assuming the second order hopping parameter is small ($\gamma_0' = 0$, [50]) gives:

$$\begin{aligned} E_{\pm}(\mathbf{k}) &= \pm\gamma_0 |\textstyle\sum_j e^{i\mathbf{k}\cdot\mathbf{n}_j}| \\ &= \pm\gamma_0 \sqrt{3 + f(\mathbf{k})}, \end{aligned} \tag{3.1}$$

where $f(\mathbf{k}) = 2\cos(\sqrt{3}ak_y) + 4\cos(3ak_x/2)\cos(\sqrt{3}ak_y/2)$. Inclusion of the next-

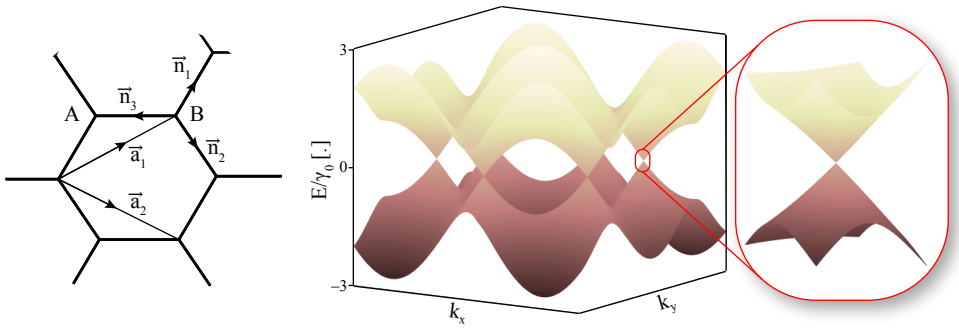

Figure 3.1: (a) Atomic structure of single-layer graphene. The lattice vectors are given by $\mathbf{a}_1 = (a/2)(3, \sqrt{3})$ and $\mathbf{a}_2 = (a/2)(3, -\sqrt{3})$ where the spacing between two carbon atoms is given by $\overline{AB} = a \approx 1.42\ \mathring{A}$. Nearest neighbor vectors are given by: $\mathbf{n}_1 = (a/2)(1, \sqrt{3})$, $\mathbf{n}_2 = (a/2)(1, -\sqrt{3})$, and $\mathbf{n}_3 = a(-1, 0)$. (b) Band structure of single layer graphene calculated using π-bond tight-binding model [49]. At several points in the Brillouin zone the dispersion relation forms a linear, gapless Dirac cone (shown inset).

nearest hopping ($0.02 \leq \gamma_0'/\gamma_0 \leq 0.2$) introduces an asymmetry into the band structure [47]. Around the Dirac point the dispersion relationship is approximately linear. Expanding around the Dirac points ($\mathbf{k} = \mathbf{K} + \delta\mathbf{k}$, where $\mathbf{K} = (2\pi/3a)(1, 1/\sqrt{3})$) to first order gives the following linear relationship:

$$E_{\pm}(\delta\mathbf{k}) = \pm v_F \hbar |\delta\mathbf{k}|, \tag{3.2}$$

where $v_F = (3/2)\gamma_0 a/\hbar \approx 10^6$m/s for a value of $\gamma_0 = 2.75$eV [49]. The work presented here will be in the low-energy limit where the dispersion relationship is well approximated by Eqn.3.2.

The consequences of the linear dispersion in graphene impacts its physical characteristics. For example, the density of states for two-dimensional graphene is calculated using 3.2 to be:

$$g(E) = \frac{dN}{dE} = \frac{2|E|}{\pi v_F^2 \hbar^2}. \tag{3.3}$$

This result includes a spin and valley degeneracy factor of four and is distinct from the usual $g(E) \propto \sqrt{E}$ dependence typically encountered in bulk semiconductors. The density of states is used to calculated many of the physical properties of a material, including the conductivity, which we consider next.

The conductivity of graphene has a broadband response due to its linear dispersion relation. The conical nature of the band structure indicates that photons with a broad range in energy can be absorbed by the material via direct interband transitions. This is different from gapped semiconductor materials which only allow interband transitions for photons with energies larger than the bandgap. In addition to interband transitions, graphene can also exhibit a phonon assisted free-carrier absorption which obeys a Drude-like response. The absorption is proportional to the the real part of the conductivity (see C.12), and is given by [51]:

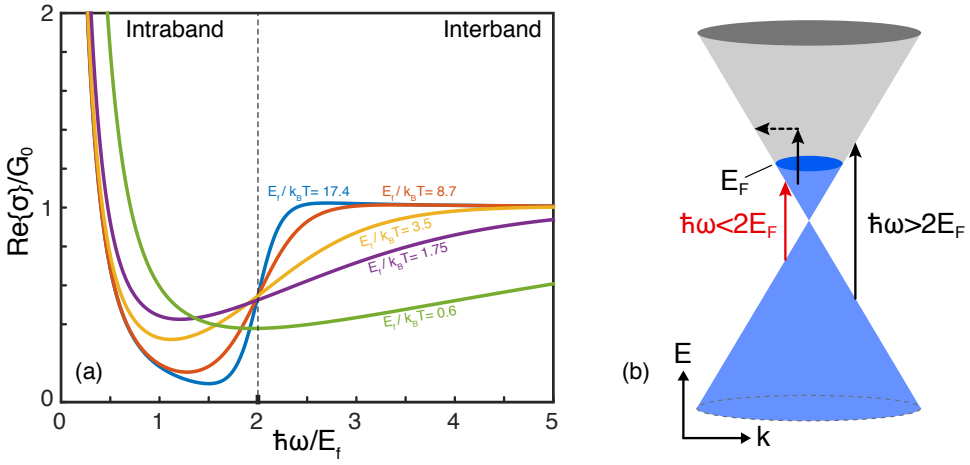

Figure 3.2: (a) A plot of the real part of the normalized conductivity as a function of photon energy. The curves show a sharper transition at lower temperatures around $\hbar\omega \approx 2E_F$. (b) Schematic diagram of the absorption processes. Direct interband absorption is energy and momentum matched (vertical transition for $\hbar\omega > 2E_F$), phonon or defect assisted (to conserve momentum) intraband absorption is shown as a vertical plus dashed horizontal line. For incident photon energies below $2E_F$ the transition is Pauli blocked (shown as red vertical arrow).

$$\frac{\mathrm{Re}\left(\sigma(\omega)\right)}{G_0} = \frac{8k_BT}{\pi\hbar} \times \ln\left(2\cosh\left(\frac{E_F}{2k_BT}\right)\right)\frac{\tau}{\omega^2\tau^2+1} + \frac{1}{2}\left[\tanh\left(\frac{E_F+\hbar\omega/2}{2k_BT}\right) - \tanh\left(\frac{E_F-\hbar\omega/2}{2k_BT}\right)\right]. \tag{3.4}$$

The real part of the conductivity is plotted in Fig.3.2(a) as a function of photon energy for a variety of temperatures. Here we can distinctly see the role of inter-

and intraband processes at different photon energies with respect to the chemical potential. A diagram in Fig.3.2(b) conceptually visualizes these processes.

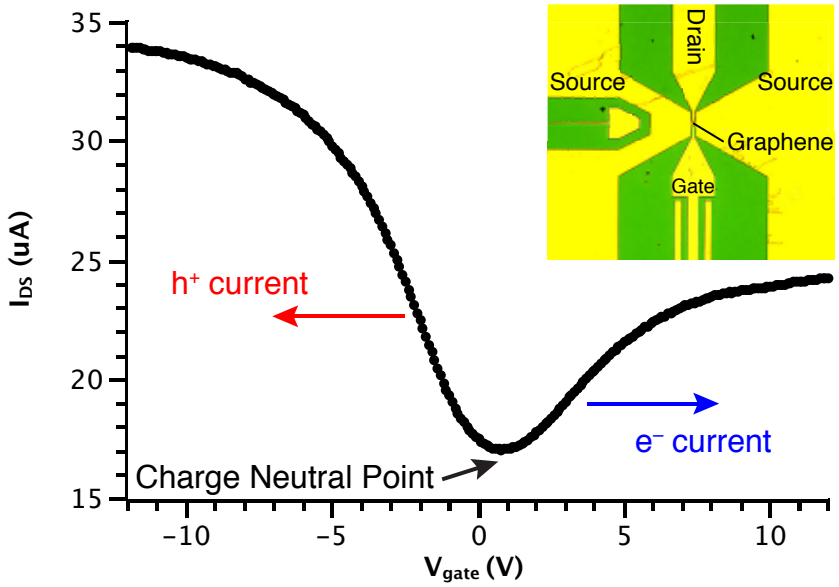

Figure 3.3: Curve showing change in source-drain current through a graphene channel as a function of back gate voltage due to the field-effect. The graphene channel was part of in a high-frequency graphene mixer (inset) that employs a top gate with a split-source electrode configuration.

Another important feature of graphene is the presence of a field effect. Through the application of an external field the carrier density in the material can be modified. The ambipolar nature of this effect means that the material behaves symmetrically around a charge neutral point (c.f. Fig. 3.3), with either electrons or holes being the majority carrier depending on the gate voltage. This effect has been used to study

the optical properties of graphene as well as for optical devices, including modulators and mixers [52]. Perhaps one of the nost attractive properties of graphene includes a high intrinsic mobility, which offers a direct pathway for the development of high speed electronic devices. Measured values for the mobility of graphene indicate it may be possible to achieve values of $200,000\,\mathrm{cm^2V^{-1}s^{-1}}$ [53] at room temperature.

In addition to the general review articles given previously, a discussions on the synthesis of graphene and its thermal and mechanical properties are given in the following articles [54–56].

3.1.2 Nonlinear Optics in Multilayer Epitaxial Graphene

Understanding the optical response of graphene at terahertz frequencies is of critical importance for designing graphene-based devices that operate in this frequency range. Here we present a terahertz pump-probe measurement that simultaneously measures both the transmitted and reflected probe radiation from multilayer epitaxial graphene, allowing for an unambiguous determination of the pump-induced absorption change in the graphene layers. The photon energy in the experiment (30 meV) is on the order of the doping level in the graphene which enables the exploration of the transition from interband to intraband processes, depending on the amount of pump-induced heating. Our findings establish the presence of a large, photoinduced reflection that contributes to the change in sign of the relative transmitted terahertz radiation, which can be purely positive or predominantly negative depending on the pump fluence, while the change in absorption is found negative

at all fluences. We develop a hot carrier model that confirms the sign-reversible nature of the relative transmitted terahertz radiation through the graphene multilayer and determine that this behavior originates from either an absorption-bleached or reflection-dominated regime. The theoretical results are incorporated into a model utilizing an energy balance equation that reproduces the measured pump-probe data. These findings, which extend to mid- and far infrared frequencies, show the importance of considering reflection in graphene-light interactions and have implications for the design of future terahertz photonic components.

3.1.2.1 Introduction

Graphene has attracted tremendous attention as a material suitable for a variety of applications due to its linear and gapless band structure and high carrier mobility. These properties make graphene particularly suitable for applications in the terahertz region, where there are notoriously few materials that interact strongly with electromagnetic radiation [44, 57, 58]. Significant effort has been devoted to developing graphene-based terahertz photonic components including devices such as saturable absorbers that are often employed as materials for passive mode-locking [59, 60], terahertz filters [61, 62], broadband detectors [63, 64], and for THz generation [65]. A detailed understanding of the terahertz-graphene interaction is required to take full advantage of the material, and there have accordingly been many recent studies investigating the heating and cooling characteristics of graphene in the terahertz region [66–71], though many have been carried out us-

ing a transmission geometry exclusively. Taking into account the pump induced change in reflectivity can reveal new information; for example, the first clear experimental demonstration of carrier multiplication in graphene utilized both reflected and transmitted light [72]. Studies involving terahertz time-domain transmission spectroscopy enable one to extract the complex dynamic conductivity [73–77] but often employ photon energies of a few meV, and are therefore limited to probing intraband absorption only. In this work, we explore a regime of intermediate photon energies, where interband processes also contribute to the optical properties. Here we present a far-infrared pump-probe study that measures both the transmitted and reflected light that enables a comprehensive accounting of the radiation. The data from this experiment reveals the presence of a prominent nonlinear reflection, that saturable absorption is present at all fluences, and a transmission that changes sign with fluence. By employing a hot carrier model to determine the graphene optical properties, we show that it is possible, at sufficiently strong intensity, to switch from a primarily interband absorption dominated regime, to one exhibiting significant intraband processes. Together, the measurement and theory give a full picture of the interaction of intense terahertz radiation with low-doped multilayer graphene and provide insight for the design of photonic components that operate in this frequency range. This effect is general in nature and will persist at other wavelengths since it depends primarily on the chemical potential relative to the photon energy.

3.1.2.2 Measurements

In this work we investigate multilayer epitaxial graphene (MLEG) produced by thermal decomposition of the carbon terminated face of $(000\bar{1})$-oriented silicon carbide [78, 79]. This growth process yields individual layers that are rotated with respect to one another, thus producing multiple decoupled graphene layers [80]. The graphene properties were verified using angular resolved photoemission spectroscopy to ensure linear dispersion [81] while the thickness was measured using ellipsometry, which indicated that the sample consists of approximately 50 layers. Investigation using magneto-spectroscopic measurements reveal long momentum relaxation times that can be attributed to low defect densities (scattering time: $\tau_s = 300\,\mathrm{fs}$) [82] and extremely low doping for the majority of the layers (in the range of 8-15 meV) [51, 81, 82]. It should be noted that the layers near the SiC-graphene interface can have larger doping levels (≈ 300 meV) due to interfacial charge redistribution from the SiC substrate [78]. The doping levels decrease rapidly within the first few layers away from the substrate, leaving a mostly intrinsic graphene multilayer [51, 83, 84].

To carry out a pump-probe study in which both reflected and transmitted light are collected, an off-axis parabolic mirror (OAP) is used (cf. Fig. 3.4). This approach allows spatial separation of the pump and probe pulses in both the transmitted and reflected directions and produces a focused spot size of 500 µm. The beam path begins with high fluence pulses generated from a free-electron laser (FEL) [85] being directed through a beam splitter which separates the beam into pump and probe paths. The pulses from the FEL have a repetition rate of 13 MHz and a center wave-

length of 42 μm, corresponding to a photon energy of 30 meV or equivalently a center frequency of about 7 THz. The bandwidth of the FEL spectrum was measured with a grating spectrometer to be around 0.3 μm. As the pulses are nearly Fourier limited [85], the pulse width can be estimated to be around 7.5 ps. The pump and probe beam paths are independently attenuated and are linearly cross-polarized. Using cross-polarized pump and probe beams helps mitigate the detection of scattered pump radiation and also suppresses potential coherent artifacts when the pulses are overlapped in space and time. The pump was chopped using a mechanical chopper and a pump-to-probe power ratio of around 25 was maintained for all measurements reported in the study. As shown in Fig.3.4, the probe beam is delayed with respect to the pump pulse using a delay stage that allows for delays of up to 250 ps to be scanned.

Pump-probe measurements are carried out for a variety of pump fluences spanning over two orders in magnitude (25 nJ·cm^{-2} to 8.6 μJ·cm^{-2}) at a temperature of 10 K. The pump-induced modulation on the reflected and transmitted probe pulse is measured using lock-in detection, producing the values $\Delta\mathcal{T}$ and $\Delta\mathcal{R}$ respectively. The changes in transmission and reflection can be specified as a percentage by dividing $\Delta\mathcal{T}$ and $\Delta\mathcal{R}$ by the signal obtained by chopping the probe directly and measuring the transmitted and reflected signals when no pump is present. This gives, respectively, the relative change in transmission and reflection, $\Delta\mathcal{T}/\mathcal{T}$ and $\Delta\mathcal{R}/\mathcal{R}$. The pump-induced change in absorption is calculated from the transmission and reflection measurements using the relation $\Delta\mathcal{A} = -(\Delta\mathcal{T} + \Delta\mathcal{R})$. Since an accurate measurement of the absorbed probe is difficult, $\Delta\mathcal{A}$ cannot be easily

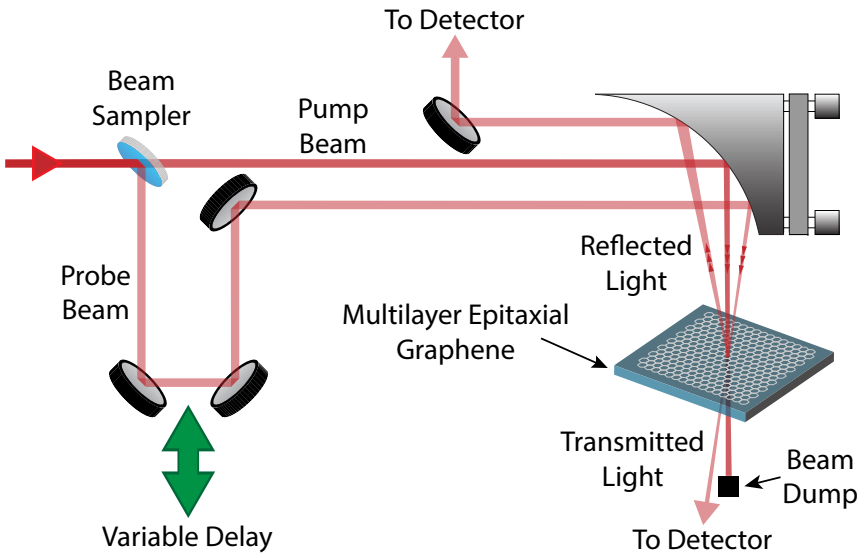

Figure 3.4: Diagram showing beam paths for pump and probe beams. The transmitted and reflected portions of the probe beam were measured as a function of the pump-probe delay.

normalized to a relative value, as was done for the transmitted and reflected signals, and is therefore given in arbitrary units.

Figure 3.5 shows the measured change in transmission, reflection, and absorption as a function of probe delay and pump fluence. In Fig.3.5(a) the relative change in transmission exhibits a fluence-dependent sign change apparent as red and blue regions in the colormap. At pump fluences below $0.6\,\mu\mathrm{J}\cdot\mathrm{cm}^{-2}$ the transmitted signal is positive, suggesting that saturable absorption is dominant in the terahertz transmission for low pump fluences. When the pump fluence increases beyond $3\,\mu\mathrm{J}\cdot\mathrm{cm}^{-2}$ the sign of the terahertz-induced transmission becomes predominantly negative; indicating that either a pump-induced absorption effect or reflection is responsible for the decrease in transmission. The relative change in reflection is displayed in Fig. 3.5(b) and exhibits a strictly positive signal that increases monotonically with pump fluence. The positive nature of this signal strongly indicates that the negative relative transmission at high pump fluences is at least partially caused by an increase in the graphene reflectivity. A similar monotonic trend is seen for the change in absorption, (cf. Fig. 3.5(c)) which is entirely negative, verifying that the graphene behaves as a saturable absorber over the entire range of pump fluences investigated. As a result of the strong pump-induced reflection, determination of the absorption saturation fluence using only the transmission data can lead to a significant underestimation of its actual value. In the present work, the absorption saturation fluence was estimated [86] from the positive portion of the transmission data to be $0.22\,\mu\mathrm{J}\cdot\mathrm{cm}^{-2}$, seven times smaller than the value determined by including both transmitted and reflected light in the estimation ($1.54\,\mu\mathrm{J}\cdot\mathrm{cm}^{-2}$). An accurate

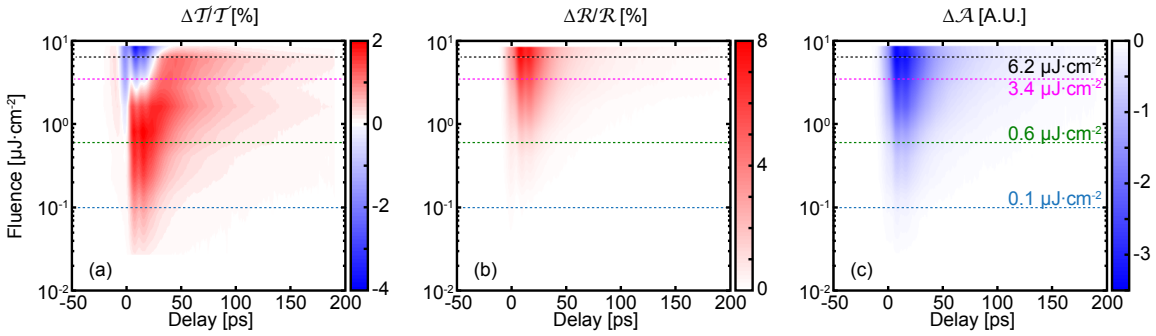

Figure 3.5: Measured (a) relative change in transmission, and (b) reflection as a function of pump fluence and pump-probe delay. Change in absorption (c) is calculated from the transmission and reflection data. The dashed lines indicate slices of the data at fluences that produce distinct curves in the relative transmission data.

accounting of the saturation fluence and the presence of a large, photoinduced reflection are important considerations for graphene-based saturable absorbers employed in laser mode-locking applications [87]. This also suggests the possibility of using graphene as a broadband optically controlled reflector, a device that would have an enhanced reflectivity with increasing pulse fluence.

3.1.2.3 Theory

To understand the transient changes in the optical properties, we first consider the temperature dependent conductivity of graphene. We assume that thermalized distribution is achieved in the material during the pump excitation which is well justified by noting that the carrier-carrier scattering processes through which the

electron population is heated is much faster ($\approx$ 100 fs [67]) than the pulse duration used in experiment. We can calculate the temperature dependent terahertz conductivity using [88]:

$$\sigma(\omega,T)=\frac{e^2(\hbar\omega)}{i\pi\hbar}\left(\int_{-\infty}^{+\infty}dE\frac{|E|}{(\hbar\omega)^2}\frac{\partial f(E,T)}{\partial E}-\int_0^{+\infty}dE\frac{f(-E,T)-f(E,T)}{(\hbar\omega)^2-4E^2}\right). \tag{3.5}$$

In the above expression E is the energy, e is the electron charge, ω is the frequency of the illumination, $\hbar$ is the reduced Planck's constant, and $f(E,T)=(\exp\left[(E-\mu(T))/k_BT\right]+1)^{-1}$ is the Fermi function, where $\mu(T)$ is the temperature-dependent chemical potential, k_B is the Boltzmann constant, and T is the electron temperature. The first and second terms in Eqn. (3.5) describe the intraband and interband conductivity respectively. The intraband portion can be evaluated to give: $\frac{2ie^2}{\pi\hbar}\frac{k_BT}{\hbar(\omega+i\tau_s^{-1})}\ln\left[2\cosh(\frac{\mu(T)}{2k_BT})\right]$, where τ_s is the electron scattering time, while the interband portion is evaluated numerically [88] (the result of this integration is complex due to the presence of a pole at $E=\hbar\omega/2$). The number of charge carriers is conserved in our calculations ($n=\int_{-\infty}^{+\infty}D(E)f(E)dE$ where $D(E)$ is the graphene density of states), and defines an implicit relationship between the chemical potential and temperature [88, 89]. In the following analysis, we attribute the optical response of the graphene to be entirely from the low-doped layers [67] which comprise the majority of our multilayer graphene sample. As a check, we calculated the pump-probe signals resulting from three highly doped layers of graphene on top of SiC (not shown). The pump-induced change of the optical parameters was more than two orders of magnitude smaller than those observed experimentally; verifying

that the large number of low-doped layers dominate the optical response.

The media surrounding the graphene impacts the optical properties expected from the combined superstrate-graphene-substrate interface [90]. The temperature dependent conductivity is calculated and then used to find the temperature dependent optical parameters ($\Delta\mathcal{T}/\mathcal{T}$, $\Delta\mathcal{R}/\mathcal{R}$, and $\Delta\mathcal{A}/\mathcal{A}$) for the well known case of a lossy film of thickness, d, separating two materials with permittivities ϵ_a and ϵ_b [91]. In this calculation we use a thickness corresponding to 50 graphene layers and a super-/substrate permittivity of 1 (vacuum)/12.3 (SiC). Charge impurities in the substrate material as well as surface topography and defects can further influence the properties of the graphene through the formation of spatial charge puddle inhomogeneities which modify the transport properties in low-doped graphene [92–95]. In the present work, the far-infrared beam samples a large area of the multilayer graphene containing a spatially inhomogeneous distribution of chemical potential patches (length scale for potential patches have been reported to be of order 100 nm [96]). The variation in the charge carrier density was measured experimentally on highly-doped, single-layer epitaxial graphene on the Si-face to be $5 \times 10^{11}\,\mathrm{cm}^{-2}$ [97] and considered theoretically using Gaussian statistics [92]. The beam averages over these patches and samples an effectively broadened Fermi distribution edge. Optical parameters best matching the experimental data are produced by convolving the Fermi distributions used in our calculations with a carrier density having a standard deviation (fluctuation strength) of approximately $4 \times 10^{10}\,\mathrm{cm}^{-2}$, indicating exceptionally high quality graphene layers..

Figure 3.6 shows the change in optical coefficients as a function of change in

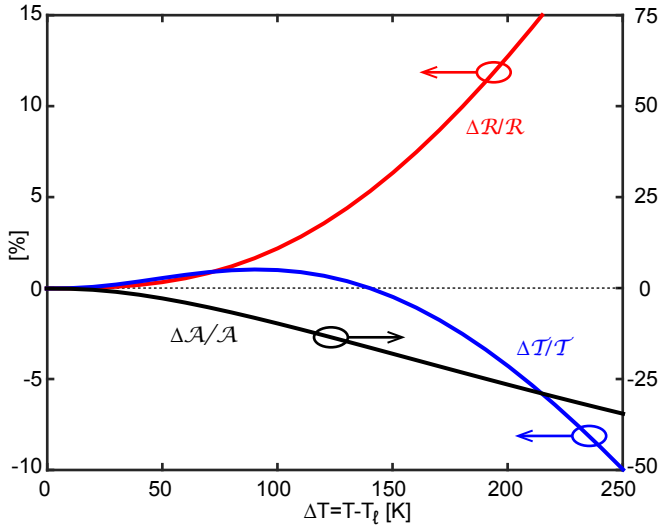

Figure 3.6: Calculated optical parameters for multilayer epitaxial graphene on silicon carbide substrate as a function of change in temperature. Parameters for calculation are for 50 graphene layers with $n = 1.65 \times 10^{10}$ cm^{-2}, $\tau_s = 300$ fs at a temperature of $T_\ell = 10$ K.

temperature at a lattice temperature of $T_\ell = 10\,K$. The reflection and absorption curves are seen to be entirely monotonically increasing and decreasing functions of change in temperature respectively, while the relative change in transmission changes sign, becoming negative for temperature changes higher than 140 K. The absorption and reflection curves illustrate that this behavior emerges when the influence of the pump-induced reflectivity surpasses that of the interband absorption bleaching. This bleaching appears as a negative change in the absorption in Fig. 3.6 and is the result of Pauli-blocking. This effect is dominant over the pump-induced reflection for small changes in temperature and leads to a net positive $\Delta\mathcal{T}/\mathcal{T}$. It will appear at other frequencies in the infrared where the doping and photon energy are of similar scale and changes in temperature from the absorbed radiation will sufficiently broaden the Fermi distribution.

Having established the role of the pump-induced reflection in the optical transmission in graphene, we next demonstrate that the derived temperature dependent optical parameters will lead directly to pump-probe signals with identical characteristics to those measured experimentally. An energy balance equation is used to form a relationship between the incident power and the pump-induced change in temperature in the graphene. For the sake of clarity, a model consisting of only the essential heating and cooling terms, similar to those used by others studying monolayer graphene [98–100], are used to describe the thermodynamics of the multilayer graphene in our pump-probe experiment. The resulting nonlinear differential equation contains terms for the electronic heat capacity, cooling, and a self-consistent

absorption/heating term:

$$\mathcal{C}_{el}(T)\frac{dT}{dt} = \mathcal{A}(T)\eta P(t) - g_1(T - T_l). \tag{3.6}$$

The terms in the energy balance equation are given as follows: $\mathcal{C}_{el}$ denotes the electronic specific heat capacity, where $\mathcal{C}_{el}(T) = \left(\frac{18\zeta(3)}{\pi\hbar^2 v_F^2}\right) T^2$ for our low-doped graphene [101–103] where v_F denotes the Fermi velocity and ζ is the Riemann zeta function. The term $\mathcal{A}(T)$ is the temperature dependent absorption as determined from our previous analysis of a lossy film separating two dielectrics. A phenomenological heating efficiency term [89], $\eta \approx 0.03$, was introduced into Eqn. (3.6) to achieve similar fluence scaling between the thermodynamic model and the data by scaling the incident power. The efficiency factor accounts for all of the unknown parameters in the energy balance equation with a single term. The incident laser pulse heating the graphene is described by a Gaussian envelope, $P(t)$. The parameter $g_1 = T^4 \frac{7\pi^3 k_B^5 D^2}{30\rho\hbar^5 v_F^6}$ is the cooling power coefficient in the clean limit when the temperature is above the Bloch-Gruneisen temperature [100] (T_{BG} <10 K for the low-doped layers), $D \approx 2\,\text{eV}$ is the deformation potential, $v_s = 2 \times 10^4$ m/s is the sound velocity in graphene, and $\rho = 7.6 \times 10^{-7}$ kg/m^2 is the mass density of graphene. Equation 3.6 is solved self-consistently to give the change in temperature as a function of time and used to calculate the delay-dependent optical parameters in the weak probe limit (i.e., the temperature change results solely from the pump pulse). The left panel of Fig. 3.7 shows the optical parameters produced by the measurement at selected pump fluences defined in Fig. 3.4 while the right panel of Fig. 3.7 shows the corresponding curves determined by the model.

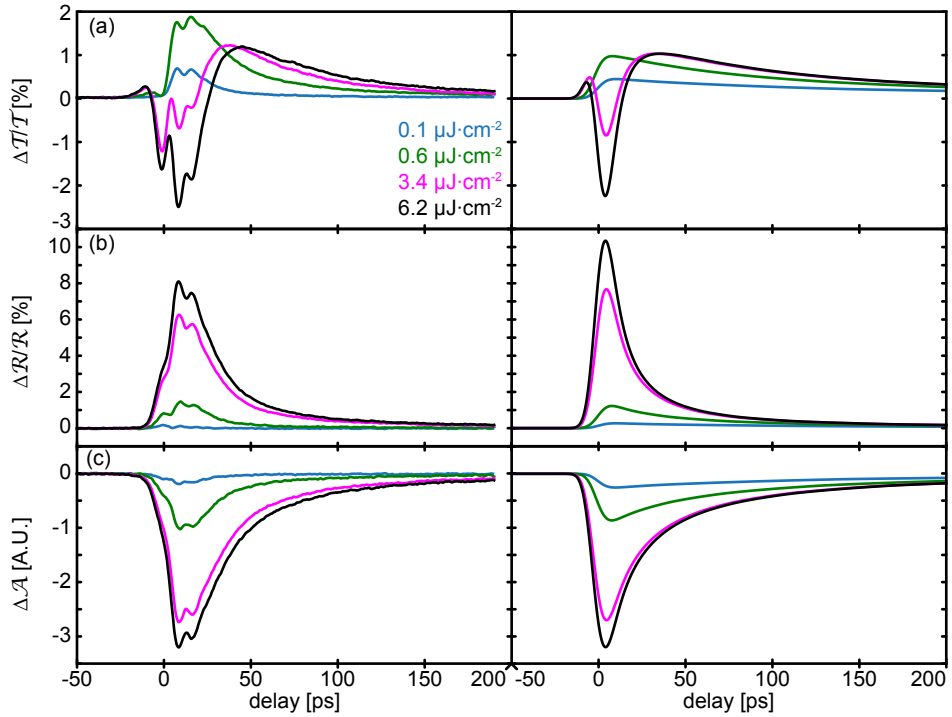

Figure 3.7: Measured (left panel) and modeled (right panel) transient pump-probe curves for the four pump fluences defined in Fig. 3.5.

3.1.2.4 Discussion

As can be seen from Fig. 3.7(a), the model and data show relative transmission curves that are strictly positive at low fluence ($< 0.6\mu J \cdot cm^{-2}$) and mostly negative at higher fluences ($> 3\mu J \cdot cm^{-2}$). The relative change in reflection from the model and data are presented in Fig. 3.7(b). These curves display a relative reflection that rapidly increases with pump fluence. The change in absorption curves decrease with pump fluence as seen in Fig. 3.7(c). The transmission curves change sign as a function of fluence when the increasing reflection becomes larger than the steadily decreasing absorption; marking a change from a fluence regime exhibiting primarily saturable absorption, to one exhibiting primarly pump-induced reflection. This changeover in phenomenology takes place when heating reduces the amount of interband absorption due to a decreased difference in carrier occupation at $\pm\hbar\omega/2$ and a simultaneous increase in intraband conductivity. The latter scales with temperature and produces a change in reflectivity. Figure A.1(a) plots the Fermi function for a range of temperature changes and shows the degree of the temperature dependent change in chemical potential and edge broadening with respect to the incident photon energy. The effect of disorder can be observed as a broadened width of the Fermi function at low temperatures.

The real part of the graphene conductivity as determined by Eqn. (3.5) is plotted in Fig. A.1 (b). Here the conductivity resulting from interband and intraband processes are plotted independently (dash-dotted and dashed lines respectively) and together add up to the total conductivity (solid trace). As shown in the figure, the

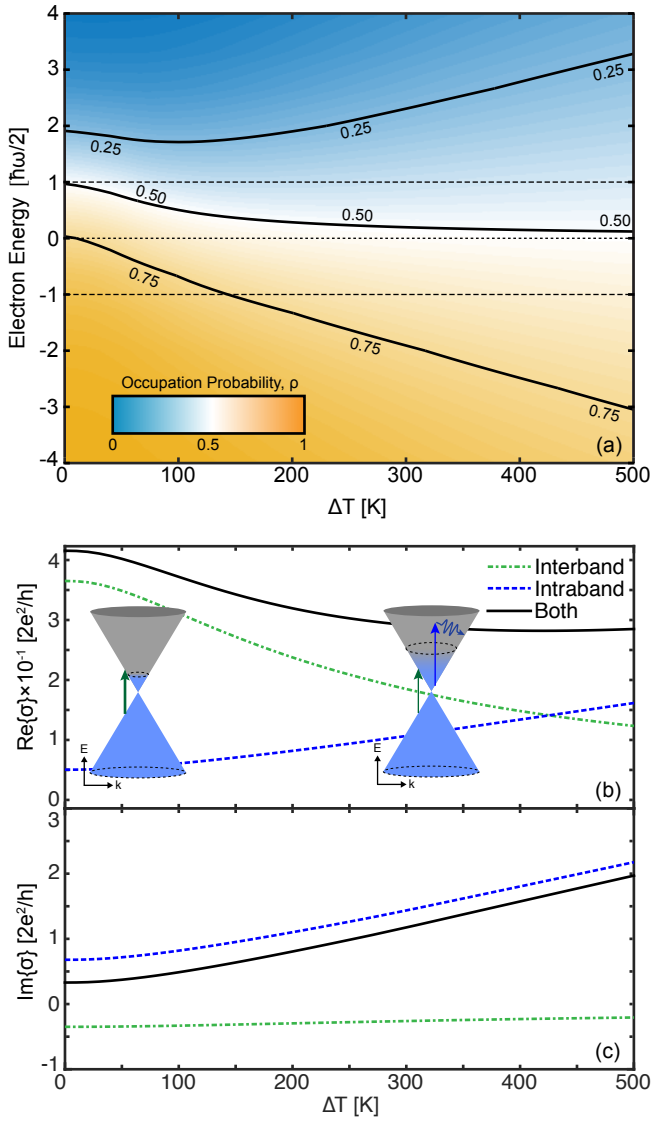

Figure 3.8: (a) Contour plot of the occupation probability for different changes in temperature. The ordinate axis is scaled by the photon half energy ($\hbar\omega/2 = 15\,\text{meV}$); horizontal dashed lines at -1, 0, and 1 are plotted for visual reference. Real (b) and imaginary (c) parts of the conductivity showing showing inter- and intraband contributions versus change in temperature ($T_\ell = 10\,\text{K}$) for the photon energy used in the experiment ($\hbar\omega = 30\,\text{meV}$). The schematic diagrams of the Dirac cones in part (b) depict the inter- and intraband absorption processes.

heating modifies the conductivity of the graphene and results in inter- and intraband processes playing a diminished and increased role respectively (an estimated peak change in temperature of around 200 K was reached in our experiments). Interband and intraband absorption processes are depicted schematically in Fig. A.1(b). At low temperature, interband absorption (green arrow) is the dominant process, while with increasing temperature intraband absorption, which is a phonon assisted process, becomes dominant (blue arrow). The imaginary part of the conductivity that leads to the increase of the reflection is shown in Fig. A.1(c). Since absorption in the graphene is proportional to the real part of the conductivity, the decrease shown in Fig. A.1(b) confirms that the graphene behaves as a saturable absorber for all fluences in our experiment and that the sign change in the transmitted signal results exclusively from an increase in the reflectivity.

The observed sign change in transmission was previously shown to originate from a temperature dependent change in inter- and intraband conductivity. To generalize this result, we consider the temperature at which the real component of the conductivity from interband and intraband processes are equal for a range of photon energies and carrier concentrations (plotted in Fig. 3.9 as solid colored lines). Though the temperature at which the conductivity contributions from interband and intraband processes achieve parity was not reached in our experiment, this temperature identifies a general point of comparison for the optical properties studied in this work. Analogous energy scales to the ones used in our experiment are represented for the case where the incident photon energy is in the vicinity of the chemical potential (shown as dashed colored lines in Fig. 3.9) where, with increas-

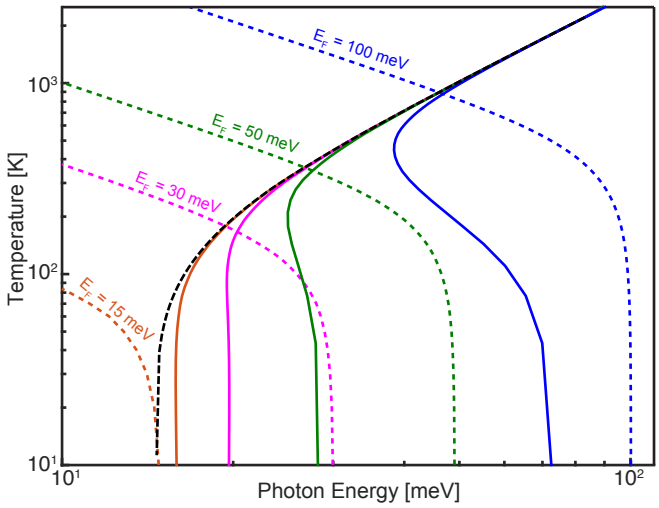

Figure 3.9: Plot of temperature where the real part of the conductivity has equal contributions from intra- and interband processes as a function of photon energy for various sample doping levels (solid colored lines) and a variation in the Fermi level of approximately 20 meV (corresponding to a carrier density variation of $4 \times 10^{10}\,\mathrm{cm}^{-2}$ for $E_F = 15\,\mathrm{meV}$). The dashed colored lines show the corresponding temperature dependent chemical potential while the black dashed line indicates a numeric high temperature solution that is independent of doping level.

ing temperature, the conductivity transitions from being interband to intraband dominant as in Fig. 5(b). For photon energies well below the chemical potential, the crossover temperature represents the crossover from intraband to interband processes. Above the chemical potential, all curves asymptotically approach the high temperature limit ($k_B T \gg \mu(T)$, black dashed line) which is independent of the graphene doping. In the high temperature limit, the crossover temperature increases with photon energy which means that at higher photon energies, the electrons must be heated by a greater amount in order for the intraband processes to compete with the interband ones. At low temperature and doping, the disorder-broadened Fermi function limits the solution to finite valued photon energies. The conductivity crossover temperatures in Fig. 3.9 are well within the range of experimentally observed values [67, 76, 89] and indicate that the same phenomena can be expected for a range of wavelengths spanning the mid- and far-infrared frequency range.

3.1.2.5 Conclusion

We have investigated the terahertz response of low-doped multilayer epitaxial graphene using pump-probe spectroscopy that measures both the reflected and transmitted far-infrared radiation. This radiometrically comprehensive measurement allows for clear determination of the differential absorption in the material which was shown to be negative, and monotonic with fluence; verifying that the graphene behaves as a saturable absorber. Additionally, the relative change in the terahertz transmission was observed to change sign depending on the magnitude of

the pump fluence as the result of a large, photoinduced reflection. This effect was clearly explained by a hot carrier model that identified two distinct physical mechanisms for the terahertz optical properties: one at low fluence where the properties are dominated by interband absorption of the incident terahertz photons, and a metallic regime that is characterized by increased intraband processes resulting from a heated electron system with significant carrier populations above the incident photon energy. These results demonstrate that it is possible to observe a self-induced modification of the absorption mechanism and underscores the importance of accounting for reflection in graphene optics. These findings apply to a range of mid- and far-infrared frequencies and will be important for the design of next generation graphene-based terahertz devices.

3.1.3 Temporal Response of a Graphene Photodetector

The temporal response of a graphene photodetector based on the photothermoelectric effect is presented in this section. Pump-probe measurements were previously described that probed the interaction of terahertz radiation with graphene. In this section we describe how other time-domain techniques can be used to study a graphene-based photodetector. Temporal characterization of the photovoltage produced by an electrically connected device can provide information about the detection mechanism, while also giving practical information about the operating bandwidth. Two methods for characterization of a connected device are described in this section. The detector described here is described fully in the work of Cai. X,

et al. [46] and was characterized in collaboration with the author of that study.

The graphene photodetector is formed by creating a graphene channel between two dissimilar metal electrodes whose separation is shorter than the electron cooling length in graphene (the cooling length is given by $\xi = \sqrt{\kappa/\gamma C_{el}}$, where κ is the thermal conductivity, C_{el} is the electron specific heat, and γ is the electron-lattice cooling rate, [104]). Two different metal contacts on the opposite sides of the device are used to create an asymmetric Fermi level across the graphene channel, which modifies the Seebeck (thermo-power) coefficient. When heated by incident light, electrons in the graphene will diffuse according the electron temperature gradient and a net voltage signal will be generated due to the asymmetry of the Seebeck coefficient across the channel. This mechanism generates a measurable photo-voltage across the electrodes that is sensitive to a wide range of wavelengths and is fast in its response (the response time is limited by the diffusion of hot electrons to the cooler electrodes). Full details describing the theory of operation are given in reference [46].

The temporal characterization was carried out on two monolayer graphene-based devices utilizing the photothermo-electric effect based on the dissimilar metal electrode design. The first device was fabricated by depositing mechanically exfoliated graphene on a partially conductive (100-250 Ω·cm) silicon substrate with an electronically insulating 300 nm SiO_2 top layer. Dissimilar metal electrodes were patterned and deposited using electron-beam lithography and thermal evaporation to produce 20 nm thick chromium and gold contacts. A back gate was formed by electrical connection to the partially conducting substrate which allows for tuning of the carrier doping in the 3μm×4μm graphene monolayer. An optical micrograph

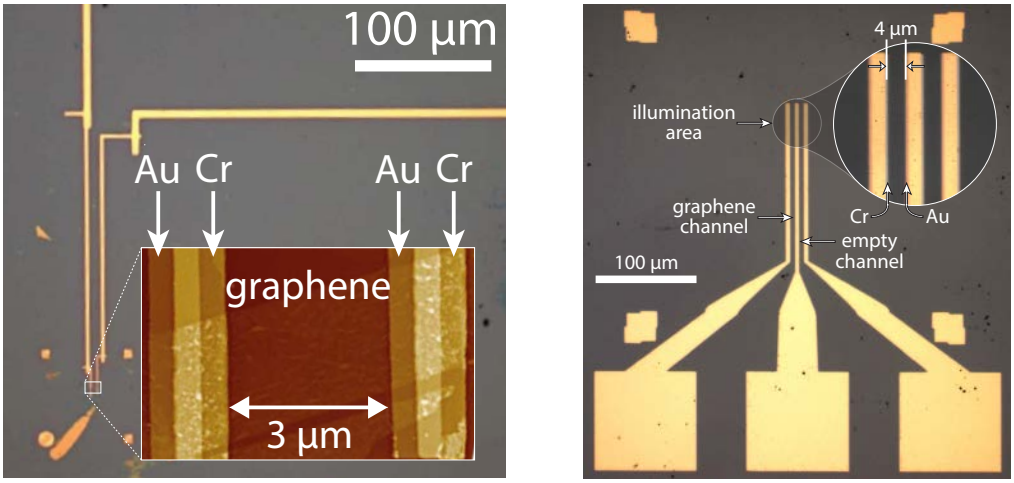

Figure 3.10: (a) Optical micrograph of a graphene photodetector fabricated on a Si/SiO_2 substrate used for the intrinsic response measurement (section 3.1.3.1). The inset shows and atomic force micrograph of the exfoliated graphene channel. (b) Optical micrograph of a high speed graphene photodetector utilizing a co-planar waveguide geometry used for the optical extrinsic response measurement (section 3.1.3.2). The photodetector employs epitaxially grown graphene on a SiC substrate.

of the device is shown in Fig. 3.10(a); the inset shows an atomic force micrograph of the active area of the detector.

The second device is fabricated from epitaxially grown monolayer graphene on a semi-insulating (109 Ω·cm) 6H-SiC(0001) substrate [105]. A high-speed co-planar waveguide geometry was defined, and the graphene selectively patterned forming a 4 µm×100µm graphene channel, by electron-beam lithography. Dissimilar chromium

and gold electrodes were deposited by lift-off. Back gating was not attempted as to avoid increasing the stray parasitic capacitance, which could impact the high-speed operation of the device. An optical micrograph of the high-speed graphene on SiC device is shown in Fig. 3.10(b). Full details on the fabrication procedure for each device is given in [46].

3.1.3.1 Intrinsic Response of a Graphene Photodetector

Intrinsic device speed refers to the timescale in which hot, photo-excited carriers diffuse to the electrodes and does not include circuit externalities such as electrode capacitance. The intrinsic response time is measured using a pulse-coincidence method that measures the photo-voltage produced by the device as a function of delay between two 60 fs, near IR (1560 nm) pulses. The change in the photo-voltage near zero delay, when the pulses are coincident, indicates the nonlinear nature of the heating when the electrons do not fully reach thermal equilibrium prior to the arrival of the second pulse. The pulse-coincidence measurement reveals a 10-15 ps intrinsic timescale that remained constant over the measured temperature range of 15K to 150K. The 10-15 ps intrinsic thermal response is comparable to other measurements reported in the literature [106] for similar graphene-based detectors in the near IR. Figure 3.11 shows the pulse-coincidence photo-voltage as a function of delay for a range of temperatures spanning one order in magnitude.

The flat response time with temperature suggests that the hot electrons in the graphene two-dimensional electron gas cool at a rate independent of tempera-

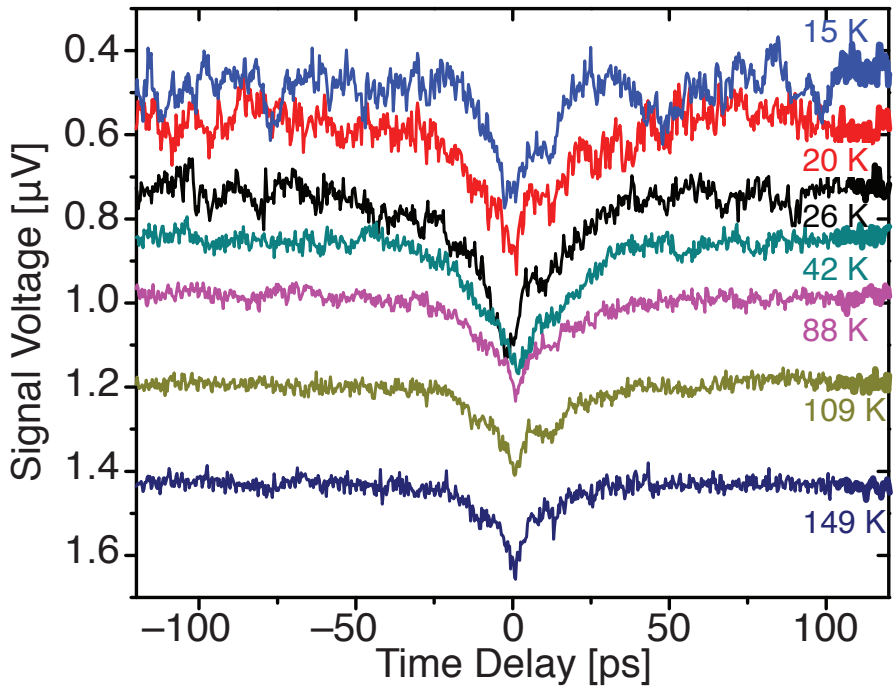

Figure 3.11: Photoresponse from pulse coincidence laser pulses as a function of delay time for a range of temperatures.

ture. A simplified heating equation dominated by diffusive cooling predicts a cooling rate that is independent of temperature, with the cooling time given as the ratio $\tau = C/\kappa$, where C and κ are the heat capacity and thermal conductivity of the graphene (the only two physical parameters in the model). This approach yields a time constant that is independent of temperature since both the heat capacity and thermal conductivity are proportional to temperature. When illuminated, the graphene electrons are heated and therefore the heat capacity of the graphene is determined by the electronic heat capacity which is given by $C = \Lambda e^2 \nu(E_F) AT$ [107] (here Λ is the Lorenz number, e is the fundamental electric charge, $\nu(E_F)$ is the den-

sity of states for a given Fermi energy, and A is the area of the graphene channel). The thermal conductivity is determined via the Weidemann-Franz law as $\kappa = \Lambda\sigma T$, where σ is the conductivity of the graphene. Estimates of the time constant using these equations (each of which assumes a purely electronic heat capacity and heat conduction pathway) gives a time constant in the range of 10 - 100 ps that is consistent with the experimentally measured values extracted from the data in Fig. 3.11.

3.1.3.2 Extrinsic Response of Graphene Photodetector

Though the highest operating frequency of the detector is in principal determined by the intrinsic speed of the device, practically speaking, the speed at which signal can be read out of the detector ultimately determines the bandwidth of operation. The extrinsic measurement includes all circuit parasitics and provides a demonstrable proof of the photo-thermoelectric graphene detector concept. Two extrinsic response measurements were carried out, one at visible wavelengths and another at terahertz frequencies (0-2 THz)[1]. All impulse response measurements were done at room temperature (300 K).

The optical extrinsic response measurement was carried out using short pulses and a fast sampling oscilloscope setup. In this approach a pulsed 1 kHz laser with 50 fs pulses, 800 nm wavelength, and an average beam power of 0.25 mW was di-

[1]The THz impulse response measurement was carried out on a third, large are device of similar making to those described previously. The large area was required to intercept as much of the large are THz beam as possible.

rected onto the graphene detector utilizing a co-planar waveguide geometry shown in Fig. 3.10(b). A small amount of the beam incident on the graphene photodetector was picked off and detected by a commercially available fast (125 MHz) visible wavelength photodetector (Newport 1801) which served as a trigger signal for a 40 GHz sampling oscilloscope (Agilent 86100C). The transient photo-voltage was read out by a fast ground-signal-ground microwave probe and recorded by the sampling oscilloscope. A plot of the transient photo-voltage is shown in Fig. 3.12(a). The full width half maximum (FWHM) of the signal is 30 ps, which is nearly the impulse response of sampling oscilloscope. This suggests the graphene photodetector is faster than the measured response of 30 ps (i.e., the measurement is a lower bound of the response time) since the voltage transient is given by the convolution of the photodetection circuit and the response of the oscilloscope.

The extrinsic photoresponse was also carried out at THz frequencies. Broadband terahertz pulses with a duration of ∼1 ps and a spectrum spanning 0-2 THz were produced through optical rectification of femtosecond pulses in a lithium niobate prism [108], and focused onto the device through a polymethylpentene (TPX) lens. The focused terahertz pulses had a beam diameter of ∼1 mm and a pulse energy of 160 nJ at a repetition rate of 1 kHz. In order to intercept a large amount of the THz radiation, a large-area device that connects several single-element graphene channels in series was used (shown inset in Fig. 3.12(b)). Each of these single-elements (gold contact-graphene channel-chromium contact) is identical in principal to the single-elements shown in the insets of Fig. 3.10. This device was fabricated using CVD graphene on SiO_2/Si and using a similar lithographic process as

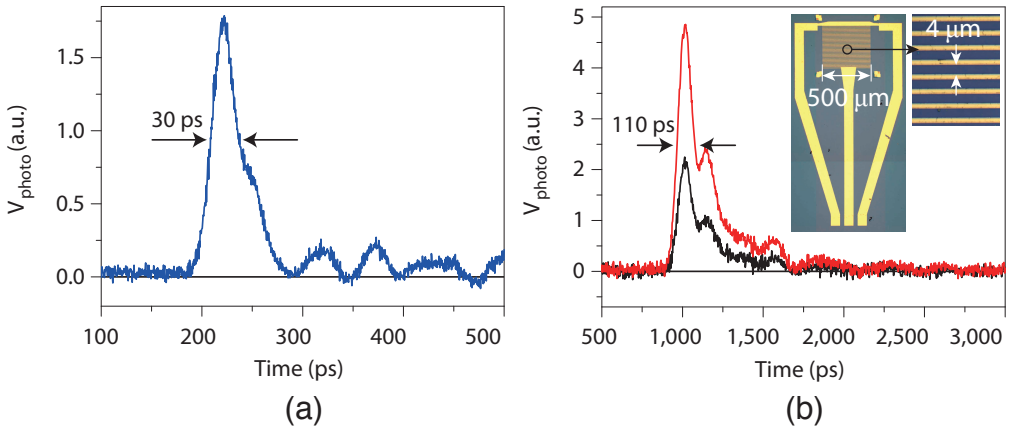

Figure 3.12: (a) Transient photo-voltage from optical impulse response measurement (FWHM 30 ps). (b) Transient photo-voltage from THz impulse response measurement at two different gate voltages (FWHM 110 ps). The inset shows the large area detector used for the THz measurement. The device is the same as previously measured devices, but uses a series connection of gold electrode-graphene channel-chromium electrode elements to increase the detector area.

described in section 3.1.3. Full details of fabrication can be found in [46]. The measured extrinsic time response of the large area detector was 110 ps FWHM. The response was measured at several different gate voltages (two shown in Fig. 3.12) to verify the photo-voltage was originating from the graphene. We note that the THz time response of the large area device is longer than the optical extrinsic response measurement carried out on the single-element device (shown in Fig. 3.10(b)) and attribute this difference to the higher capacitance present in the large area device.

Chapter 4: Investigations on Atomically Thin Black Phosphorus

4.1 Overview

Black phosphorous is an electrically conductive, stable allotrope of phosphorous formed by heating white phosphorous under high pressure [109]. It is a van der Waals solid (like graphite) in that two dimensions of the material are strongly (covalently or ionically) bonded, while the third dimension is held together by weaker van der Waals forces [110]. This property lends itself to a mechanical exfoliation process (whereby few or single atomic layers can be isolated [111]) and has thus become one of the latest two-dimensional materials to be studied by researchers [112].

Unlike graphene, the electrical band structure of black phosphorus possesses a band gap. This feature, along with high electrical mobility, electrical and optical anisotropy, and field effect creates the possibility to explore interesting physics as well as novel optoelectronic devices. This chapter explores the nonlinear optical properties of atomically thin black phosphorus flakes (section 4.3) and also presents the demonstration of a fast mid-infrared photoconductive detector utilizing a black phosphorus field effect transistor architecture (section 4.4). The study of the optical nonlinearity and its associated time scale aims to explore new material properties as well as gauge the suitability of multilayer phosphorene as a material for opto-

electronic applications. The photodetector work details the first demonstration of a photoconductive detector operating in the mid-infrared, close to the longest wavelengths where the photoconductive effect is possible. A brief overview of the material properties of black phosphorus and a summary of devices based on this material is given in section 4.2.

4.2 Black Phosphorus

The crystal structure of black phosphorus is orthorhombic and forms a puckered hexagonal lattice as shown in Fig. 4.1(b) and (c). The corrugated structure of the crystal produces unique anisotropic optical and electrical properties [113] with recent experimental studies showing anisotropic linear optical absorption and electrical transport [112]. One of the most important qualities of multilayer phosphorene is the direct bandgap, a feature lacking in graphene. The bandgap in black phosphorous ranges from 300 meV (bulk) to 1.5 eV (single layer) and ranges in-between these values for the first few layers ($\sim$ 5 layers). Recent work also shows that the bandgap in the material can be further configured by inducing strain in the material [114]. Moreover, the relatively low bandgap of "bulk" black phosphorus (more than five layers) uniquely positions this material between graphene (zero bandgap) and the transition metal dicalcogenides (TMD, e.g., MoS_2) which are insulating materials with large bandgaps of a few electron volts [113]. Theoretical predictions estimate exceptionally high carrier mobilities of 10,000 to 26,000 $cm^2V^{-1}s^{-1}$ are possible [115] with recent experimental work reporting realized values in the range of 650 to 1000

$cm^2V^{-1}s^{-1}$ [112]. The ability to control the bandgap, the anisotropic optical and electrical properties, and the high mobility are all characteristics of significant technological importance for creating novel optoelectronic devices.

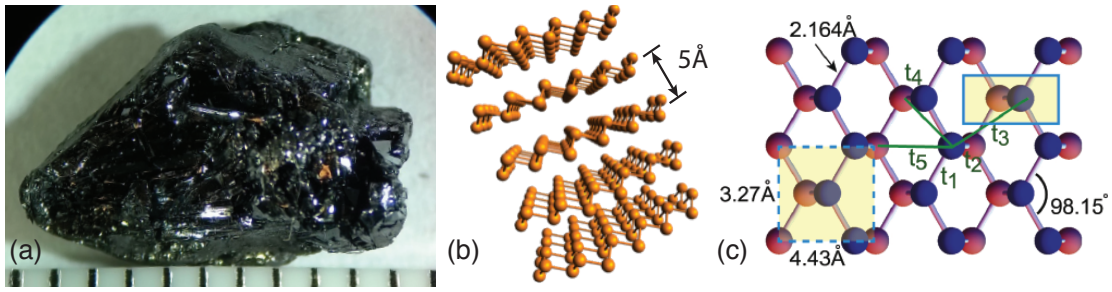

Figure 4.1: (a) Macroscopic picture of black phosphorus crystals, scale markers are 1 mm. Perspective (b) and top-down (c) view of black phosphorus chemical structure. Interlayer spacing is approximately 5 Å((b) and (c) adapted from [116]).

The favorable electrical and optical properties of black phosphorus has led to a large amount of research in using this material in field effect transistors and detectors. Recently chip-integrated detectors [117], field effect transistors [118], and saturable absorbers [119] have been recently realized in this material (though demonstrations have mostly been at visible and telecommunications wavelengths). Due to the size of its bandgap, which corresponds to the near- and mid-infrared frequency range, black phosphorus is highly attractive material for developing infrared optoelectronic devices.

4.3 Time-Domain Spectroscopy Black Phosphorus

4.3.1 Overview

In this section we present polarization-resolved transient transmission measurements on multi-layer black phosphorus. Background free two-color pump-probe spectroscopy measurements are carried out on mechanically exfoliated black phosphorus flakes that have been transferred to a large-bandgap, silicon carbide substrate. The blue-shifted pump pulse (780 nm) induces an increased transmission of the probe pulse (1560 nm) over a time scale commensurate with the measurement resolution (hundreds of fs). After the initial pump-induced transparency, the sign of the transient flips and a slower enhanced absorption is observed. This extended absorption is characterized by two relaxation time scales of 180 ps and 1.3 ns. The saturation peak is attributed to Pauli blocking while the extended absorption is ascribed to a Drude response of the pump-induced carriers. The anisotropic carrier mobility in the black phosphorus leads to different weights of the Drude absorption, depending on the probe polarization, which is readily observed in the amplitude of the pump-probe signals.

4.3.2 Introduction

Black phosphorus is a relatively new member in the family of two-dimensional materials that can be mechanically exfoliated to atomically thin films. Its crystalline structure forms a corrugated hexagonal lattice that exhibits unique anisotropic

optical and electrical properties [115] that have recently been experimentally observed [120]. The direct bandgap in black phosphorus is dependent on the number of layers, ranging from about 0.3 eV in bulk (5 or more layers) [121] to about 2 eV for a single layer [122]. In contrast to other two-dimensional materials, where the mobility is commonly far below that of graphene [123–125], the mobility in black phosphorus can approach values on the order of $10,000\,\mathrm{cm^2V^{-1}s^{-1}}$ [115]. The presence of a direct band gap along with the high carrier mobility makes black phosphorus an interesting candidate for fast field effect transistors [126] and optoelectronic devices like photodetectors [127, 128]. Similar to graphene, black phosphorus also features a strong saturable absorption [129], a feature that has already been exploited for use in mode-locked lasers [119]. Polarization-resolved linear spectroscopy measurements have shown that the optical absorption is strongly anisotropic [130], while photoluminescence measurements reveal an even stronger anisotropy, with the photoemission being strongly polarized (97%) in the direction perpendicular to the corrugations in the material [131]. Apart from linear absorption and electrical transport studies, the carrier dynamics in black phosphorus have not been thoroughly investigated. Two very recent studies report pump-probe measurements on black phosphorus flakes on a silicon substrate using a reflection geometry [132,133]. In this paper we present a polarization-resolved, collinear near-infrared pump-probe study on black phosphorus flakes in transmission. To achieve a background free transmission measurement, a semi-insulating, large bandgap silicon carbide substrate is used.

4.3.3 Measurements and Discussion

The two-color pump-probe experiments were carried out on multi-layer black phosphorus flakes obtained by mechanical exfoliation and transferral onto a 300 μm thick silicon carbide substrate. This substrate was chosen since it possesses a bandgap nearly two (four) times that of the pump (probe) photon energy; thus allowing for a pump-probe signal from the black phosphorus flake that is unaffected by contributions from the substrate. This property of the substrate was confirmed by pump-probe measurements on the bare silicon carbide where no signals could be observed. The exfoliation process yielded flakes between $30 - 80$ layers and several hundreds of μm^2 in area, as determined by optical contrast microscopy [134]. The results reported here are for a flake with 10 % linear transmission and an estimated thickness of approximately 80 layers. As a means of carrying out precision photometry, we patterned a circular chromium aperture that covers all but a 10 μm diameter region in the center of the black phosphorus flake under investigation. This ensures uniform illumination of the irregular black phosphorus flakes and guarantees that only probe light transmitted through the black phosphorus is measured by the detector. The aperture was patterned using electron-beam lithography and liftoff. Following fabrication, a 200 nm PMMA cover layer was spin-coated over the entire device to prevent degradation of the black phosphorus which is known to react with ambient humidity [134].

The measurements were carried out at room temperature (300 K) using two fiber lasers (Menlo Systems). The lasers produce approximately 100 fs wide pulses

at a repetition rate of 100 MHz and center wavelengths of 780 nm and 1560 nm for the pump and probe, respectively. The two lasers were electronically synchronized with a small difference in repetition rate, allowing for large pump-probe delays (up to 10 ns) to be achieved without the use of a mechanical delay line. Both the pump and probe separately pass through a half-wave plate to allow the polarization of each beam to be independently controlled. Figure 4.2(a) defines the polarization (shown as double-ended arrows) with respect to the major and minor axis of the measured relative linear transmission ellipse at 1560 nm for the particular black phosphorus flake presented in this work. The difference in transmission is caused by the anisotropy of the band structure [135, 136] and provides a means to establish the flake orientation prior to carrying out the polarization-resolved pump-probe measurements. In Fig. 4.2(a), the major axis (along the 0° direction) corresponds to horizontal polarization while the minor axis (along the 90° direction) corresponds to vertical polarization. Diagonal polarization refers to a linear polarization angle of 45° and 135°. The inset in Fig. 4.2(a) shows the linear polarization angle with respect to the corrugation orientation in black phosphorus. The main experimental diagram in Fig. 4.2(b) defines the independent linear polarization angles for both the pump and probe pulses as Φ_P and Φ_p, respectively. The pump is chopped (550 Hz) and combined with the probe beam before being reflected into an aspheric objective (NA=0.4) using a beam splitter. The light passing through the lens focusses the beams onto the sample, which is positioned such that the pump and probe beams overfill the aperture. The light transmitted through the aperture is recollimated by a second objective, passed through an intrinsic silicon window to filter out the pump,

and directed into the signal input of a balanced detector unit. The remaining light transmitted through the beam splitter passes through a variable optical attenuator, intrinsic silicon window, and into the reference input of the balanced detector. A lock-in amplifier monitors the pump-induced modulation of the probe in the black phosphorus flake as the delay between the pump and probe is scanned. For all measurements the probe fluence was approximately three orders of magnitude smaller than that of the pump. Figure 4.2(b) shows a diagram of the sample illumination geometry, an energy band diagram for the experiment, and an optical micrograph of a black phosphorus-filled aperture.

To investigate the power dependence of the pump induced changes, transient transmission data were collected for pump fluences ranging from $3\,\mu J/cm^2$ to $80\,\mu J/cm^2$ for vertically polarized pump and probe. The first 60 ps of the pump-probe signals are shown in Fig. 4.3(a). The pump-probe traces are characterized by an initial pump-induced transparency having a duration on the same time scale as the pump and probe pulse overlap, followed by a slower transient absorption. In the inset of Fig. 4.3(a) the $\Delta T/T_0$ values from the main panel of Fig. 4.3(a) are plotted for fixed delay values $\Delta t = 0$ ps and 10 ps as a function of pump fluence. The transmission spectra for these two phenomenologically distinct regions of the transient response (i.e., the absorption saturation region near $\Delta t = 0$ ps, and the reduced transmission region for $\Delta t > 5$ ps) scale linearly over nearly two orders of magnitude in pump fluence. This result is consistent with an absorption effect that is proportional to a population of free-carriers whose size is proportional to the absorbed power. Contemporaneous measurements on black phosphorus using

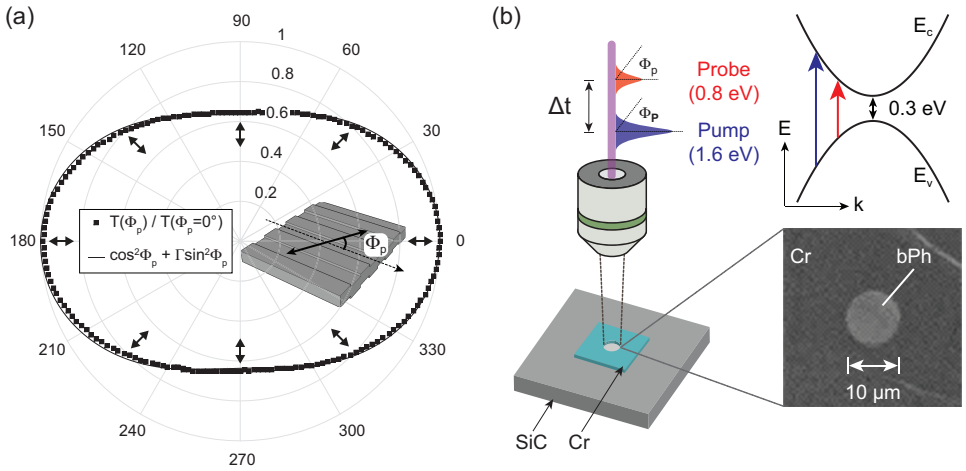

Figure 4.2: (a) Relative change in linear transmission as a function of the linear polarization angle with phenomenological fit. The double-ended arrows show the direction of the electric field oscillation and define horizontal, diagonal, and vertical polarizations. The inset shows the polarization angle with respect to the corrugated surface of the black phosphorus. (b) In clockwise order: Diagram showing the sample illumination geometry and definition of the pump-probe delay, simplified band diagram of bulk black phosphorus showing the relevant energy scales in the experiment, and an optical micrograph of a black phosphorus(bPh)-filled aperture.

reflection spectroscopy also observed linear power scaling and similarly attributed this effect to absorption by photoexcited carriers [132, 133]. To induce a change in transmission of order 10^{-3} in our experiment we estimate a photoexcited carrier density of $1.7 \times 10^{14}\,\mathrm{cm}^{-2}$. To evaluate the relaxation dynamics, Fig. 4.3(b) plots

the carrier-induced transient absorption on a logarithmic scale over a 5 nanosecond timescale, along with a bi-exponential fit to the data. For the lowest pump fluence (grey data set in Fig. 4.3), the relaxation can be described by a single exponential decay with a time constant of 770 ps. With increasing pump-power, a faster time constant of 180 ps (±30 ps) becomes more prominent (visible as an increasingly large upward curvature of the data at smaller delays as the fluence is increased), while the slower time constant linearly increases to 1.8 ns at 80 $\mu J/cm^2$ (appearing as a decrease in the slope of the data as the fluence is increased). We attribute the transient pump-induced transparency to Pauli blocking, while the subsequent slower negative transient reflects the lifetime of the pump-generated free carrier population. Absorbed pump photons create free-carriers in the black phosphorus that will increase the conductivity and lead to both an increased absorption and reflection [130]. We note that both effects could contribute to the observed negative transient seen here. Transient heating of the crystal lattice could also partially contribute to the observed negative signal. An increase in the lattice temperature could also explain the slowing of the carrier relaxation observed at higher pump fluences for delays above 1000 ps.

To further investigate the carrier dynamics, we performed a set of pump-probe measurements for different combinations of pump and probe polarization. The pump and probe polarizations were set to the four polarization angles of 0°, 45°, 90°, and 135° (corresponding to horizontal, diagonal, vertical, and diagonal polarization). The measurements for pump and probe polarization angles of 135° were performed as a crosscheck and yielded identical results to the measurements carried out at 45°.

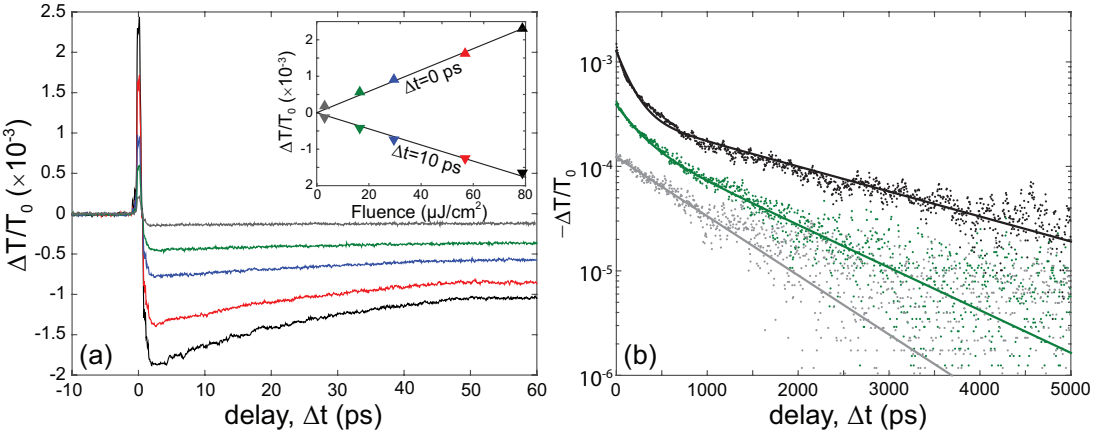

Figure 4.3: (a) Change in transmission as a function of probe delay for a variety of pump powers. The inset shows the linearity of the change in transmission with pump fluence at 0 ps and 10 ps. (b) Logarithmic plot of $\Delta T/T_0$ for three pump fluences along with bi-exponential fits (solid lines).

Figure 4.4 presents the pump-probe transmission spectra for 9 unique polarization configurations. Each panel of Fig. 4.4 contains the traces taken at different probe polarizations for a fixed pump polarization. All measurements were taken at a constant incident pump fluence of 30 μJ/cm^2. By comparing Fig. 4.4(a) and Fig. 4.4(c), one sees that in all cases the transient response is smaller when the pump is vertically polarized than when it is horizontally polarized. This dependence on pump polarization cannot be fully explained by polarization-dependent absorption of the pump, estimated to be only about 5% for the multilayer black phosphorus considered here. Assuming that the positive peak is caused primarily by Pauli blocking, this

suggests that the carriers are changing the orientation of their momentum, aligning along the energy gradient of the anisotropic band structure. The short time scale on which this transient enhancement of transmission occurs (within the resolution of the measurement) implies an efficient carrier-phonon scattering by which the carriers minimize their energy within the conduction and valence band, respectively.

We attribute the extended negative transient to intraband (Drude) absorption, resulting from an excess pump-induced carrier population, similar to what has been reported recently in graphene [137]. For a better understanding of the anisotropy of the signal, the amplitude of the positive peak at 0 ps and the amplitude of the negative transmission at a time delay of 10 ps is plotted in Fig. 4.5. While both components of the transient response depend on the probe polarization, the slower negative transient response shows a much more pronounced anisotropy, and is nearly absent when the probe is horizontally polarized. The stronger anisotropy of the delayed absorption is likely explained by the large differences in the carrier mobility in black phosphorus. The mobility in few-layer black phosphorus has been recently calculated to be around 400 and 1,500 $\mathrm{cm^2V^{-1}s^{-1}}$ for electrons moving parallel or perpendicular to the corrugations, respectively [115], which could explain the observed anisotropic transient response. Our observations regarding the angular dependence of the signal amplitude for pump and probe polarization agree well with the findings in [132] noting that the anisotropy is more pronounced for changes in the probe polarization. Additional theoretical modelling is needed to fully understand the mechanisms governing the polarization anisotropy of the pump-induced change in transmission.

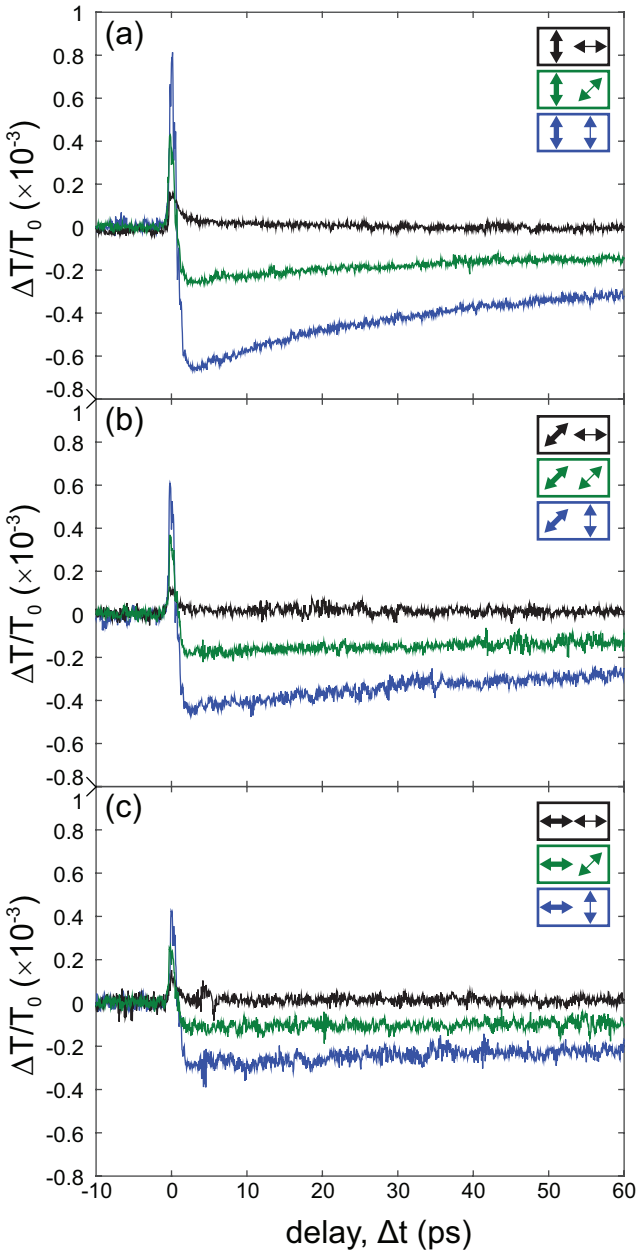

Figure 4.4: Polarization-resolved pump-probe signals. Each panel shows a set of curves for a fixed pump and varied probe polarization. In the legend, the thick (thin) arrow designates the pump (probe) polarization.

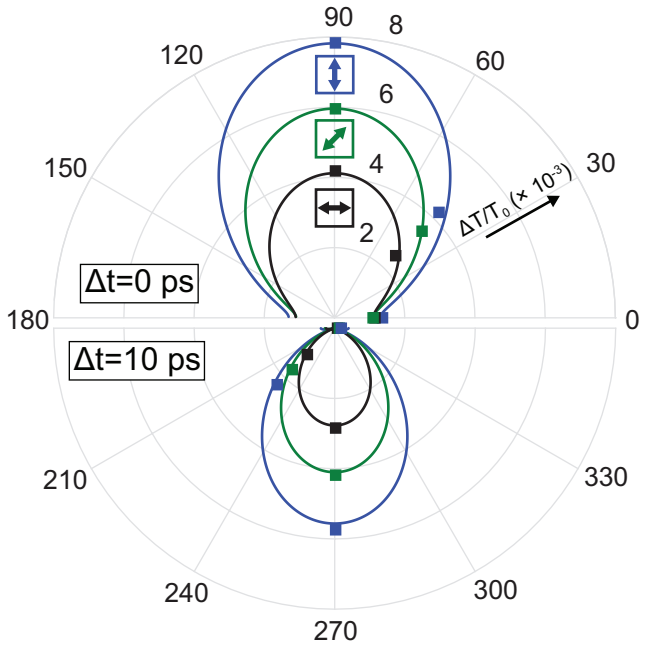

Figure 4.5: $\Delta T/T_0$ at 0 ps (upper half-circle) and 10 ps (lower half-circle) for all pump-probe polarization configurations as a function of probe polarization angle. The colored arrows indicate the pump polarization. The solid lines are phenomenological fits of the form: $a\cos^2\Phi_p + b\sin^2\Phi_p$.

4.3.4 Summary

In summary, two-color pump-probe experiments were conducted on thin layers of black phosphorus in a transmission geometry. We observed a transient photobleaching on the time scale of the temporal resolution of the measurement followed by a long-lived pump-induced absorption exhibiting two characteristic time scales on the order of 180 ps and 1.3 ns. Polarization-resolved measurements revealed an anisotropy that was stronger for the time delayed portion of the response and is

attributed to the strong anisotropy of the electron mobility in black phosphorus. These results emphasize the importance of polarization and black phosphorus orientation in optoelectronic devices as well as purely optical devices that make use of the material's nonlinear optical properties.

4.4 Black Phosphorus Photoconductive Detector

4.4.1 Overview

Atomically thin multilayers of black phosphorus exhibit many desirable qualities for optoelectronic applications [120]. As described in section 4.3.2, it possesses an electronic bandgap that depends on the number of layers - achieving its bulk value of 300 meV if there are greater than approximately 5 of them [115]. In addition, black phosphorus has a high carrier mobility and can be electronically gated via the field effect [115, 120]. There has been significant research studying this material for use in photodetection [117, 127] and understanding the properties and physical origin of the photoresponse remains an active area of research. In this section we present electrical and optical measurements that characterize the properties of a black phosphorus photoconductive detector based on a field effect transistor (FET) platform. These measurement provide details on the origin and speed of the detection mechanism and also demonstrate fast detection at mid-infrared frequencies.

4.4.2 Characterization and Discussion

Atomically thin flakes of black phosphorus were produced by mechanical exfoliation from a bulk crystal and were subsequently transferred to a substrate consisting of a low-doped silicon wafer that was uniformly covered with 300 nm of thermally grown SiO_2. This oxide provides electrical insulation between the black phosphorus flake and the conductive substrate that serves as the gate electrode. Electrodes were defined using standard contact photolithography and metal liftoff. The electrodes are comprised of 10 nm of chromium as wetting layer and 100 nm of gold and form a 5 µm channel across an approximately 20 layer thick black phosphorus flake. An encapsulating Al_2O_3 cover layer of 100 nm was added to safeguard the black phosphorus flake against degradation from exposure to the ambient environment. Linear optical transmission measurements indicate around $20 - 40\,\%$ absorption in the flake; indicating the number of layers of black phosphorus to be between $8 - 20$ layers for the devices presented in this section. An image of the device is shown in Fig. 4.6(a).

The electrical gating characteristics of the black phosphorus FET were determined by monitoring the source drain current through the FET channel at a constant source-drain bias of V_{SD} while sweeping gate voltage (c.f. Fig. 4.6). At negative voltages the sample is p-doped (i.e., holes are the majority carriers) while at positive voltages the sample is n-doped (i.e., electrons are the majority carriers). At the charge neutral point of the device shown in Fig. 4.6(a) ($V_G = 23\,V$) the chemical potential is located in the bandgap of the material and the total number of charge

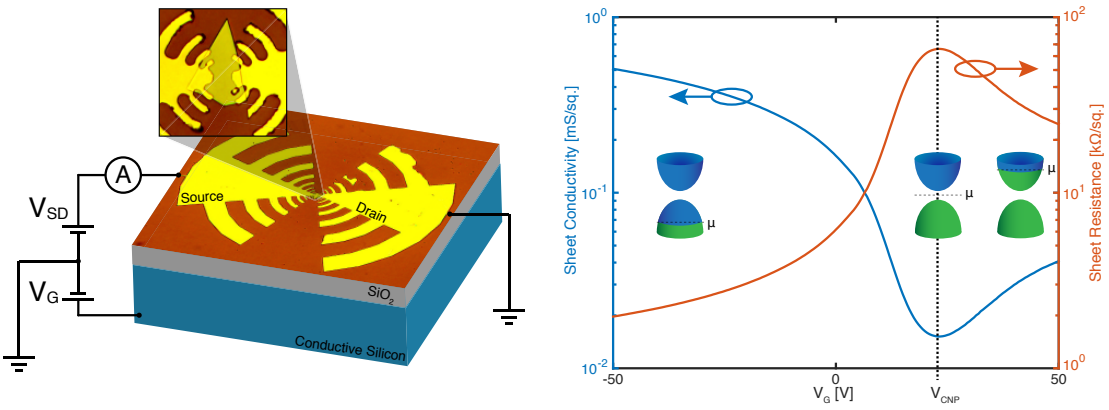

Figure 4.6: (a) Diagram of black phosphorus FET with integrated antenna: A = ammeter, V_{SD} = source-drain voltage, V_G = gate voltage. Inset shows black phosphorus flake and metal contacts. (b) Gating curve for black phosphorus FET showing sheet conductivity and resistance. The inset shows the relative level of the chemical potential with respect to the conduction and valence bands in the material.

carriers is minimized (resulting in a peak(minimum) in the resistance(conductance)). This measurement further indicates that the black phosphorus flakes used in the experiment are intrinsically p-doped (i.e., electrons must be added to the flake by applying a positive voltage to bring the sample to charge neutrality). The electrical gating measurements can also be used to estimate the carrier mobility in the sample. Assuming a simple Drude conductivity (and ignoring the anisotropy in the electrical transport) allows us to write the following expression for the sheet resistance of the black phosphorus flake:

$$R = \frac{L}{W}\frac{1}{\sigma} = \frac{\Gamma}{q\mu n}. \tag{4.1}$$

In the above expression $\Gamma = L/W$ contains the geometrical factor of the resistance (length, L, and width, W) and $\sigma = q\mu n$ is the DC Drude conductivity. The term q is the elementary charge, μ is the mobility, and n is the carrier density. The carrier field effect mobility is estimated from the electrical transport measurements by [126]:

$$\mu_{FE} = \frac{\Gamma}{C_{BG}}\frac{dG}{dV_G}\bigg|_{V_{linear}}. \tag{4.2}$$

In the above expression C_{BG} is the capacitance of the back-gate formed by the substrate-oxide-flake structure, and $dG/dV_G\Big|_{V_{linear}}$ is the derivative of the conductance with respect to the voltage evaluated at the linear regions of the transport

curve. This formula assumes the charge accumulates on the flake like an ideal capacitor and the conductivity described by the Drude model. Using the linear regions of the sheet conductance curve near the charge neutral point (cf. Fig. 4.6) the hole and electron mobility are found to be $\mu_h = 846\,\mathrm{V^{-1}cm^{-2}s^{-1}}$ and $\mu_e = 95\,\mathrm{V^{-1}cm^{-2}s^{-1}}$.

To understand the photodetection mechanism, the FET channel is illuminated from the top by a near infrared ($\lambda = 1.56\mu\mathrm{m}$, $\hbar\omega = 800\,\mathrm{meV}$) fiber laser. The pulse duration is 100 fs and an average power of 5 mW, and was focussed using a high NA aspherical lens to a spot size of approximately 3 μm. The laser pulses are mechanically chopped and the photocurrent is converted to a voltage by a transimpedance amplifier before being measured with a lock-in amplifier. Position dependent photocurrent measurements show a non-zero signal that is peaked at the center of the channel only when the bias voltage is non-zero, suggesting that the detection mechanism is photoconductive in nature. At zero source-drain bias, scanning photocurrent measurements across the FET channel reveal oppositely signed peaks at the contacts, a signature consistent with a photovoltaic effect that has also observed by others [130]. The position dependent scan is shown in Fig. 4.7(a).

The possibility of a thermal detection mechanism was also explored by conducting temperature dependent electrical transport measurements. In a bolometric detector, an incident laser pulse with power, P, could heat the sample (change the temperature, T) which would change the resistance, R, of the material ($\frac{dR}{dP} = \frac{dR}{dT}\frac{dT}{dP} \neq 0$). The change in resistance could be monitored with the appropriate electrical readout (requiring a bias voltage or current). To study this potential detection mechanism, the temperature dependence of the resistance was measured by

uniformly heating the device on a hot plate and measuring the current through the flake as a function of back-gate voltage. The uniform heating ensures no diffusive, gradient-based heat currents influence the measured signal, and that the change in conductivity results solely from the temperature dependence of the black phosphorus resistance. The electrical transport measurements for a range of temperatures are plotted in Fig. 4.7. In the hole doped regime a clear decrease in the conductivity is seen with increasing temperature - a signature of an increased carrier scattering rate [76]. Near the charge neutral point the conductivity is seen to increase with increasing temperature suggesting that thermally activated carriers are increasing the carrier density and producing a decreased conductivity. Each of these effects are linear with temperature and indicate that at a particular gate voltage an incident laser pulse could produce an increased or decreased resistance assuming there is sufficient photo-induced heating.

The detector shown in Fig. 4.6(a) was tested at room temperature using three wavelengths spanning the near and mid-infrared frequency range in the intrinsic p-doped regime (i.e., $V_G = 0\,V$). These measurements were carried out using a pulsed sources and a 40 GHz sampling oscilloscope that could resolve the temporal impulse response of the detector. The pulsed sources had wavelengths of 1.56μm (same laser as was used for the position dependent scans shown in Fig. 4.7), 2.5μm, and 3.6μm (these last two wavelengths were generated using filtered supercontinuum light generated in a nonlinear fiber that is seeded by ultrafast ≈ 25 fs pulses). This approach provides information about the operating speed of the detector as well as information about the origin of the photoresponse. To ensure the operating

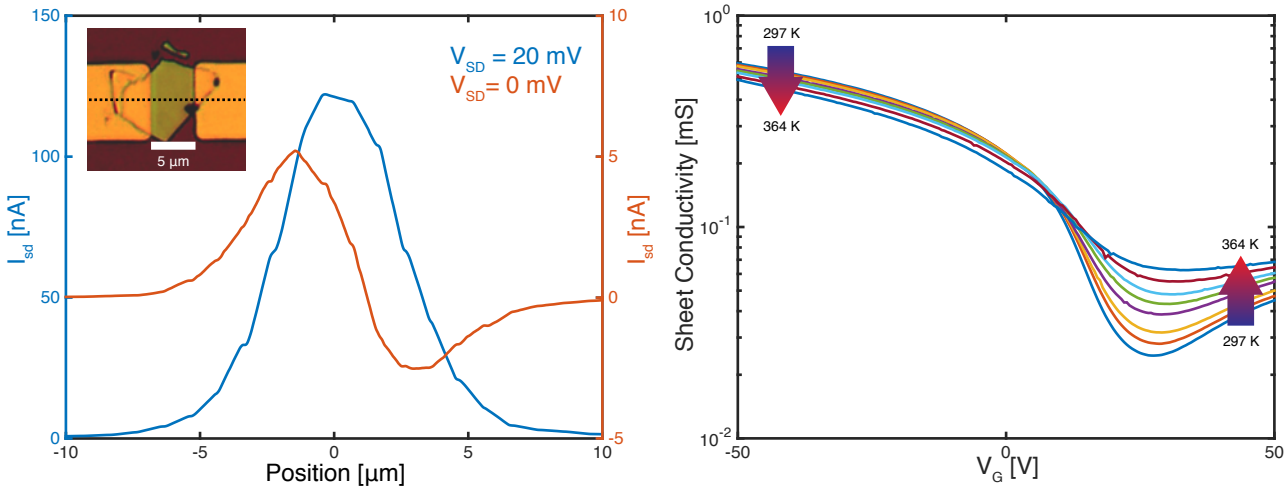

Figure 4.7: (a) Position scan across FET channel (see inset) with and without source-drain bias. (b) Gating curve for black phosphorus FET as a function of temperature.

speed was not hindered by stray capacitances, the device was packaged and wired to a high-frequency SMK connector. The photosignal was amplified by a 20 GHz voltage amplifier with a < 28 ps rise time and connected to the source-drain voltage supply via a bias-T. An image of the packaged device an electrical diagram of the measurement are shown in Fig. 4.8.

To analyze the signals we note that the device resistance could be modified by either a photoconductive or bolometric effect. Since we are illuminating the center of the channel and applying a large bias, the photoconductive effect is expected to be dominant in this operational mode. Referring to the circuit shown in Fig. 4.8(b), if we assume the device resistance, R_D, is large compared to the input impedance of the amplifier (i.e., $R_D \gg R_{input} = 50\,\Omega$, cf. Fig. 4.6(b)) then the change in

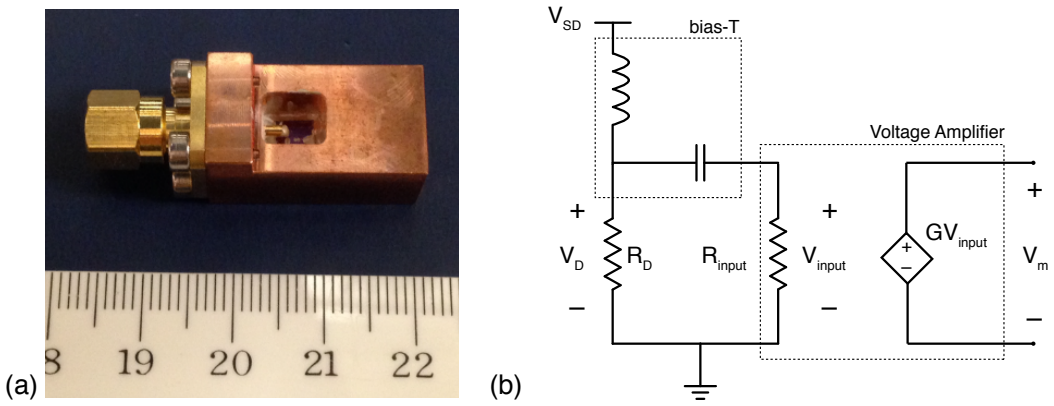

Figure 4.8: (a) Image of packaged, high-speed device used for photocharacterization. (b) Circuit diagram for impulse response measurement.

conductivity can be written as,

$$\frac{\Delta\sigma}{\sigma} \approx \frac{-V_m}{GV_{SD} + V_m}. \tag{4.3}$$

In the above expression V_m is the measured signal voltage, G is the voltage amplifier gain, and V_{SD} is the source-drain voltage. Critically, the sign of the change in the conductivity will indicate if the photoinduced resistance change of the device is positive or negative. If $(\Delta\sigma/\sigma)$ is positive, it indicates that the conductivity is increased from an augmented carrier density due to absorption of the incident light. When the same quantity is negative, however, it suggests that photo-induced heating is decreasing the conductivity (as seen in the direct heating measurements shown in Fig. 4.7). The change in conductivty given by Eqn. 4.3 can be larger than unity as is the case, for example, when using the material as a photoconductive switch. The

AC photo-induced current can be calculated by $i_{AC} = (V_m/GR_i)$.

The room temperature impulse response of the packaged black phosphorus detector is shown in Fig. 4.9. At all wavelengths the change in the conductivity is seen to be positive, indicating the detection mechanism is photoconductive. The photoresponse exhibits a fast response time on the order of 1 ns. Analysis of the peak change in conductivity (inset in Fig. 4.9) shows the expected linear dependence characteristic of a photoconductive response. From the curves given in Fig. 4.9 we can estimate the efficiency, η, by determining the total collected number of charge carriers ($(1/q)\int i_{AC}(t)dt$) and dividing by the number of incident photons, giving a value of $\eta \approx 10^{-4}$. The responsivity is then given by $\widetilde{R} = \eta\lambda[\mu\text{m}]/1.24\text{A/W}$ and was found to be in the range of 250 [μA/W] for the wavelengths tested at a bias voltage of 200 mV[1]. The overall efficiency of our device can be improved by using a thicker flake that would absorb nearly all of the incident radiation (around 20 % absorbed in flake tested) and by increasing the bias voltage.

The next important figure of merit is to determine the noise equivalent power (NEP) of our detector. The NEP gives the power required to achieve a signal-to-noise ratio of unity for a given bandwidth. Therefore a smaller NEP is more desirable. To estimate the NEP, the photoresponse of our detector was measured using a chopped beam and lock-in amplification for different incident average powers. The slope of the curve with respect to the incident power gives the voltage

[1]We note that this equation only applies to wavelengths with corresponding photon energies above the material bandgap. Though the efficiency can exceed unity for a photoconductive detector, calculating the responsivity provides a useful means of comparison to other detectors.

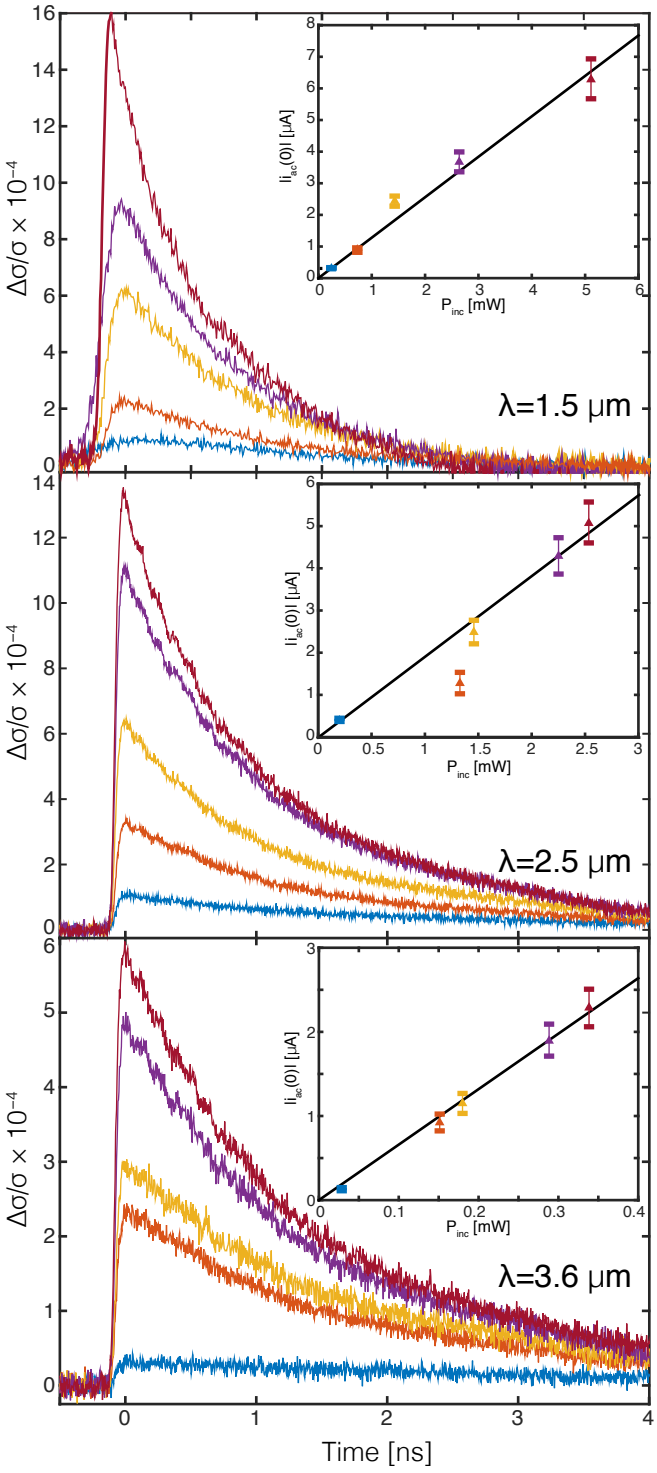

Figure 4.9: Impulse response measurements of black phosphorus detector at near- and mid-infrared wavelengths. The inset shows the linearity of the photoresponse peak (peak AC current) with incident power.

responsivity of the detector (units of V/W). The noise floor gives the voltage level with contributions background, electrical pickup, and the thermal noise of our detector and is measured when the incident power blocked. Dividing the measured noise voltage level by the responsivity, and then dividing by the square root of the bandwidth of the measurement (i.e., multiplying by $\sqrt{2\tau_{int}}$ where τ_{int} is the integration time of the measurement) gives an estimated NEP of $\approx 530\,\mathrm{pW}/\sqrt{\mathrm{Hz}}$ for a 200 mV bias voltage. This figure is around one hundered times larger than that predicted by using the Johnson noise contribution from the detector resistance alone ($\sqrt{4k_BTR}\,[\mathrm{V}/\sqrt{Hz}]$), where k_B is the Boltzmann constant, T is the temperature, and R is the device resistance), suggesting that background and pickup noise likely contribute to the measurement-based NEP value.

4.4.3 Summary

We've demonstrated a photoconductive detector based on black phosphorus operating at mid-infrared wavelengths. The detector shows a fast extrinsic (i.e., including circuit parasitics) response time on the order of 1 ns, indicating that gigahertz class detection is possible. The noise equivalent power was estimated using a lock-in measurement showing a value of $530\,[\mathrm{pW}/\sqrt{\mathrm{Hz}}]$ for a 200 mV bias voltage. An estimation of the responsivity for the bias voltage of 200 mV was determined to be of order $250\,[\mu\mathrm{A/W}]$, indicating that black phosphorus is a promising material for room temperature mid-infrared detection.

Chapter 5: Future Directions

5.1 Overview

Though two-dimensional materials were first analyzed in the 1950's by Wallace [50], their research did not experience wide popularity until relatively recently [48]. Once determined that single-layer graphene could be experimentally isolated and was thermodynamically stable, other van der Waals materials were rapidly studied in a similar fashion (e.g., the transition metal dicalcogenides and black phosphorus). While there is much work remaining in understanding many of the characteristics and properties of these two-dimensional materials in isolation, an emerging area of research exploiting heterostructures made by combining multiple types of atomically thin materials to tailor their optical and electrical properties is gaining momentum. For example, in [138] graphene has been combined with insulating hexagonal boron nitride through successive exfoliation and transfer steps to enhance the mobility in the graphene layer by over an order in magnitude. Similarly, patterning of these materials has also become attractive, especially in the field of plasmonics. In one popular example, graphene has been patterned into nanoribbon arrays for the purpose of momentum matching the free-space propagating wave to the surface-bound plasmon mode [62]. Advances in two-dimensional materials research will result from

the discovery and practical application of the novel physics created by using both composite materials and nanopatterning to engineer the light-matter interaction. In the following section specific next steps on the work presented in this thesis are given.

5.2 Optoelectronics with Atomically Thin Black Phosphorus

Fully realizing black phosphorus as a mid-infrared material for detection, mixing, and emission is of considerable scientific and technological interest. The pathway forward for black phosphorus will be in taking advantage of the materials naturally high mobility, unique anisotropic behavior, and mid-infrared bandgap. All of these features suggest the possibility of a high-speed polarization sensitive photonic components.

One possibility would be to exploit the high on-off ratios in black phosphorus field effect transistors and the change in photoconductivity described in 4.4 to create a photo-conductive switch. Due to the high mobility of black phosphorus (as evidenced by the fast response times shown in 4.4) the fast migration of charge carriers across the channel could produce terahertz radiation. If successful, this would be the first demonstration of terahertz emission utilizing a two-dimensional material and would, in principal, work at wavelengths up to the material band gap (approximately 4 μm). Sensitive electro-optic sampling techniques [139] could be used to detect the emitted terahertz radiation.

Another potential study would examine the polarization dependence of the

photocurrent in electrically connected black phosphorus. Due to the anisotropic electrical conductivity and optical absorption in black phosphorus, the study would aim to understand the relationship of the polarization of the absorbed incident light and the resulting photocurrent. If the two are correlated, this would indicate that the carriers generated from absorption would maintain some degree of the incident photon momentum (that is, the light polarized along the high conductivity axis of the crystal would generate a stronger current in the direction of this axis than the low conductivity axis). This experiment would require a simultaneous measurement of the photocurrent generated by linearly polarized light along the fast and slow axis of the material. This measurement could be done using a lock-in based approach or a pulsed measurement using a sampling oscilloscope. One potential realization of this measurement is shown in Fig. 5.1. If a relationship is found between the incident polarization and the measured photocurrent along each axis of the material, this allows for the possibility of a single-element detector capable of detecting both the intensity and polarization of the incident radiation.

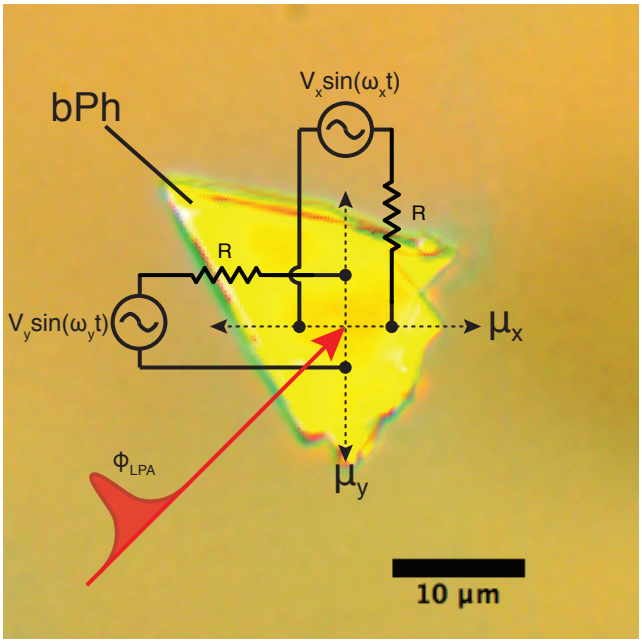

Figure 5.1: Polarization resolved photocurrent measurement showing differing sinusoidal current bias applied (realized via a large current limiting resistor, R, in series with a voltage source) along the two in-plane mobility axes of the material (an optical micrograph of a black phosphorus flake is shown with scale bar). Measuring the photovoltage due to the linearly polarized light (with linear polarization angle Φ_{LPA}) across the device using lock-in amplification could reveal information about the relationship between the incident light polarization and the photocurrent.

Chapter A: Appendix A - Experimental Methods

This appendix provides detail on the two-frequency pump-probe heterodyne technique used for many of the studies reported in this thesis.

A.1 Two-Frequency Heterodyne Pump-Probe

Traditional optical heterodyning detects a difference, or beat, frequency generated by the mixing of two optical waves of different frequency in a square-law photo-detector [140, 141]. This beat frequency has a phase and magnitude that is directly related to the optical phase difference and amplitudes of the constituent fields, thus making optical heterodyning an attractive method for pump-probe spectroscopy.

The fidelity of the heterodyne signal is susceptible to uncontrolled mechanical and thermal effects introduced by sample heating, thermal relaxation of the opto-mechanical components comprising the system, as well as by laser power fluctuations. A comprehensive study of thermal drift in optical heterodyne systems can be found in [142]. These effects introduce instability into the signals of interest and specialized approaches utilizing radio receivers [30, 143, 144] or fast measurements with radio-frequency lock-in detection [31] have been employed to mitigate them.

In this study, we introduce a heterodyning technique that detects two heterodyne signals; a technique thus requiring two lock-in detectors or a single lock-in detector with two phase sensitive channels (in this work we used a single Signal Recovery 7270 with dual-phase lock-in detection). A detailed discussion of the dual-frequency heterodyning technique is provided in this appendix.

In contrast to conventional pump-probe heterodyne experiments, deleterious thermal drift and power fluctuation effects in the two-frequency technique are managed by additionally chopping our pump signal. Chopping the pump signal produces sidebands at $\pm f_C$ from the heterodyne frequency, where f_C is the chopping frequency. It will be shown that measurement of one of the sidebands in addition to the primary heterodyne signal provides a simple and robust means of eliminating noise, particularly phase drift, in the heterodyne measurement. It should also be noted that a judicious choice of the heterodyne frequency to be an odd integer multiple of the chopper half-frequency (i.e., $f_H = N\frac{f_C}{2}$, N = odd integer), spectrally segregates the strong, co-propagating and co-polarized pump signal from the heterodyne signal; further improving the signal to noise ratio of the measurement.

Essential to the success of this method is that a common master clock is used to generate the frequencies driving the AOFs, the chopper, and the reference input on the lock-in detector. This ensures that a common phase relationship is maintained between all beams and detection hardware in the experiment. For the measurements reported here, we used a four-channel, 171 MHz digital digital signal generator (Novatech Intruments Inc. Model 409B, which incorporates the Analog Devices AD9959 programmable synthesizer chip.) The first two channels were programmed

to generate the 35 MHz and 35.0625 MHz signals required to drive the AOFSs. The third channel produces a $f_c = 1$ kHz signal that was used to drive the optical chopper. The fourth output of the synthesizer was programmed to produce a 500 Hz reference frequency equal to half of the chopper frequency that was sent to the lock-in amplifier. The lock-in amplifier was then configured to simultaneously measure at both 62.5 kHz and 63.5 kHz (i.e., the 125th and 127th harmonics of the reference frequency.) The heterodyne frequency is specifically chosen to be an odd integer multiple of the chopper half-frequency, which ensures that there is no interference from higher harmonics of the strong chopped pump pulse.

In order to unambiguously measure the relative phase and intensity shift, the correct phase relationship must be established between the pump beam and the chopper wheel since a phase offset can occur depending on the relative spatial position of the pump beam in the chopper wheel slot and the chopper wheel position with respect to the photo-interrupter in the chopper wheel controller. To eliminate this phase offset, the phase of the detected pump signal at the chopping frequency is zeroed in the lock-in amplifier immediately prior to conducting measurements.

Figure A.1 illustrates the principle of operation of the two-frequency lock-in detection, for a fixed pump delay. When the probe and reference pulses interfere with one another in the balanced detector, they produce a sinusoidal heterodyne signal at the heterodyne frequency $f_H (= 62.5$ kHz). We note that the detectors used are not fast enough to resolve the individual pulses (≈ 500 fs) or their repetition period (10 ns). As illustrated notionally in Fig. A.1(a), the magnitude and phase of the heterodyne signal depends on whether the pump is on or off. When the pump

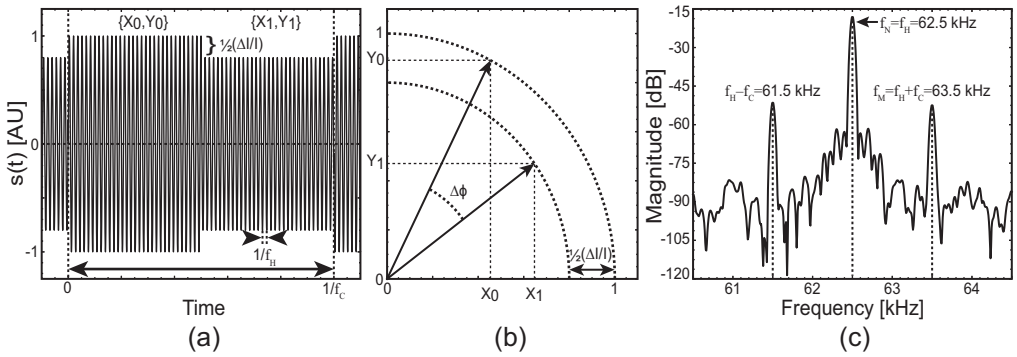

Figure A.1: (a) Notional time series data showing the function $s(t)$ over one chopping period as described by Eq. (A.1). The chopper wheel blocks or passes the pump beam in time intervals of length $\frac{1}{2f_c}$ with the sinusoidally varying signal in each interval being described by $\{X_0, Y_0\}$ or $\{X_1, Y_1\}$ respectively. (b) Component representation of the notional time series is shown in the first quadrant of the in-phase and quadrature-phase plane. (c) Measured frequency spectrum of $s(t)$ with relevant harmonics indicated. Harmonics of the collinear pump, which occur at even integer multiples of the 0.5 kHz lock-in amplifier reference frequency, are suppressed through the use of balanced detection.

intensity is chopped, the received signal $s(t)$ may be written as a periodic signal:

$$s(t) = \begin{cases} X_1 \cos(Nt) + Y_1 \sin(Nt) & -\pi < t \leq -\frac{\pi}{2} \\ X_0 \cos(Nt) + Y_0 \sin(Nt) & -\frac{\pi}{2} < t \leq 0 \\ X_1 \cos(Nt) + Y_1 \sin(Nt) & 0 < t \leq \frac{\pi}{2} \\ X_0 \cos(Nt) + Y_0 \sin(Nt) & \frac{\pi}{2} < t \leq \pi \end{cases} \tag{A.1}$$

In this expression, the the period 2π represents two full chopping cycles and $N(=125)$ heterodyne cycles, where N is an odd number. The coefficients X_0 and Y_0 represent the in-phase and quadrature-phase components of the heterodyne signal when the pump is off, while X_1 and Y_1 correspond to the in-phase and quadrature-phase components when the pump is on. Figure A.1(b) illustrates vector component representation of heterodyne signal when the pump is off and on, illustrating the change in intensity and phase.

Figure A.1(c) shows a representative spectrum of the received signal $s(t)$, measured using an electrical spectrum analyzer. In addition to the heterodyne tone at $f_H(= 62.5$ kHz), we see sidebands at $f_H \pm f_C$, where f_C is the chopping frequency (1 kHz.) The lock-in detector is configured to simultaneously measure the Fourier components at f_H and $f_H + f_C$.

The periodic signal $s(t)$ can be expanded in a Fourier series:

$$s(t) = \frac{x_0}{2} + \sum_{n=1}^{\infty} x_n \cos(nt) + y_n \sin(nt) \tag{A.2}$$

with the expansion coefficients being given by:

$$x_n = \frac{1}{\pi} \int_{-\pi}^{\pi} s(t) \cos(nt) dt, \qquad n = 0, 1, 2, \ldots \tag{A.3}$$

$$y_n = \frac{1}{\pi} \int_{-\pi}^{\pi} s(t) \sin(nt) dt, \qquad n = 1, 2, \ldots \tag{A.4}$$

Substituting Eq. (A.1) into Eqs. (A.3-A.4), we obtain the following expressions for the Fourier cofficients at the heterodyne frequency ($n = N(= 125)$) and at

the first upper sideband ($n = M = N + 2(= 127)$):

$$x_N = \frac{X_0 + X_1}{2} + \frac{Y_1 - Y_0}{\pi N} \tag{A.5}$$

$$y_N = \frac{Y_0 + Y_1}{2} + \frac{X_1 - X_0}{\pi N} \tag{A.6}$$

$$x_M = \frac{Y_0 - Y_1}{\pi} \tag{A.7}$$

$$y_M = \frac{X_1 - X_0}{\pi} \tag{A.8}$$

The dual-frequency lock-in detector employed in these experiments allows for simultaneous measurement of these four quantities, although we note that with a appropriate reference signals the four quantities could be also measured using two independent lock-in amplifiers. From these four measured quantities, one can calculate the the Fourier coefficients of the heterodyne signal when the pump is off (X_0, Y_0) and on (X_0, Y_0).

$$X_0 = x_N + \frac{1}{N} x_M - \frac{\pi}{2} y_M \tag{A.9}$$

$$Y_0 = y_N - \frac{1}{N} y_M + \frac{\pi}{2} x_M \tag{A.10}$$

$$X_1 = X_0 + \pi y_M \tag{A.11}$$

$$Y_1 = Y_0 - \pi x_M \tag{A.12}$$

From these results we can calculate the relative change in intensity, $(\Delta I/I)$, and change in phase, $\Delta\phi$,

$$\left(\frac{\Delta I}{I}\right) = \frac{X_1^2 + Y_1^2}{X_0^2 + Y_0^2} - 1 \tag{A.13}$$

$$\Delta\phi = \tan^{-1}\left(\frac{Y_1}{X_1}\right) - \tan^{-1}\left(\frac{Y_0}{X_0}\right) \tag{A.14}$$

This approach subtracts off the intensity and phase noise fluctuations common to both measured harmonics leaving only the change in intensity and phase resulting from the presence of the pump pulse.

For small changes in the relative intensity and phase, or equivalently, when the Fourier amplitudes satisfy $(x_M, y_M) \ll (x_N, y_N)$, Eqs. (A.13-A.14) can be expanded to first order to give

$$\left(\frac{\Delta I}{I}\right) = 2\pi \left(\frac{x_N y_M - y_N x_M}{x_N^2 + y_N^2}\right) \tag{A.15}$$

$$\Delta\phi = -\pi \left(\frac{x_N x_M + y_N y_M}{x_N^2 + y_N^2}\right) \tag{A.16}$$

Chapter B: Appendix B - Carrier Dominated Pulse Propagation Analysis

B.1 Overview

This appendix gives a derivation of a simplified pulse propagation model for the case of a weak probe pulse under the influence of a pump-induced carrier population. The results given here can be used to model pump-probe signals in a material dominated by carrier effects.

B.2 Simplified Propagation Equation

Pulse propagation in an optical waveguide can be described by the following scalar differential equation [13]:

$$\frac{\partial}{\partial z}u(z,t) = -\left(\frac{\alpha}{2} + i\frac{\beta_2}{2}\frac{\partial^2}{\partial t^2} + i\frac{\omega}{c}\Delta n_{FCA}(z,t) + \frac{1}{2}\Delta\alpha_{FCA}(z,t)\right)u(z,t) + \left(i\frac{\omega}{c}n_2 - \frac{\beta}{2}\right)\frac{|u(z,t)|^2}{A_{\text{eff}}}u(z,t). \tag{B.1}$$

In the above equation the various terms are given as follows: α is the linear absorption coefficient, β_2 describes the group velocity dispersion, n_{FCA} and α_{FCA} account the index and absorption change due to free carriers, n_2 and β are the Kerr and two-photon absorption coefficient, A_{eff} is the effective mode area in the waveg-

uide, ω is the optical frequency, c denotes the speed of light in vacuum, and $u(z,t)$ is the slowly varying pulse envelope which is normalized to give the optical power in the mode when $|u(z,t)|^2$ is calculated. The above equation must be solved for both the pump and probe pulses in addition to another differential equation describing the evolution of the free-carriers in the waveguide produced by the absorption of the pump and probe fields. Next we will describe several simplifying assumptions that will allow for an analytic solution of the probe field, $u_{\mathrm{p}}(z,t)$, where the subscript 'p' is used to indicate the probe (the probe field is of interest since the experimentally measured quantity is $\propto |u_{\mathrm{p}}(z,t)|^2$).

First we assume that the dispersion in the waveguides can be neglected since the dispersion length $L_D = T_0^2/|\beta_2| >> L$ where L is the length of the waveguide under investigation (a valid assumption for waveguides of a few millimeters and a dispersion parameter less than, of order, $2\,\mathrm{ps}^2\,\mathrm{m}^{-1}$ corresponding to a $D_2 \approx 1500\mathrm{ps}\,\mathrm{nm}^{-1}\,\mathrm{km}^{-1}$ at telecommunications wavelengths). This allows us to remove the second derivative term from the separate, but coupled, equations governing the pump and probe field envelopes. The second assumption is that the probe pulse is weak and only subject to linear absorption and free-carrier absorption and dispersion effects that result from the pump pulse (i.e., the Kerr effect and two-photon absorption can be ignored). The carrier effect assume a Drude-like response, in that the absorption and dispersion are assumed to be directly related to the free-excess free carrier population. The carrier absorption and refraction coefficients can then be written as:

$$\Delta\alpha_{\mathrm{FCA}}(z,t) = \sigma_{\mathrm{FCA}}\Delta N(z,t) \tag{B.2}$$

$$\Delta n_{\mathrm{FCA}}(z,t) = k_{\mathrm{FCA}}\Delta N(z,t). \tag{B.3}$$

In the above expressions we have the carrier cross section given by, σ_{FCA}, and carrier dispersion given as k_{FCA}. The excess carrier concentration is given as $\Delta N(z,t)$ and is a function of the pump field. The final assumption relies on the notion that the pump pulse is not affected by the carriers it generates, that is, their is no self-amplitude or phase modulation of the pump due to carrier effects. Using these assumptions, we can write the pump and probe pulse evolution equations as:

$$\frac{\partial}{\partial z}u_{\mathbf{P}}(z,t) = -\left(\frac{\alpha}{2}\right)u_{\mathbf{P}}(z,t) + \left(i\frac{\omega}{c}n_2 - \frac{1}{2}\beta\right)\frac{|u_{\mathbf{P}}(z,t)|^2}{A_{\mathrm{eff}}}u_{\mathbf{P}}(z,t) \tag{B.4}$$

$$\frac{\partial}{\partial z}u_{\mathrm{p}}(z,t) = -\left(\frac{\alpha}{2} + \left[i\frac{\omega}{c}k_{FCA} + \frac{1}{2}\sigma_{FCA}\right]\Delta N(z,t)\right)u_{\mathrm{p}}(z,t). \tag{B.5}$$

Equation B.4 can be rewritten into a more convenient form if we write the complex field amplitude as $u(z,t) = |u(z,t)|e^{i\phi(z,t)}$, where we have done a standard phasor conversion. Substituting this into Eqn. B.4, using the definition $I(z,t) = |u(z,t)|^2/A_{\mathrm{eff}}$ where $I(z,t)$ denotes the intensity, and separating into real and imaginary components gives:

$$\frac{\partial}{\partial z}I_{\mathbf{P}}(z,t) = -\alpha I_{\mathbf{P}}(z,t) - \beta I_{\mathbf{P}}(z,t)^2 \tag{B.6}$$

$$\frac{\partial}{\partial z}\phi_{\mathbf{P}}(z,t) = \frac{\omega}{c}n_2 I_{\mathbf{P}}(z,t) \tag{B.7}$$

The solution to Eqn. B.6 is of particular importance for the present analysis:

$$I_{\mathbf{P}}(z,t) = \frac{I_{\mathbf{P}}(0,t)e^{-\alpha z}}{1+\beta I_{\mathbf{P}}(0,t)L_{\text{eff}}(z)}. \tag{B.8}$$

The effective length, denoted as $L_{\text{eff}(z)}$ in the above expression, is given by $L_{\text{eff}}(z) = (1-e^{-\alpha z})/\alpha$. In the limit of $\alpha \to 0$ the effective length goes to the natural length z and 0 for the case of $\alpha \to \infty$. We also note that in the above expression if β is set to zero we recover the expected result $I_{\mathbf{P}}(z,t) = I_{\mathbf{P}}(0,t)e^{-\alpha z}$. This equation describes the pump intensity that is depleted by both linear and two-photon absorption.

Now that we have the solution to the pump intensity, we can consider the excess carrier population generated by the strong pump pulse. For optical waveguides we consider a material whose bandgap is above the single-photon absorption energy and assume that the generated number of carriers is related only to those produced by two-photon absorption (the linear absorption then results mainly from scattering losses). The excess carrier concentration can be described by the following differential equation:

$$\frac{\partial}{\partial t}\Delta N(z,t) = \frac{\beta}{2\hbar\omega}I_{\mathbf{P}}^2(z,t) - \frac{\Delta N(z,t)}{\tau_c}. \tag{B.9}$$

Above the term τ_c denotes the carrier recombination time. For many practical cases of interest, the exciting pump pulse with pulse width tau_P, is much shorter than the carrier recombination time scale (i.e. $\tau_P \ll \tau_c$). For this case Eqn. B.9 can be simplified to a homogeneous equation subject to the initial condition $\Delta N(z,0)$,

which is given by:

$$\Delta N(z,0) \approx \frac{\beta}{2\hbar\omega}\int_{-\infty}^{+\infty} I_{\mathbf{P}}^2(z,t)dt = \Delta N_0(z). \tag{B.10}$$

To evaluate the above equation, we can employ Eqn. B.8. Here we must specify a more exact form for the initial pump pulse: $I_{\mathbf{P}}(0,t) = I_{0,\mathbf{P}}f(t)$, where $I_{0,\mathbf{P}}$ is the peak on-axis pump intensity and $f(t)$ describes the temporal shape of the pulse (e.g., $f(t) = \mathrm{sech}^2(t/\tau_P)$). The solution to the homogeneous form of Eqn. B.9 can then be found as:

$$\Delta N(z,t) = \Delta N_0(z)e^{-t/\tau_c}. \tag{B.11}$$

The above expression describes an excess carrier population at position z that decays exponentially with time constant τ_c. This equation applies for times greater than time zero ($t = 0$) which is the arrival time of the pump pulse (the function is zero otherwise).

We can now use Eqn. B.11 in the equation for the probe field (Eqn. B.5) to solve for the intensity and phase of the probe. The probe will experience free-carrier effects due to the excess carrier concentration given in Eqn. B.11. Depending on the relative delay of the pump and probe and also the different propagation speed of the pump and probe (which will be different due to the optical Kerr effect and free-carrier dispersion respectivly), the carrier concentration influencing the probe will be determined by the time dependent part of Eqn. B.11. Since the nonlinear contribution to the refractive index is typically treated as a perturbation to the linear refractive index, we assume that the time delay between the pump and probe

remains constant (i.e., the time delay is set experimentally to be a value τ and is unaffected by the different propagation speeds of the pump and probe pulses). This gives the excess carrier concentration experienced by the probe pulse to be: $\Delta N_0(z)e^{-\tau/\tau_c}$.

Equation B.5 is solved in the same way as the pump equation (i.e., we can write the field as a phasor quantity and arrive at two differential equations). The resulting equations describing the probe are:

$$\frac{\partial}{\partial z} I_{\mathrm{p}}(z,t) = -\left(\alpha + \sigma_{\mathrm{FCA}} \Delta N_0(z) e^{-\tau/\tau_c}\right) I_{\mathrm{p}}(z,t) \tag{B.12}$$

$$\frac{\partial}{\partial z} \phi_{\mathrm{p}}(z,t) = -\frac{\omega}{c} k_{\mathrm{FCA}} \Delta N_0(z) e^{-\tau/\tau_c} \tag{B.13}$$

These equations can be integrated directly to find the probe intensity and phase and are valid for times larger than the pump-pulse overlap time (i.e., they describe the probe in the regime where the effect of the pump is only that of the pump-induced carrier effects).

Chapter C: Appendix C - Graphene Optical Parameters

Derivation of the reflection and transmission coefficients are determined for a graphene layer separating two dielectrics. The resulting equations are analyzed at various limits for several practical cases of interest.

C.1 Optical Properties of a Metallic Film

Here we derive the optical parameters for a lossy film separating two dielectric half-spaces having different relative permittivities (see Figure Appendix B). For this we use a scattering matrix approach to calculate the reflectance and transmittance through the lossy material.

To begin, we use the following two *transfer* matrices to describe the propagation of light through a cascade of optical elements (across a material boundary ($x \rightarrow y$), through a uniform medium (z) of length d, and accross a second boundary).

$$\overline{\overline{M}}_{xy} = \frac{1}{t_{yx}} \begin{bmatrix} 1 & r_{yx} \\ r_{yx} & 1 \end{bmatrix} \qquad \overline{\overline{M}}_{c} = \begin{bmatrix} e^{-ik_c d} & 0 \\ 0 & e^{+ik_c d} \end{bmatrix} \tag{C.1}$$

The above matrices use the transmission and reflection coefficients $t_{ab} = \frac{2n_a}{n_a+n_b}$ and $r_{ab} = \frac{n_a-n_b}{n_a+n_b}$ and wave vector $k_c = \frac{2\pi}{\lambda} n_c$ where λ is the vacuum wavelength and

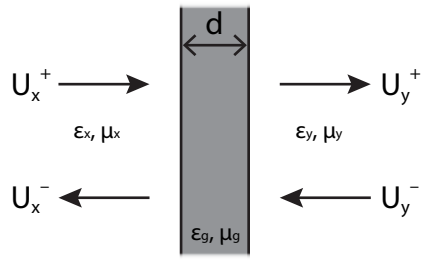

Figure C.1: Diagram defining field amplitudes and directions for scattering matrix formalism.

n_c is the complex refractive index of the matrial. Cascading three matrices (first boundary, propagation through film, second boundary) yields the transfer materix through the thin film: $\overline{\overline{M}}_{\text{film}} = \overline{\overline{M}}_{gy} \times \overline{\overline{M}}_{g} \times \overline{\overline{M}}_{xg}$.

$$\overline{\overline{M}}_{\text{film}} = \frac{1}{t_{gx}t_{yg}} \begin{bmatrix} e^{-ik_g d} + r_{gx}r_{yg}e^{+ik_g d} & r_{gx}e^{-ik_g d} + r_{yg}e^{+ik_g d} \\ r_{gx}e^{+ik_g d} + r_{yg}e^{-ik_g d} & e^{+ik_g d} + r_{gx}r_{yg}e^{-ik_g d} \end{bmatrix} = \begin{bmatrix} A & B \\ C & D \end{bmatrix} \tag{C.2}$$

To calculate the optical parameters of interest, we convert the transfer matrix to a scattering matrix using the following relation:

$$\begin{bmatrix} U_y^+ \\ U_x^- \end{bmatrix} = \frac{1}{D} \begin{bmatrix} AD - BC & B \\ -C & 1 \end{bmatrix} \begin{bmatrix} U_x^+ \\ U_y^- \end{bmatrix} = \begin{bmatrix} t_{xy} & r_{yx} \\ r_{xy} & t_{yx} \end{bmatrix} \begin{bmatrix} U_x^+ \\ U_y^- \end{bmatrix}. \tag{C.3}$$

Setting the incoming field $U_x^+ = 0$ and $U_y^- = 1$ gives the following straightforward relations for the film reflection and transmission coefficients in terms of the transfer matrix elements: $r_{yx} = B/D$, $t_{yx} = 1/D$. Assuming the incident radiation is incident from vacuum ($y = 0$) and the lossy layer, g, is on top of a substrate material ($x = s$)

we can write the optical coefficients in the following form.

$$r_{0s} = \frac{r_{0g} + r_{gs}e^{-2ik_g d}}{1 + r_{gs}r_{0g}e^{-2ik_g d}} \tag{C.4}$$

$$t_{0s} = \frac{t_{gs}t_{0g}e^{-ik_g d}}{1 + r_{gs}r_{0g}e^{-2ik_g d}} \tag{C.5}$$

The reflectance, transmittance, and absorption are given by $R = |r_{0s}|^2$ and $T = \frac{n_s}{n_0}|t_{0s}|^2$ and $A = 1 - R - T$. The results are the same as those given in [91].

C.2 Useful limits

First we consider the value of the complex refractive index of the graphene layer in comparison to the surrounding dielectric materials. The refractive index in the graphene is given by:

$$\begin{aligned}
\widetilde{n}_g &= \sqrt{\overline{\epsilon} - i\frac{\widetilde{\sigma}}{\omega\epsilon_0}} \\
&= \sqrt{\overline{\epsilon} - i\frac{\widetilde{G}}{d_1\omega\epsilon_0}} \\
&\approx \sqrt{-i\frac{\widetilde{G}}{d_1\omega\epsilon_0}} \\
&= \sqrt{-i\frac{Z_0\widetilde{G}}{2\pi}\frac{\lambda}{d_1}}.
\end{aligned} \tag{C.6}$$

In the above expression $\widetilde{G}$ is the complex sheet conductivity of graphene, d_1 is the thickness of a single graphene layer (around $3.35\mathring{A}$), ω is the frequency of illumi-

nation, ϵ_0 is the free-space permittivity, Z_0 is the impedance of free-space, and $\bar{\epsilon}$ is the average permittivity of the surrounding media. To simplify the expression, it was assumed that $\sigma/\omega\epsilon_0$ is much larger than unity. This is well justified, since for example, at the wavelength of 1 μm, which should make this factor small because of the high optical frequency range, the resulting value for this factor is around 20 (here the universal conductivity value of $\widetilde{G} = G_0 = \pi e^2/2h = 6 \times 10^{-5}$[S] and surrounding media with an average refractive index of about 2 was used, where e is the elementary electron charge, and h is Planck's constant). We can also use Eqn.(C.6) to simplify the phase argument in Eqns. (C.4) and (C.5).

$$\begin{aligned} \Phi &= ik_0\widetilde{n}_g d \\ &= ik_0\widetilde{n}_g^2 d/\widetilde{n}_g \\ &= \widetilde{G}NZ_0/\widetilde{n}_g \end{aligned} \tag{C.7}$$

In the above expression, $N = d/d_1$ is the number of layers in the sample. We note that except for large values of N, the above value of Φ should be small ($\ll 1$).

We now substitute the trivial reflection and transmission expressions (r_{ab}, t_{ab}) into Eqn.(C.4) and (C.5).

$$r_{os} = \frac{(n_0 - \widetilde{n}_g)(\widetilde{n}_g + n_s) + (\widetilde{n}_g - n_s)(n_0 + \widetilde{n}_g)e^{-2\Phi}}{(n_0 + \widetilde{n}_g)(\widetilde{n}_g + n_s) + (\widetilde{n}_g - n_s)(n_0 - \widetilde{n}_g)e^{-2\Phi}} \tag{C.8}$$

$$t_{os} = \frac{4n_0\widetilde{n}_g e^{-\Phi}}{(n_0 + \widetilde{n}_g)(\widetilde{n}_g + n_s) + (\widetilde{n}_g - n_s)(n_0 - \widetilde{n}_g)e^{-2\Phi}} \tag{C.9}$$

If we make the following thin-film limit approximation, $e^{-x} \approx 1 - x$ (i.e., $x \ll 1$) then the above equations can be simplified to:

$$R = |r_{os}|^2 = \frac{|n_0 - n_s - \widetilde{G}NZ_0|^2}{|n_0 + n_s + \widetilde{G}NZ_0|^2} \tag{C.10}$$

$$T = \frac{n_s}{n_0}|t_{os}|^2 = \frac{4n_0 n_s}{|n_0 + n_s + \widetilde{G}NZ_0|^2}. \tag{C.11}$$

Using the expression $A = 1 - R - T$ gives the following expression for the absorption, which depends only on the real part of the graphene conductivity.

$$A = \frac{4\mathrm{Re}\left(\widetilde{G}\right) NZ_0 n_0}{(n_0 + n_s)^2 + 2\mathrm{Re}\left(\widetilde{G}\right) NZ_0(n_0 + n_s) + \left(|G|NZ_0\right)^2}$$

$$A \approx \frac{4\mathrm{Re}\left(\widetilde{G}\right) NZ_0 n_0}{(n_0 + n_s)^2} \tag{C.12}$$

The above equations denote the thin-film limit equations for graphene. If we apply Eqn.(C.12) for the case of a single free-standing layer in the optical regime ($n_0 = n_s = 1,\ N = 1,\ Z_0 = 377\,\Omega,\ \widetilde{G} = G_0$) then $A = 6 \times 10^{-5}[\mathrm{S}] \times 377\,[1/\mathrm{S}] = 2.3\%$ which is the well known universal optical absorption for graphene. For multilayer graphene consisting of more than 10 layers, the full expressions given by Eqns. C.8 and C.9 should be used.

Bibliography

[1] G.D. Reid and K. Wynne. Ultrafast laser technology and spectroscopy. *Encyclopedia of Analytical Chemistry*, 2000.

[2] W. Demtröder. *Laser Spectroscopy 1.* Springer Berlin Heidelberg, 2014.

[3] A. Markelz, S. Whitmire, J. Hillebrecht, and R. Birge. Thz time domain spectroscopy of biomolecular conformational modes. *Phys. Med. Biol.*, 47(21):3797, 2002.

[4] M.C. Nuss and J. Orenstein. Terahertz time-domain spectroscopy. In *Millimeter and submillimeter wave spectroscopy of solids*, pages 7–50. Springer, 1998.

[5] D. Grischkowsky, S. Keiding, M. van Exter, and C. Fattinger. Far-infrared time-domain spectroscopy with terahertz beams of dielectrics and semiconductors. *JOSA B*, 7(10):2006–2015, 1990.

[6] J. Shah. *Ultrafast Spectroscopy of Semiconductors and Semiconductor Nanostructures*, volume 115. Springer, 1999.

[7] B.E. Saleh and M.C. Teich. *Fundamentals of Photonics*. Wiley New York, 1991.

[8] K. Kim and T.E. Murphy. Porous silicon integrated mach-zehnder interferometer waveguide for biological and chemical sensing. *Opt. Express*, 21(17):19488–19497, Aug 2013.

[9] A.K. Geim, K.S. Novoselov, O.V. Yazyev, S.G. Louie, S. Ghosh, W. Bao, D.L. Nika, S. Subrina, E.P. Pokatilov, C.N. Lau, and A.A. Balandin. Nobel prize for graphene. *Nat. Mater.*, 6:183–192, 2007.

[10] M. Hochberg and T. Baehr-Jones. Towards fabless silicon photonics. *Nature Photon.*, 4(8):492–494, 2010.

[11] B. Jalali and S. Fathpour. Silicon photonics. *J. Lightwave Technol.*, 24(12):4600–4615, 2006.

[12] G.T. Reed and A.P. Knights. *Silicon Photonics*. Wiley Online Library, 2008.

[13] G.P. Agrawal. *Fiber-Optic Communication Systems*, volume 4. Wiley, 2010.

[14] H. Föll, M. Christophersen, J. Carstensen, and G. Hasse. Formation and application of porous silicon. *Mater. Sci. Eng. R-Rep.*, 39(4):93–141, 2002.

[15] W. Theiß. Optical properties of porous silicon. *Surf. Sci. Rep.*, 29(3):91–192, 1997.

[16] G. Vincent. Optical properties of porous silicon superlattices. *Appl. Phys. Lett.*, 64(18):2367–2369, 1994.

[17] D.J. Lockwood. Optical properties of porous silicon. *Solid State Commun.*, 92(1):101–112, 1994.

[18] A.G. Cullis, L.T. Canham, and P.D.J. Calcott. The structural and luminescence properties of porous silicon. *J. Appl. Phys.*, 82(3):909–965, 1997.

[19] F.Z. Henari, K. Morgenstern, W.J. Blau, V.A. Karavanskii, and V.S. Dneprovskii. Third-order optical nonlinearity and all-optical switching in porous silicon. *Appl. Phys. Lett.*, 67(3):323–325, 1995.

[20] V.S.-Y. Lin, K. Motesharei, K.-P.S. Dancil, M.J. Sailor, and M.R. Ghadiri. A porous silicon-based optical interferometric biosensor. *Science*, 278(5339):840–843, 1997.

[21] V. Klimov, D. McBranch, and V. Karavanskii. Strong optical nonlinearities in porous silicon: Femtosecond nonlinear transmission study. *Phys. Rev. B*, 52(24):R16989, 1995.

[22] P. Apiratikul, A.M. Rossi, and T.E. Murphy. Nonlinearities in porous silicon optical waveguides at 1550 nm. *Opt. Express*, 17(5):3396–3406, 2009.

[23] P.B. Chapple, J. Staromlynska, J.A. Hermann, T.J. Mckay, and R.G. McDuff. Single-beam z-scan: Measurement techniques and analysis. *Journal of Nonlinear Optical Physics & Materials*, 6(03):251–293, 1997.

[24] M. Dinu, F. Quochi, and H. Garcia. Third-order nonlinearities in silicon at telecom wavelengths. *Appl. Phys. Lett.*, 82(18):2954–2956, 2003.

[25] J. Zhang, Q. Lin, G. Piredda, R.W. Boyd, G.P. Agrawal, and P.M. Fauchet. Anisotropic nonlinear response of silicon in the near-infrared region. *Appl. Phys. Lett.*, 91(7):71113–71113, 2007.

[26] W.S.C. Chang. *Fundamentals of Guided-Wave Optoelectronic Devices*, volume 1. Cambridge University Press, 2010.

[27] P. Apiratikul, A.M. Rossi, and T.E. Murphy. Nonlinearities in porous silicon optical waveguides at 1550 nm. *Opt. Express*, 17(5):3396–3406, Mar 2009.

[28] R. Hui and M. O'Sullivan. *Fiber Optic Measurement Techniques*. Academic Press, 2009.

[29] P. Apiratikul. *Semiconductor Waveguides for Nonlinear Optical Signal Processing*. PhD thesis, University of Maryland, College Park, 2009.

[30] K.L. Hall, G. Lenz, E.P. Ippen, and G. Raybon. Heterodyne pump–probe technique for time-domain studies of optical nonlinearities in waveguides. *Opt. Lett.*, 17(12):874–876, Jun 1992.

[31] Y. Shoji, T. Ogasawara, T. Kamei, Y. Sakakibara, S. Suda, K. Kintaka, H. Kawashima, M. Okano, T. Hasama, H. Ishikawa, and M. Mori. Ultrafast nonlinear effects in hydrogenated amorphous silicon wire waveguide. *Opt. Express*, 18(6):5668–5673, Mar 2010.

[32] P.A. Elzinga, R.J. Kneisler, F.E. Lytle, Y. Jiang, G.B. King, and N.M. Laurendeau. Pump/probe method for fast analysis of visible spectral signatures utilizing asynchronous optical sampling. *Appl. Optics*, 26(19):4303–4309, 1987.

[33] T. Matsumoto, T. Futagi, H. Mimura, and Y. Kanemitsu. Ultrafast decay dynamics of luminescence in porous silicon. *Phys. Rev. B*, 47:13876–13879, May 1993.

[34] D. Dimitropoulos, R. Jhaveri, R. Claps, J.C.S. Woo, and B. Jalali. Lifetime of photogenerated carriers in silicon-on-insulator rib waveguides. *Appl. Phys. Lett.*, 86(7):071115–071115, 2005.

[35] R. Tsu, H. Shen, and M. Dutta. Correlation of raman and photoluminescence spectra of porous silicon. *Appl. Phys. Lett.*, 60(1):112–114, 1992.

[36] R.A. Soref and B.R. Bennett. Electrooptical effects in silicon. *IEEE J. Quantum Elect.*, 23(1):123–129, 1987.

[37] A. Cutolo, M. Iodice, P. Spirito, and L. Zeni. Silicon electro-optic modulator based on a three terminal device integrated in a low-loss single-mode soi waveguide. *J. Lightwave Technol.*, 15(3):505–518, 1997.

[38] J. Matres, G.C. Ballesteros, P. Gautier, J.M. Fédéli, J. Martí, and C.J. Oton. High nonlinear figure-of-merit amorphous silicon waveguides. *Opt. Express*, 21(4):3932–3940, 2013.

[39] C. Grillet, L. Carletti, C. Monat, P. Grosse, B. Ben Bakir, S. Menezo, J.M. Fedeli, and D.J. Moss. Amorphous silicon nanowires combining high nonlinearity, fom and optical stability. *Opt. Express*, 20(20):22609–22615, 2012.

[40] J.J. Wathen, V.R. Pagán, R.J. Suess, K.-Y. Wang, A.C. Foster, and T.E. Murphy. Non-instantaneous optical nonlinearity of an a-si:h nanowire waveguide. *Opt. Express*, 22(19):22730–22742, 2014.

[41] J.J. Wathen, V.R. Pagán, and T.E. Murphy. Simple method to characterize nonlinear refraction and loss in optical waveguides. *Opt. Lett.*, 37(22):4693–4695, 2012.

[42] R.J. Suess, M.M. Jadidi, K. Kim, and T.E. Murphy. Characterization of optical nonlinearities in nanoporous silicon waveguides via pump-probe heterodyning technique. *Opt. Express*, 22(14):17466–17477, 2014.

[43] A.B. Fallahkhair, K.S. Li, and T.E. Murphy. Vector finite difference modesolver for anisotropic dielectric waveguides. *J. Lightwave Technol.*, 26(11):1423–1431, 2008.

[44] F. Bonaccorso, Z. Sun, T. Hasan, and A.C. Ferrari. Graphene photonics and optoelectronics. *Nature Photon.*, 4(9):611–622, 2010.

[45] A.N. Grigorenko, M. Polini, and K.S. Novoselov. Graphene plasmonics. *Nature Photon.*, 6(11):749–758, 2012.

[46] X. Cai, A.B. Sushkov, R.J. Suess, M.M. Jadidi, G.S. Jenkins, L.O. Nyakiti, R.L. Myers-Ward, S. Li, J. Yan, D.K. Gaskill, T.E. Murphy, H.D. Drew, and

M.S. Fuhrer. Sensitive room-temperature terahertz detection via the photothermoelectric effect in graphene. *Nat. Nanotechnol.*, 9(10):814–819, 10 2014.

[47] A.H. Castro Neto, F. Guinea, N.M.R. Peres, K.S. Novoselov, and A.K. Geim. The electronic properties of graphene. *Rev. Mod. Phys.*, 81(1):109, 2009.

[48] A.K. Geim and K.S. Novoselov. The rise of graphene. *Nat. Mater.*, 6(3):183–191, 2007.

[49] V.N. Popov. Curvature effects on the structural, electronic and optical properties of isolated single-walled carbon nanotubes within a symmetry-adapted non-orthogonal tight-binding model. *New J. Phys.*, 6(1):17, 2004.

[50] P.R. Wallace. The band theory of graphite. *Phys. Rev.*, 71(9):622, 1947.

[51] S. Winnerl, F. Göttfert, M. Mittendorff, H. Schneider, M. Helm, T. Winzer, E. Malic, A. Knorr, M. Orlita, M. Potemski, M. Sprinkle, C. Berger, and W. A. de Heer. Time-resolved spectroscopy on epitaxial graphene in the infrared spectral range: relaxation dynamics and saturation behavior. *J. Phys. Condens. Matter*, 25(5):054202, 2013.

[52] H. Wang, A. Hsu, J. Wu, J. Kong, and T. Palacios. Graphene-based ambipolar rf mixers. *IEEE Electron Device Lett.*, 31(9):906–908, Sept 2010.

[53] K. Bolotin, K.J. Sikes, Z. Jiang, M. Klima, G. Fudenberg, J. Hone, P. Kim, and H.L. Stormer. Ultrahigh electron mobility in suspended graphene. *Solid State Commun.*, 146(9):351–355, 2008.

[54] W. Choi, I. Lahiri, R. Seelaboyina, and Y.S. Kang. Synthesis of graphene and its applications: a review. *Crit. Rev. Solid State Mater. Sci.*, 35(1):52–71, 2010.

[55] Eric Pop, Vikas Varshney, and Ajit K Roy. Thermal properties of graphene: Fundamentals and applications. *Mrs Bulletin*, 37(12):1273–1281, 2012.

[56] I.W. Frank, D.M. Tanenbaum, A.M. Van der Zande, and P.L. McEuen. Mechanical properties of suspended graphene sheets. *J. Vac. Sci. Technol.*, 25(6):2558–2561, 2007.

[57] T. Otsuji, S.A. Boubanga Tombet, A. Satou, H. Fukidome, M. Suemitsu, E. Sano, V. Popov, M. Ryzhii, and V. Ryzhii. Graphene-based devices in terahertz science and technology. *J. Phys. D: Appl. Phys.*, 45(30):303001, 2012.

[58] A. Tredicucci and M.S. Vitiello. Device concepts for graphene-based terahertz photonics. *IEEE J. Sel. Top. Quantum Electron.*, 20(1):130–138, 2014.

[59] Z. Sun, T. Hasan, F. Torrisi, D. Popa, G. Privitera, F. Wang, F. Bonaccorso, D.M. Basko, and A.C. Ferrari. Graphene mode-locked ultrafast laser. *ACS Nano*, 4(2):803–810, 2010.

[60] Q. Bao, H. Zhang, Y. Wang, Z. Ni, Y. Yan, Z.X. Shen, K.P. Loh, and D.Y. Tang. Atomic-layer graphene as a saturable absorber for ultrafast pulsed lasers. *Adv. Funct. Mater.*, 19(19):3077–3083, 2009.

[61] M.M. Jadidi, A.B. Sushkov, R.L. Myers-Ward, A.K. Boyd, K.M. Daniels, D.K. Gaskill, M.S. Fuhrer, H.D. Drew, and T.E. Murphy. Tunable terahertz hybrid metal–graphene plasmons. *Nano Lett.*, 15(10):7099–7104, 2015.

[62] L. Ju, B. Geng, J. Horng, C. Girit, M. Martin, Z. Hao, H.A. Bechtel, X. Liang, A. Zettl, Y-.R. Shen, and F. Wang. Graphene plasmonics for tunable terahertz metamaterials. *Nat. Nanotechnol.*, 6(10):630–634, 10 2011.

[63] M. Mittendorff, J. Kamann, J. Eroms, D. Weiss, C. Drexler, S.D. Ganichev, J. Kerbusch, A. Erbe, R.J. Suess, T.E. Murphy, S. Chatterjee, K. Kolata, J. Ohser, J.C. König-Otto, H. Schneider, M. Helm, and S. Winnerl. Universal ultrafast detector for short optical pulses based on graphene. *Opt. Express*, 23(22):28728–28735, Nov 2015.

[64] F. Bianco, D. Perenzoni, D. Convertino, S. L. De Bonis, D. Spirito, M. Perenzoni, C. Coletti, M. S. Vitiello, and A. Tredicucci. Terahertz detection by epitaxial-graphene field-effect-transistors on silicon carbide. *Appl. Phys. Lett.*, 107(13), 2015.

[65] J. Maysonnave, S. Huppert, F. Wang, S. Maero, C. Berger, W.A. de Heer, T.B. Norris, L.A. de Vaulchier, S. Dhillon, J. Tignon, R. Ferreira, and J. Mangeney. Terahertz generation by dynamical photon drag effect in graphene excited by femtosecond optical pulses. *Nano Lett.*, 14(10):5797–5802, 2014.

[66] J.M. Dawlaty, S. Shivaraman, M. Chandrashekhar, F. Rana, and M.G. Spencer. Measurement of ultrafast carrier dynamics in epitaxial graphene.

Appl. Phys. Lett., 92(4):042116, 2008.

[67] P.A. George, J. Strait, J. Dawlaty, S. Shivaraman, M. Chandrashekhar, F. Rana, and M.G. Spencer. Ultrafast optical-pump terahertz-probe spectroscopy of the carrier relaxation and recombination dynamics in epitaxial graphene. *Nano Lett.*, 8(12):4248–4251, 2008.

[68] H. Choi, F. Borondics, D. A. Siegel, S. Y. Zhou, M. C. Martin, A. Lanzara, and R. A. Kaindl. Broadband electromagnetic response and ultrafast dynamics of few-layer epitaxial graphene. *Appl. Phys. Lett.*, 94(17), 2009.

[69] K. J. Tielrooij, J. C. W. Song, S. A. Jensen, A. Centeno, A. Pesquera, A. Zurutuza Elorza, M. Bonn, L. S. Levitov, and F. H. L. Koppens. Photoexcitation cascade and multiple hot-carrier generation in graphene. *Nat. Phys.*, 9(4):248–252, 04 2013.

[70] Z. Mics, K.J. Tielrooij, K. Parvez, S.A. Jensen, I. Ivanov, X. Feng, K. Müllen, M. Bonn, and D. Turchinovich. Thermodynamic picture of ultrafast charge transport in graphene. *Nat. Commun.*, 6:7655, 2015.

[71] S. Winnerl, M. Orlita, P. Plochocka, P. Kossacki, M. Potemski, T. Winzer, E. Malic, A. Knorr, M. Sprinkle, C. Berger, W. A. de Heer, H. Schneider, and M. Helm. Carrier Relaxation in Epitaxial Graphene Photoexcited Near the Dirac Point. *Phys. Rev. Lett.*, 107:237401, Nov 2011.

[72] T. Plötzing, T. Winzer, E. Malic, D. Neumaier, A. Knorr, and H. Kurz. Experimental verification of carrier multiplication in graphene. *Nano Lett.*, 14(9):5371–5375, 2014.

[73] J. Horng, C.F. Chen, B. Geng, C. Girit, Y. Zhang, Z. Hao, H.A. Bechtel, M. Martin, A. Zettl, M.F. Crommie, Y-.R. Shen, and F. Wang. Drude conductivity of dirac fermions in graphene. *Phys. Rev. B*, 83(16):165113, 2011.

[74] A. J. Frenzel, C. H. Lui, Y. C. Shin, J. Kong, and N. Gedik. Semiconducting-to-Metallic Photoconductivity Crossover and Temperature-Dependent Drude Weight in Graphene. *Phys. Rev. Lett.*, 113:056602, Jul 2014.

[75] H.Y. Hwang, N.C. Brandt, H. Farhat, A.L. Hsu, J. Kong, and K.A. Nelson. Nonlinear THz Conductivity Dynamics in P-Type CVD-Grown Graphene. *J. Phys. Chem. B*, 117(49):15819–15824, 2013.

[76] G. Jnawali, Y. Rao, H. Yan, and T.F. Heinz. Observation of a Transient Decrease in Terahertz Conductivity of Single-Layer Graphene Induced by Ultrafast Optical Excitation. *Nano Lett.*, 13(2):524–530, 2013.

[77] H.A. Hafez, P.L. Lévesque, I. Al-Naib, M.M. Dignam, X. Chai, S. Choubak, P. Desjardins, R. Martel, and T. Ozaki. Intense terahertz field effects on photoexcited carrier dynamics in gated graphene. *Appl. Phys. Lett.*, 107(25):251903, 2015.

[78] C. Berger, Z. Song, X. Li, X. Wu, N. Brown, C. Naud, D. Mayou, T. Li, J. Hass, A.N. Marchenkov, H. Conrad, P.N. First, and W.A. de Heer. Elec-

tronic confinement and coherence in patterned epitaxial graphene. *Science*, 312(5777):1191–1196, 2006.

[79] W.A. de Heer, C. Berger, M. Ruan, M. Sprinkle, X. Li, Y. Hu, B. Zhang, J. Hankinson, and E. Conrad. Large area and structured epitaxial graphene produced by confinement controlled sublimation of silicon carbide. *Proc. Natl. Acad. Sci.*, 108(41):16900–16905, 2011.

[80] J. Hass, F. Varchon, J. E. Millán-Otoya, M. Sprinkle, N. Sharma, W. A. de Heer, C. Berger, P. N. First, L. Magaud, and E. H. Conrad. Why multilayer graphene on $4h$-SiC$(000\bar{1})$ behaves like a single sheet of graphene. *Phys. Rev. Lett.*, 100:125504, Mar 2008.

[81] M. Sprinkle, D. Siegel, Y. Hu, J. Hicks, A. Tejeda, A. Taleb-Ibrahimi, P. Le Fèvre, F. Bertran, S. Vizzini, H. Enriquez, S. Chiang, P. Soukiassian, C. Berger, W. A. de Heer, A. Lanzara, and E. H. Conrad. First direct observation of a nearly ideal graphene band structure. *Phys. Rev. Lett.*, 103:226803, Nov 2009.

[82] M. Orlita, C. Faugeras, P. Plochocka, P. Neugebauer, G. Martinez, D. K. Maude, A.-L. Barra, M. Sprinkle, C. Berger, W. A. de Heer, and M. Potemski. Approaching the dirac point in high-mobility multilayer epitaxial graphene. *Phys. Rev. Lett.*, 101:267601, Dec 2008.

[83] D. Sun, Z.-K. Wu, C. Divin, X. Li, C. Berger, W.A. de Heer, P.N. First, and T.B. Norris. Ultrafast relaxation of excited dirac fermions in epitaxial

graphene using optical differential transmission spectroscopy. *Phys. Rev. Lett.*, 101:157402, Oct 2008.

[84] D. Sun, C. Divin, C. Berger, W.A. de Heer, P.N. First, and T.B. Norris. Spectroscopic measurement of interlayer screening in multilayer epitaxial graphene. *Phys. Rev. Lett.*, 104:136802, Apr 2010.

[85] P. Michel, F. Gabriel, E. Grosse, P. Evtuschenko, T. Dekorsy, M. Krenz, M. Helm, U. Lehnert, W. Seidel, R. Wünsch, D. Wolhlfarth, and A. Wolf. First lasing of the elbe mid-ir fel. In R. Bakker, L. Giannessi, M. Marsi, and R. Walker, editors, *Proceedings of the 26th FEL Conference*, pages 8–13. Comitato Conferenze Elettra, August 2004.

[86] E. Garmire. Resonant optical nonlinearities in semiconductors. *IEEE J. Sel. Top. Quantum Electron.*, 6(6):1094–1110, 2000.

[87] N. Tolstik, E. Sorokin, and I.T. Sorokina. Graphene mode-locked cr:zns laser with 41 fs pulse duration. *Opt. Express*, 22(5):5564–5571, Mar 2014.

[88] L. A. Falkovsky and S. S. Pershoguba. Optical far-infrared properties of a graphene monolayer and multilayer. *Phys. Rev. B*, 76:153410, Oct 2007.

[89] S. A. Jensen, Z. Mics, I. Ivanov, H.S. Varol, D. Turchinovich, F.H.L. Koppens, M. Bonn, and K.J. Tielrooij. Competing ultrafast energy relaxation pathways in photoexcited graphene. *Nano Lett.*, 14(10):5839–5845, 2014.

[90] J. Holovský, S. Nicolay, S. De Wolf, and C. Ballif. Effect of the thin-film limit on the measurable optical properties of graphene. *Sci. Rep.*, 5:15684, 10 2015.

[91] M. Born and E. Wolf. *Principles of Optics*. Cambridge University Press, 7 edition, 1999.

[92] Q. Li, E. H. Hwang, and S. Das Sarma. Disorder-induced temperature-dependent transport in graphene: Puddles, impurities, activation, and diffusion. *Phys. Rev. B*, 84:115442, Sep 2011.

[93] E. H. Hwang, S. Adam, and S. Das Sarma. Carrier transport in two-dimensional graphene layers. *Phys. Rev. Lett.*, 98:186806, May 2007.

[94] Y. Zhang, V.W. Brar, C. Girit, A. Zettl, and M.F. Crommie. Origin of spatial charge inhomogeneity in graphene. *Nat. Phys.*, 5(10):722–726, 10 2009.

[95] D. Waldmann, J. Jobst, F. Speck, T. Seyller, M. Krieger, and H.B. Weber. Bottom-gated epitaxial graphene. *Nat. Mater.*, 10(5):357–360, 2011.

[96] J. Martin, N. Akerman, G. Ulbricht, T. Lohmann, J.H. Smet, K. Von Klitzing, and A. Yacoby. Observation of electron–hole puddles in graphene using a scanning single-electron transistor. *Nat. Phys.*, 4(2):144–148, 2008.

[97] A.E. Curtin, M.S. Fuhrer, J.L. Tedesco, R.L. Myers-Ward, C.R. Eddy, and D.K. Gaskill. Kelvin probe microscopy and electronic transport in graphene on sic (0001) in the minimum conductivity regime. *Appl. Phys. Lett.*, 98(24):243111, 2011.

[98] M.W. Graham, S.-F. Shi, D.C. Ralph, J. Park, and P.L. McEuen. Photocurrent measurements of supercollision cooling in graphene. *Nat. Phys.*, 9(2):103–108, 2013.

[99] A.C. Betz, S.H. Jhang, E. Pallecchi, R. Ferreira, G. Fève, J.-M. Berroir, and B. Plaçais. Supercollision cooling in undoped graphene. *Nat. Phys.*, 9(2):109–112, 2013.

[100] C.B. McKitterick, D.E. Prober, and M.J. Rooks. Electron-phonon cooling in large monolayer graphene devices. *Phys. Rev. B*, 93:075410, Feb 2016.

[101] C.H. Lui, K.F. Mak, J. Shan, and T.F. Heinz. Ultrafast photoluminescence from graphene. *Phys. Rev. Lett.*, 105:127404, Sep 2010.

[102] S.-F. Shi, T.-T. Tang, B. Zeng, L. Ju, Q. Zhou, A. Zettl, and F. Wang. Controlling graphene ultrafast hot carrier response from metal-like to semiconductor-like by electrostatic gating. *Nano Lett.*, 14(3):1578–1582, 2014.

[103] M.T. Mihnev, J.R. Tolsma, C.J. Divin, D. Sun, R. Asgari, M. Polini, C. Berger, W.A. de Heer, A.H. MacDonald, and T.B. Norris. Electronic cooling via interlayer Coulomb coupling in multilayer epitaxial graphene. *Nat. Commun.*, 6:8105, 2015.

[104] J.C.W. Song, M.S. Rudner, C.M. Marcus, and L.S. Levitov. Hot carrier transport and photocurrent response in graphene. *Nano Lett.*, 11(11):4688–4692, 2011.

[105] L.O. Nyakiti, V.D. Wheeler, N.Y. Garces, R.L. Myers-Ward, C.R. Eddy, and D.K. Gaskill. Enabling graphene-based technologies: Toward wafer-scale production of epitaxial graphene. *MRS Bulletin*, 37(12):1149–1157, 2012.

[106] A. Pospischil, M. Humer, M.M. Furchi, D. Bachmann, R. Guider, T. Fromherz, and T. Mueller. Cmos-compatible graphene photodetector covering all optical communication bands. *Nature Photon.*, 7(11):892–896, 2013.

[107] N.W. Ashcroft and N.D. Mermin. *Solid State Physics*. Saunders College, Philadelphia, 1976.

[108] J. Hebling, K.-L. Yeh, M.C. Hoffmann, B. Bartal, and K.A. Nelson. Generation of high-power terahertz pulses by tilted-pulse-front excitation and their application possibilities. *JOSA B*, 25(7):B6–B19, 2008.

[109] K.J. Chang and M.L. Cohen. Structural stability of phases of black phosphorus. *Phys. Rev. B*, 33(9):6177, 1986.

[110] S.Z. Butler, S.M. Hollen, L. Cao, Y. Cui, J.A. Gupta, Humberto R. Gutiérrez, T.F. Heinz, S.S. Hong, J. Huang, A.F. Ismach, E. Johnston-Halperin, M. Kuno, V.V. Plashnitsa, R.D. Robinson, R.S. Ruoff, S. Salahuddin, J. Shan, L. Shi, M.G. Spencer, M. Terrones, W. Windl, and J.E. Goldberger. Progress, challenges, and opportunities in two-dimensional materials beyond graphene. *ACS Nano*, 7(4):2898–2926, 2013. PMID: 23464873.

[111] A. Castellanos-Gomez, L. Vicarelli, E. Prada, J.O. Island, K.L. Narasimha-Acharya, S.I. Blanter, D.J. Groenendijk, M. Buscema, G.A. Steele, J.V. Alvarez, H.W. Zandbergen, J.J. Palacios, and H.S.J van der Zant. Isolation and characterization of few-layer black phosphorus. *2D Materials*, 1(2):025001, 2014.

[112] F. Xia, H. Wang, and Y. Jia. Rediscovering black phosphorus as an anisotropic layered material for optoelectronics and electronics. *Nat. Commun.*, 5, 07 2014.

[113] X. Ling, H. Wang, S. Huang, F. Xia, and M.S. Dresselhaus. The renaissance of black phosphorus. *Proc. Natl. Acad. Sci. USA*, 112(15):4523–4530, 2015.

[114] Y. Li, S. Yang, and J. Li. Modulation of the electronic properties of ultrathin black phosphorus by strain and electrical field. *J. Phys. Chem. C*, 118(41):23970–23976, 2014.

[115] J. Qiao, X. Kong, Z.-X. Hu, F. Yang, and W. Ji. High-mobility transport anisotropy and linear dichroism in few-layer black phosphorus. *Nat. Commun.*, 5, 2014.

[116] Wikipedia. Phosphorene — Wikipedia, the free encyclopedia, 2016.

[117] N. Youngblood, C. Chen, S.J. Koester, and M. Li. Waveguide-integrated black phosphorus photodetector with high responsivity and low dark current. *Nature Photon.*, 2015.

[118] Likai Li, Yijun Yu, Guo Jun Ye, Qingqin Ge, Xuedong Ou, Hua Wu, Donglai Feng, Xian Hui Chen, and Yuanbo Zhang. Black phosphorus field-effect transistors. *Nature nanotechnology*, 2014.

[119] J. Sotor, G. Sobon, W. Macherzynski, P. Paletko, and K.M. Abramski. Black phosphorus saturable absorber for ultrashort pulse generation. *Appl. Phys. Lett.*, 107(5):051108, 2015.

[120] F. Xia, H. Wang, and Y. Jia. Rediscovering black phosphorus as an anisotropic layered material for optoelectronics and electronics. *Nat. Commun.*, 5, 2014.

[121] Y. Takao and A. Morita. Electronic structure of black phosphorus: tight binding approach. *Physica B+C*, 105(1-3):93–98, 1981.

[122] V. Tran, R. Soklaski, Y. Liang, and L. Yang. Layer-controlled band gap and anisotropic excitons in few-layer black phosphorus. *Phys. Rev. B*, 89(23):235319, 2014.

[123] L. Ma, D.N. Nath, E.W. Lee II, C.H. Lee, M. Yu, A. Arehart, S. Rajan, and Y. Wu. Epitaxial growth of large area single-crystalline few-layer mos2 with high space charge mobility of 192 cm2 v- 1 s- 1. *Appl. Phys. Lett.*, 105(7):072105, 2014.

[124] H.-J. Chuang, X. Tan, N.J. Ghimire, M.M. Perera, B. Chamlagain, M.M.-C. Cheng, J. Yan, D. Mandrus, D. Tománek, and Z. Zhou. High mobility wse2 p-and n-type field-effect transistors contacted by highly doped graphene for low-resistance contacts. *Nano Lett.*, 14(6):3594–3601, 2014.

[125] J. Kumar, M.A. Kuroda, M.Z. Bellus, S.-J. Han, and H.-Y. Chiu. Full-range electrical characteristics of ws2 transistors. *Appl. Phys. Lett.*, 106(12):123508, 2015.

[126] L. Li, Y. Yu, G.J. Ye, Q. Ge, X. Ou, H. Wu, D. Feng, X.H. Chen, and Y. Zhang. Black phosphorus field-effect transistors. *Nat. Nanotechnol.*, 9(5):372–377, 2014.

[127] M. Buscema, D.J. Groenendijk, S.I. Blanter, G.A. Steele, H.S.J. van der Zant, and A. Castellanos-Gomez. Fast and broadband photoresponse of few-layer black phosphorus field-effect transistors. *Nano Lett.*, 14(6):3347–3352, 2014.

[128] M. Engel, M. Steiner, and P. Avouris. Black phosphorus photodetector for multispectral, high-resolution imaging. *Nano Lett.*, 14(11):6414–6417, 2014.

[129] S.B. Lu, L.L. Miao, Z.N. Guo, X. Qi, C.J. Zhao, H. Zhang, S.C. Wen, D.Y. Tang, and D.Y. Fan. Broadband nonlinear optical response in multi-layer black phosphorus: an emerging infrared and mid-infrared optical material. *Opt. Express*, 23(9):11183–11194, 2015.

[130] T. Low, A.S. Rodin, A. Carvalho, Y. Jiang, H. Wang, F. Xia, and A.H. Castro Neto. Tunable optical properties of multilayer black phosphorus thin films. *Phys. Rev. B*, 90(7):075434, 2014.

[131] X. Wang, A.M. Jones, K.L. Seyler, V. Tran, Y. Jia, H. Zhao, H. Wang, L. Yang, X. Xu, and F. Xia. Highly anisotropic and robust excitons in monolayer black phosphorus. *Nat. Nanotechnol.*, 10(6):517–521, 2015.

[132] S. Ge, C. Li, Z. Zhang, C. Zhang, Y. Zhang, J. Qiu, Q. Wang, J. Liu, S. Jia, J. Feng, and D. Sun. Dynamical evolution of anisotropic response in black phosphorus under ultrafast photoexcitation. *Nano Lett.*, 15(7):4650–4656, 2015.

[133] J. He, D. He, Y. Wang, Q. Cui, M.Z. Bellus, H.-Y. Chiu, and H. Zhao. Exceptional and anisotropic transport properties of photocarriers in black phosphorus. *ACS Nano*, 9(6):6436–6442, 2015.

[134] A. Castellanos-Gomez, L. Vicarelli, E. Prada, J.O. Island, K.L. Narasimha-Acharya, S.I. Blanter, D.J. Groenendijk, M. Buscema, G.A. Steele, J.V. Alvarez, H.W. Zandbergen, J.J. Palacios, and H.S.J. van der Zant. Isolation and characterization of few-layer black phosphorus. *2D Mater.*, 1(2):025001, 2014.

[135] H. Asahina, K. Shindo, and A. Morita. Electronic structure of black phosphorus in self-consistent pseudopotential approach. *J. Phys. Soc. Jpn.*, 51(4):1193–1199, 1982.

[136] A. Morita. Semiconducting black phosphorus. *Appl. Phys. A*, 39(4):227–242, 1986.

[137] F. Kadi, T. Winzer, E. Malic, A. Knorr, F. Göttfert, M. Mittendorff, S. Winnerl, and M. Helm. Microscopic Description of Intraband Absorption in Graphene: The Occurrence of Transient Negative Differential Transmission. *Phys. Rev. Lett.*, 113:035502, Jul 2014.

[138] C.R. Dean, A.F. Young, I. Meric, C. Lee, L. Wang, S. Sorgenfrei, K. Watanabe, T. Taniguchi, P. Kim, K.L. Shepard, and J. Hone. Boron nitride substrates for high-quality graphene electronics. *Nat. Nanotechnol.*, 5(10):722–726, 2010.

[139] Q. Wu and X.-C. Zhang. Free-space electro-optic sampling of terahertz beams. *Appl. Phys. Lett.*, 67(24):3523–3525, 1995.

[140] O.E. DeLange. Optical heterodyne detection. *IEEE Spectrum*, 5(10):77–85, October 1968.

[141] R.H. Kingston. *Optical Sources, Detectors, and Systems: Fundamentals and Applications*. Academic Press, 1995.

[142] W. Hou and X. Zhao. Drift of nonlinearity in the heterodyne interferometer. *Precision Engineering*, 16(1):25–35, 1994.

[143] C.-K. Sun, B. Golubovic, J.G. Fujimoto, H.K. Choi, and C.A. Wang. Heterodyne nondegenerate pump–probe measurement technique for guided-wave devices. *Opt. Lett.*, 20(2):210–212, 1995.

[144] A.R. Motamedi, A.H. Nejadmalayeri, A. Khilo, F.X. Kärtner, and E.P. Ippen. Ultrafast nonlinear optical studies of silicon nanowaveguides. *Opt. Express*, 20(4):4085–4101, Feb 2012.